A Measurement of the W Boson Mass with the ALEPH Detector

Jeremy Nowell

Imperial College of Science, Technology and Medicine

November 2000

A thesis submitted for the degree of Doctor of Philosophy of the University of London and the Diploma of Imperial College

Abstract

A measurement of the mass of the W boson in $e^+ e^-$ collisions using data collected with the ALEPH detector at the LEP accelerator is presented. Approximately 450 pb^{-1} of data collected at centre of mass energies between 188.6 and 201.6 GeV during 1998 and 1999 is used for the measurement. The selection of fully hadronic WW decays using a neural network is described. The reconstruction of the invariant mass from the selected events is presented, paying particular attention to the procedure of kinematic fitting and the improvements to the mass resolution obtained by selecting and reconstructing initial state radiation. The W mass is extracted from the resulting invariant mass distribution using the method of Monte Carlo reweighting. The evaluation of relevant systematic uncertainties is described. The W mass is measured to be

$$M_{\mathrm{W}} = 80.453 \pm 0.090\ \mathrm{GeV}/c^2\,.$$

This result is combined with results from ALEPH, the other LEP experiments, and further measurements to give a world average W mass of

$$M_{\mathrm{W}} = 80.436 \pm 0.037\ \mathrm{GeV}/c^2\,.$$

These results are interpreted within the context of the Standard Model of particle physics and compared with the indirect measurement of the W mass:

$$M_{\mathrm{W}} = 80.386 \pm 0.025\ \mathrm{GeV}/c^2\,.$$

Acknowledgements

Firstly I would like to thank the Imperial HEP group for accepting me to do this PhD. I would like to thank Julia Sedgbeer for her support as my supervisor over the past three years and for proof reading this thesis so well.

Many people from the ALEPH WW group have supported and advised me on the work that has gone into this thesis, it has been a pleasure working with them (and attending the famous WW meetings!). I would like to thank John Thompson for his advice and for reading my thesis, and Oliver and #5 Hansen for their invaluable advice on all things related to kinematic fitting. In particular, however, I would like to thank Ann Moutoussi for her continual support, advice and encouragement throughout the course of my PhD.

I would also like to thank all those in London and Geneva who made the whole process more enjoyable: Brinick, Nav, Steve, Tom, Russell, Alun, John, David, Barbara and everyone else.

Finally, I would like to dedicate this thesis to my family, without their love and support over the years none of this would have been possible.

London, November 2000

Contents

List of Figures

List of Tables

Chapter 1

Introduction

During the last forty years the theory describing the interactions between fundamental particles, the Standard Model of Particle Physics, has survived numerous experimental tests. Recent collider and non-collider experiments have measured the parameters of the Standard Model to a high precision. For example, experiments carried out at the Large Electron Positron collider (LEP) have measured the mass of the Z^0 boson, M_Z, with a relative precision of 0.002%.

In 1996 the centre of mass energy of the LEP collider was increased from the Z^0 resonance, the LEP1 phase of operation, past the threshold for WW boson pair production. This phase of operation of the collider, known as LEP2, has allowed the study of the properties of the W boson, in particular the W mass, M_W.

The mass of the W boson mass is a fundamental parameter of the Standard Model. It can be determined indirectly by a global fit to all electroweak data using the relationship

$$M_W^2 \left(1 - \frac{M_W^2}{M_Z^2}\right) = \frac{\pi\alpha}{G_F\sqrt{2}} . \frac{1}{1 - \Delta r}, \tag{1.1}$$

where α is the fine structure constant, G_F is the Fermi coupling constant and Δr includes the effect of higher order corrections, depending logarithmically on the mass of the Higgs boson and quadratically on the mass of the top quark. The current indirect measurement of the W mass is [1].

$$M_W = 80.386 \pm 0.025 \text{ GeV}/c^2 , \tag{1.2}$$

where the error given is the combined statistical and systematic error. A major goal of the LEP2 physics programme is to make a direct measurement of the W mass to a similar level of precision as the indirect measurement, thus providing a test of the Standard Model and allowing the Higgs mass to be constrained through the effect of the radiative corrections.

At the beginning of the LEP2 programme the collider operated at a centre of mass energy of 161 GeV, the threshold for WW pair production. The centre of mass energy of the LEP collider has been steadily increased since that time, primarily to extend the reach of the search for the Higgs boson, reaching an energy of 202 GeV in 1999. The luminosity delivered by LEP has also increased, such that about 450 pb^{-1} of data had been collected by the ALEPH experiment at energies above the WW threshold up to the end of data taking in 1999. At all energies above 161 GeV the W mass is measured using the technique of direct reconstruction. The statistical power of this technique, assuming 100% efficiency, perfect detector resolution and no background, has been estimated as [2]:

$$\Delta M_{\mathrm{W}} \sim \frac{\Gamma_{\mathrm{W}}}{\sqrt{N}} \approx 50\ \mathrm{MeV}/c^2 \sqrt{\frac{100\ \mathrm{pb}^{-1}}{\mathcal{L}}}, \tag{1.3}$$

where Γ_{W} is the width of the W boson, N is the number of events collected and $\mathcal{L}$ is the integrated luminosity of the data collected. Thus with 450 pb^{-1} of data a statistical precision of $\sim$ 25 MeV/c^2 would be expected, comparable to the uncertainty on the indirect measurement.

This thesis describes the measurement of the W boson mass using events in which both W particle has decayed hadronically selected from data collected by the ALEPH collaboration in 1998 and 1999, at centre of mass energies between 189 GeV and 202 GeV. Chapter 2 describes the theory of W boson production and decay. Chapter 3 describes the LEP collider and the ALEPH detector. The remainder of the thesis is devoted to the description of the W mass measurement. Chapter 4 describes the selection of fully hadronic WW events, while Chapter 5 describes the reconstruction of the selected events. Chapter 6 explains the extraction of the W mass. Chapter 7 describes the calculation of the systematic uncertainties on the measurement. The measurement is combined with other ALEPH and LEP W mass measurements in Chapter 8, and interpreted in terms of the Standard Model. Finally, Chapter 9 summarises the thesis.

Chapter 2

Theoretical Framework

2.1 Introduction

Particle physics involves the study of the fundamental constituents of matter and their interactions. This chapter begins with a short introduction to the Standard Model of particle physics. The physics of W bosons is then explored in more detail, starting with W pair production and then W boson decay.

2.2 The Standard Model

The Standard Model of particle physics is a gauge theory describing the electroweak and strong interactions of fundamental particles. It is based on the electroweak model of Glashow, Weinberg and Salam [3, 4, 5], the electroweak interactions of quarks being introduced through the GIM mechanism (Glashow, Iliopoulos and Maiani) [6]. It has the group structure of:

$$SU(3)_C \otimes SU(2)_L \otimes U(1)_Y \, , \tag{2.1}$$

where C refers to the colour charge, L to the weak isospin of left handed fermions, Y the weak hypercharge, $U(N)$ the group of unitary transformations on N objects[1] and $SU(N)$ the group of special unitary transformations on N objects[2].

---

[1] The unitary transformations are those which can be represented by a group of unitary matrices, unitary matrices being those whose inverse are equal to their transpose conjugate: $\tilde{U}^* U = I$.

[2] The special unitary transformations are those which can be represented by unitary matrices with determinant 1.

The $SU(3)_C$ part of the theory describes QCD and the $SU(2)_L \otimes U(1)_Y$ part describes the electroweak interaction. The photon, Z^0 and $W^{\pm}$ gauge bosons arise from the spontaneous breaking of the electroweak symmetry by the Higgs mechanism [7]. It is through this mechanism that the Z^0 and $W^{\pm}$ gauge bosons acquire masses. The Higgs mechanism also predicts the existence of a scalar particle, the Higgs boson, which is the only particle in the Standard Model that has not been experimentally verified. The Standard Model is described in detail in References [8, 9, 10].

2.3 W Pair Production

At LEP2 the main mechanism for the production of W bosons is pair production via electron positron annihilation:

$$e^+e^- \to W^+W^- .$$

At tree level three Feynman diagrams contribute to this process, the `CC03` diagrams[3], shown in Figure 2.1. The first two of these diagrams are the *annihilation* diagrams, with either a Z^0 boson or a photon produced in the s-channel. The third diagram is the *conversion* diagram with the exchange of a neutrino in the t-channel.

Each of the W bosons rapidly decays to a pair of fermions, either a lepton and neutrino or quark and antiquark. The final state is thus four fermions. Besides the WW diagrams, there are many other processes that can give rise to a four fermion final state. For example the final state $e^+e^- \, \nu_e \, \bar{\nu}_e$ can be produced by the following processes:

$$e^+e^- \to Z^0Z^0 ,$$

$$e^+e^- \to We\nu_e ,$$

$$e^+e^- \to Z^0e^+e^- ,$$

$$e^+e^- \to Z^0\nu_e\bar{\nu}_e .$$

To distinguish between final states, those coming from W pair production are called *signal*, and those from all other processes *background*.

---

[3] So called because there are three *charged current* processes.

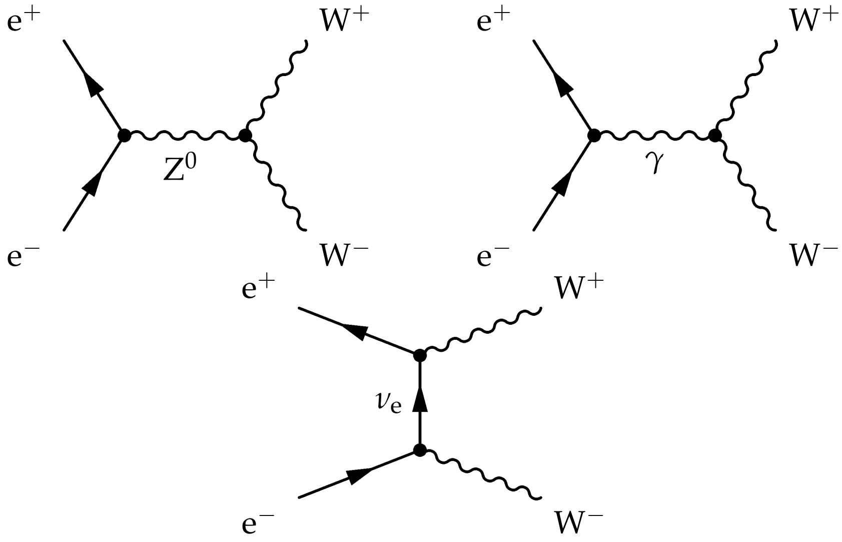

Figure 2.1: The `CC03` diagrams of WW production. The top two diagrams are the annihilation diagrams while the third is the exchange diagram.

2.3.1 On-Shell WW Cross Section

The cross section for the production of four fermions by the process

$$e^+e^- \to f_1\bar{f}_2f_3\bar{f}_4$$

can be expressed as the sum of a signal and background component:

$$\sigma = \sigma_0^{WW}\left(1 + \delta_{EW} + \delta_{QCD}\right) + \sigma_{bkg}\,. \tag{2.2}$$

The background component, σ_{bkg}, includes all contributions from non WW processes, such as $e^+e^- \to W^-e^+\nu_e$. The WW component has three contributions:

- σ_0^{WW} is the lowest order cross-section, or Born approximation, calculated using the three `CC03` diagrams for W pair production shown in Figure 2.1.
- δ_{EW} accounts for the higher order electroweak corrections such as loop corrections and real photon emission. More detail can be found in Section 2.3.4.
- δ_{QCD} accounts for the higher order QCD corrections. These apply only for final states containing pairs of quarks, and one of the biggest effects is hard gluon emission leading to additional jets in the final state.

The production of a four fermion final state for WW processes takes place through a double-resonant WW stage. The W bosons have a finite width so are off-shell. However, the on shell process where the W width is neglected is a useful first step in the calculation of the cross section. The cross section can be calculated analytically [11] for the `CC03` diagrams to give the following expression:

$$\sigma_{Born} = \frac{\pi\alpha^2}{s}\frac{1}{\sin^4\theta_W}\beta + \mathcal{O}\left(\beta^3\right) \ , \tag{2.3}$$

where θ_W is the Weinberg or weak mixing angle and $\beta = \sqrt{1 - 4M_{\mathrm{W}}^2/s}$. $\sqrt{s}$ is the centre of mass energy, and the sharp dependence of the Born cross section on this quantity is shown in Figure 2.2. The term proportional to β is due to the t-channel neutrino exchange diagram, while the s-channel diagrams and s-t channel interference lead to the term proportional to β^3. Close to threshold β is very small and so the t-channel contribution is dominant. The s channel contribution grows as the centre of mass energy is increased. At $\sqrt{s} = 188.6$ GeV $\beta \sim 0.5$ so the t channel process is still the dominant contribution.

In addition to the `CC03` diagrams there is also a tree level Higgs contribution to the cross section, however this is negligible since it is suppressed by a factor of $m_{\mathrm{e}}/M_{\mathrm{W}}$, where m_{e} is the mass of the electron. This contribution becomes more important at higher energies where its inclusion becomes necessary to avoid unitarity problems.

2.3.2 W Width

The production and decay of each W boson can be described by a Breit-Wigner resonance. The total decay width of the W boson, Γ_{W}, is obtained by summing up the partial decay widths of the W for each possible final state. A precision measurement of the W width may then provide evidence for physics beyond the Standard Model, for example the decay of the W into supersymmetric particles. The masses of the fermions into which the W decays are small compared to the W boson mass and so are usually neglected in the calculation of the partial widths, carried out using the appropriate matrix elements. The same corrections δ_{EW} and δ_{QCD} mentioned in the previous section have to be used in the calculation of the partial widths. These corrections can be accounted for by parametrising the lowest order width in terms of the Fermi constant, G_F, determined from measurements of the muon lifetime, and the mass of the W boson. We then obtain for the partial widths the following expressions [12]:

$$\Gamma_{\mathrm{W}\to\ell\nu} = \frac{G_F M_{\mathrm{W}}^3}{6\sqrt{2}\pi}, \tag{2.4}$$

for leptonic decays and

$$\Gamma_{\mathrm{W}\to q_i q_j} = \frac{G_F M_{\mathrm{W}}^3}{6\sqrt{2}\pi} 3 \left|V_{ij}\right|^2 \left(1 + \frac{\alpha_s\left(M_{\mathrm{W}}^2\right)}{\pi}\right) \tag{2.5}$$

for hadronic decays. The factor of 3 in Equation 2.5 arises because each quark has three possible colour states. V_{ij} is the CKM matrix which describes mixing between different quark flavour states, and the factor in brackets is the QCD correction. Thus we have the following expression for the total W width:

$$\Gamma_{\mathrm{W}} = \frac{3 G_F M_{\mathrm{W}}^3}{2\sqrt{2}\pi} \left(1 + \frac{2\alpha_s\left(M_{\mathrm{W}}^2\right)}{\pi}\right). \tag{2.6}$$

Note the dependence of the W width on the W mass. This dependence is used in the W mass measurement described in this thesis.

The current world average measurement of the W width is 2.12 ± 0.05 GeV/c^2 [13] in good agreement with the Standard Model prediction of 2.0927 ± 0.0025 GeV/c^2 [13].

2.3.3 Off-Shell WW Cross Section

The full treatment of WW production must take into account the finite width of the W bosons. The leading order cross section can be described as the two-fold convolution of a hard-scattering cross section with two Breit-Wigner density functions:

$$\sigma(s) = \int_0^s ds_1 \int_0^{\left(\sqrt{s}-\sqrt{s_1}\right)^2} ds_2 \rho(s_1) \rho(s_2) \sigma^0(s, s_1, s_2), \tag{2.7}$$

where

$$\rho(s) = \frac{1}{\pi} \frac{\Gamma(s)}{\left(s - M_{\mathrm{W}}^2\right)^2 + \Gamma^2(s)} \tag{2.8}$$

is the relativistic Breit-Wigner function associated with the W propagators, s is the square of the centre of mass energy of the initial state electron and positron and s_1, s_2 are the squares of the invariant masses of the two virtual W bosons.

$\sigma^0(s, s_1, s_2)$ is the leading order cross section for W pair production, calculated using the `CC03` diagrams (taking into account their interference). Thus the on-shell cross section is just $\sigma^0_{on-shell}(s) = \sigma^0\left(s, M_\mathrm{W}^2, M_\mathrm{W}^2\right)$.

The width in Equation 2.8 can be expressed in two different schemes as:

$$\Gamma(s) = \begin{cases} s \times \Gamma_\mathrm{W}/M_\mathrm{W} & \text{running width} \\ \overline{\Gamma}_\mathrm{W}\overline{M}_\mathrm{W} & \text{fixed width} \end{cases} \tag{2.9}$$

Where the masses and widths in each scheme are related through the following expression [14]:

$$\left(s - \overline{M}_\mathrm{W}^2 + i\overline{M}_\mathrm{W}\overline{\Gamma}_\mathrm{W}\right) = \frac{s - M_\mathrm{W}^2 + is\Gamma_\mathrm{W}/M_\mathrm{W}}{1 + i\Gamma_\mathrm{W}/M_\mathrm{W}}\,. \tag{2.10}$$

The running width scheme is the same as that used at LEP1 in the precision measurement of the mass of the Z^0 boson and so has been adopted at LEP2 for measurements of the W mass. However, the Monte Carlo generator used in this analysis uses the fixed width scheme. Thus to make the quoted mass consistent the following correction must be applied to the measured W mass, M_W^{meas} (which is equivalent to $\overline{M}_\mathrm{W}$) [14]:

$$M_\mathrm{W}^{meas} = M_\mathrm{W} - \frac{1}{2}\frac{\Gamma_\mathrm{W}^2}{M_\mathrm{W}} = M_\mathrm{W} - 27\ \mathrm{MeV}/c^2\,. \tag{2.11}$$

The issue of gauge invariance arises in two ways when going from the on-shell cross section to the off-shell case. The first is that only the `CC03` diagrams are used, instead of the full set of four-fermion diagrams. To include all the diagrams in the calculation is complicated, however, and the `CC03` approximation is sufficient for current measurements [15].

The second more important source of gauge invariance are the poles that occur in the resonant diagrams when $s = M_\mathrm{W}^2$ in Equation 2.8. These singularities can be cured by introducing a finite width in some way, while at the same time preserving gauge invariance and unitarity. The inclusion of the full set of four-fermion diagrams solves this problem since the finite width arises naturally from the imaginary parts of higher order diagrams that describe the boson self-energies. The two width schemes discussed above are ways round this problem. These two methods along with others are discussed further in Reference [15].

2.3.4 Radiative Corrections

Coulomb Correction

The Coulomb correction to the WW cross section is necessary because of the long range electromagnetic interaction between the W^+ and W^-. The cross section tends to be enhanced when the two oppositely charged particles have a relatively low velocity, $v/c \ll 1$.

For the on-shell cross section the Coulomb correction diverges as the threshold for W pair production is approached, since to leading order it is $(1 + \alpha\pi/v_0)$, and the relative velocity $v_0 = 2\left(1 - 4M_W^2/s\right)^{1/2}$ approaches zero at threshold.

For the off-shell case the finite W width screens the Coloumb singularity, acting as a cut-off for multiple soft photon exchange between the W^+ and W^-. The perturbative expansion is in terms of $\alpha\pi\sqrt{M_W/\Gamma_W}$ instead of $\alpha\pi/v_0$ [16]. The correction is approximately 6% close to threshold, but becomes smaller at higher centre of mass energies. Coulomb corrections could also lead to shifts in the average reconstructed mass of the W bosons, by approximately 20 MeV/c^2 in the threshold region, but becoming smaller at higher energies [17].

Similarly to Equation 2.7 the cross section including the Coulomb correction can be written as [16]

$$\sigma(s) = \int_0^s ds_1 \int_0^{\left(\sqrt{s}-\sqrt{s_1}\right)^2} ds_2 \rho(s_1)\,\rho(s_2)\,\sigma^0(s, s_1, s_2)\left[1 + \delta_C(s, s_1, s_2)\right], \quad (2.12)$$

where δ_C is the Coulomb correction which to $\mathcal{O}(\alpha)$ is given by

$$\delta_C(s, s_1, s_2) = \frac{\alpha}{v}\left[\pi - 2\arctan\left(\frac{|\kappa|^2 - p^2}{2p\Re(\kappa)}\right)\right]. \quad (2.13)$$

Here p is the centre of mass momentum of a virtual W boson and v is the average velocity of the W bosons in their centre of mass system and can be expressed as

$$v = \frac{4p}{\sqrt{s}} = 2\sqrt{1 - \frac{2s(s_1 + s_2) - (s_1 - s_2)^2}{s^2}}. \quad (2.14)$$

$\kappa = \sqrt{-M_W(E + i\Gamma_W)}$ where $E = \left(s - 4M_W^2\right)/4M_W$.

Figure 2.2 shows the WW lineshape with and without the Coulomb correction applied.

Initial State Radiation

Initial state radiation (ISR) is one of the largest electroweak corrections to the WW cross section. ISR is the emission of one or more photons from the incoming electron and positron, leading to a reduced centre of mass energy, and therefore a different cross section.

The emission of virtual and soft real photons with energy $E < \omega$ leads to doubly logarithmic contributions $\sim \alpha \ln\left(s/m_{\mathrm{e}}^2\right) \ln\left(s/\omega^2\right)$ at each order in perturbation theory. The infra-red divergent corrections cancel when hard photon radiation is added and the collinear ($\ln\left(s/m_{\mathrm{e}}^2\right)$) logarithms can be resummed and incorporated into the cross section using either a *flux function* or a *structure function* approach [18]. Both of these approaches assume that the ISR correction factorises.

In the flux function approach the ISR corrected cross section is given by:

$$\sigma^{ISR}(s) = \int_{s_{min}}^{s} \frac{ds'}{s} F(x,s)\,\sigma\left(s'\right) , \qquad (2.15)$$

where s' is the square of the reduced centre of mass energy, $x = 1 - s'/s$, and σ is the Coulomb corrected off-shell cross section of Equation 2.12. The radiator function $F(x,s)$ is given by

$$F(x,s) = tx^{t-1}\left(1 + \mathcal{S}(s)\right) + \mathcal{H}(x,s) , \qquad (2.16)$$

where t contains all mass singularity terms $\ln\left(s/m_{\mathrm{e}}^2\right)$:

$$t = \frac{2\alpha}{\pi}\left[\ln\left(\frac{s}{m_{\mathrm{e}}^2}\right) - 1\right] . \qquad (2.17)$$

The $\mathcal{S}(s)$ term comes from soft and virtual photon emission and the $\mathcal{H}(x,s)$ term comes from hard photon emission [19].

Alternatively the structure function approach [20] may be used in which the cross section is given by:

$$\sigma^{QED}(s) = \int_{x_1^{min}}^{1} dx_1 \int_{x_2^{min}}^{1} dx_2 \mathcal{D}(x_1,s)\,\mathcal{D}(x_2,s)\,\sigma(x_1 x_2 s, s_1, s_2) , \qquad (2.18)$$

where

$$\mathcal{D}(x,s) = \frac{t}{2}(1-x)^{t/2-1}\left(1 + \overline{\mathcal{S}}\right) + \overline{\mathcal{H}}(x,s) , \qquad (2.19)$$

and

$$x_1^{min} = \frac{(\sqrt{s_1} + \sqrt{s_2})^2}{s} \qquad x_2^{min} = \frac{(\sqrt{s_1} + \sqrt{s_2})^2}{x_1 s} . \tag{2.20}$$

The predictions of both schemes for the average energy loss through initial state radiation are very similar and so the flux function approach is generally adopted since calculations are numerically faster using this scheme. Figure 2.2 shows the effect of ISR on the WW lineshape.

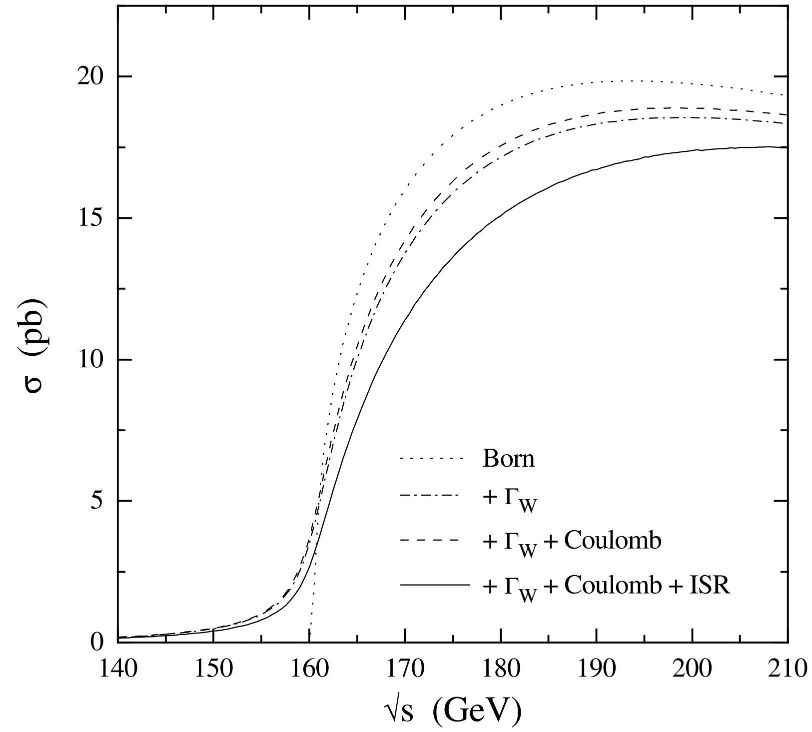

Figure 2.2: The cross section for $e^+e^- \to W^+W^-$ as a function of centre of mass energy, $\sqrt{s}$, in various approximations:
(i) Born (on-shell) cross section (dotted line),
(ii) Born (off-shell) cross section (dash-dotted line),
(iii) as (ii) with first-order Coulomb corrections (dashed line),
(iv) as (iii) with initial state radiation (solid line).

2.4 WW Decay

Each of the W bosons produced in a W pair event at LEP2 quickly decays into a pair of particles, either a quark and antiquark or a lepton and antineutrino, as shown in Figure 2.3. The measurement presented in this thesis uses those events in which both W boson decays into a quark-antiquark pair, the so-called fully hadronic events.

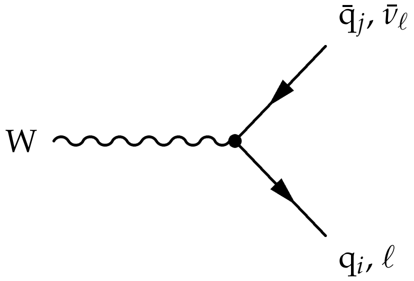

Figure 2.3: W boson decay into quark-antiquark, $q_i\bar{q}_j$, (where the subscripts i, j denote different quark flavours) or lepton antineutrino, $\ell\bar{\nu}_\ell$.

2.4.1 Fragmentation

The coloured quarks or partons produced by the decay of a W boson quickly form colourless jets of particles through a process that can be divided into three stages:

- **Parton Shower:** The initial partons split into quarks and gluons. This stage can be described by perturbative QCD.
- **Hadronisation:** The quarks and gluons combine to form jets of hadrons, leptons and photons.
- **Decay:** The particles formed in the hadronisation step decay.

The definitions of these different steps vary between texts, however for the purpose of this discussion they are replaced by the single term “fragmentation”. The fragmentation of a fully hadronic event is complicated with a final state of many particles, perhaps more than 50 being produced.

The most complicated step in the fragmentation process is hadronisation. This is in the regime of non-perturbative QCD and the modelling of this step is based on phenomenological ideas. The most developed model is the “string fragmentation model” [21] which describes the colour dipole field between the initial $q\overline{q}$ pair as a narrow flux-tube or “string”. This tube has a constant energy per unit length and so the energy stored in it increases linearly with the quark separation. Eventually the stored energy may become large enough to create a new $q\overline{q}$ pair, thus breaking the string. Adjacent quarks at the end of each string are combined to form hadrons which may subsequently decay. This final decay stage is simulated using tables of decay modes and branching ratios. The string model forms the basis of the `JETSET` Monte Carlo program [22] which is used for event simulation throughout the analysis described in this thesis.

The `HERWIG` program [23, 24] is an alternative Monte Carlo event generator which uses a different hadronisation model. The "cluster fragmentation" model is used in which jets of quarks and antiquarks are produced from gluon splitting and then combined into all allowed colour singlets to form clusters. Each of these clusters has a mass distribution and spatial size and fragments into hadrons according to these properties.

2.4.2 Final State Interactions

The Monte Carlo event simulation used in this thesis assumes that the W^+ and W^- decay independently, each W system proceeding through the fragmentation stage without reference to the other. However at LEP2 energies the large width of the W means that the average separation of the W decay vertices is ~ 0.1 fm, smaller than the typical hadronisation scale of ~ 1 fm. In the fully hadronic channel the fragmentation of each W can therefore no longer considered to be independent. These final state interactions (FSI) can be divided into two different processes, colour reconnection and Bose-Einstein effects.

Colour Reconnection

Colour reconnection is a QCD phenomenon in which partons from different W bosons are connected. Instead of the original colour singlets $q_1\overline{q}_2$ and $q_3\overline{q}_4$ it may be possible to form another set, $q_1\overline{q}_4$ and $q_3\overline{q}_2$. These effects could lead to a bias in the reconstructed W mass.

Colour reconnection may take place in either the parton shower or hadronisation stage of fragmentation. In the parton shower phase the effect can be described using perturbative QCD, and is expected to be small [25, 26]. However in the hadronisation stage the effect could be larger but here only phenomenological models exist to describe it. All of these models are based on a space-time picture in which reconnection is a local phenomenon. Objects are formed at the hadronisation stage through a local interaction which may combine products of the two W's in regions where they overlap.

The `JETSET` Monte Carlo program contains three models proposed by Khoze and Sjöstrand based on the string hadronisation model [25]. These are based on different hypotheses of the structure of the QCD vacuum and the confinement mechanism.

- **Model I:** After the parton shower phase the strings are described as cylinders and may reconnect with a probability that is proportional to the degree of overlap of different strings, ϕ.

  $$\mathcal{P}_{reco} = 1 - e^{-k_\phi \phi}, \tag{2.21}$$

  where k_ϕ is a free parameter that can be adjusted to give any desired reconnection probability.

- **Model II:** Strings are viewed as vortex lines with thin core regions. Reconnection takes place if these core regions intersect.

- **Model II$'$:** Similar to model II but reconnection is suppressed if there is no reduction in the overall string length.

The reconnection probability of Model II is partly predicted, however that of Model I is a completely free parameter. The effects of colour reconnection are therefore difficult to estimate since the strength is not predicted absolutely.

Colour reconnection has also been implemented in the cluster fragmentation model in `HERWIG`. Only colour singlet combinations of partons are allowed to form clusters. The probability for colour reconnections to take place is governed by a free parameter.

The Monte Carlo program `ARIADNE` [27, 28] implements colour reconnection within the framework of the Dipole Cascade Model [29, 30]. Colour dipoles are reconnected with a probability $\left(1/N_C^2\right)$, where N_C is the number of colours, only if the total string length is reduced. Colour indices are randomly (with some restrictions) assigned to each colour dipole. After each gluon radiation dipoles with identical indices are allowed to reconnect. Reconnections within and between different W systems are allowed.

Bose-Einstein Correlations

Bose-Einstein (BE) effects [31, 32] are phenomena arising from Bose-Einstein statistics and account for a significant systematic uncertainty on the measured W mass from the fully hadronic channel. In fully hadronic WW events a large number of pions are produced. A consequence of Bose-Einstein statistics is that an enhancement of identical pions at small momentum separation, relative to the hypothetical state of uncorrelated production, is expected – almost four times as many identical pion pairs as in a single W decay. The effect of this is to bias the reconstructed W mass since low momentum pions from different W's are produced closer to each other than in the absence of Bose-Einstein correlations. This reduces the momentum of the W's and so increases the measured mass. The size of the effect is difficult to estimate since the effect is quantum mechanical whereas Monte Carlo programs are based on classical probabilities.

The BE effect is studied using the two-boson correlation function $f(Q)$, where $Q^2 = -(p_1 - p_2)^2$ is the square of the difference in four momenta of the two bosons. The BE enhancement relative to a reference with no BE effects occurs at low values of Q^2 and is given by

$$f(Q) = 1 + \lambda e^{-R^2 Q^2}, \tag{2.22}$$

where R is the radius of a Gaussian source of the bosons and λ is the incoherence parameter which is the effective strength and is in the range $0 \leq \lambda \leq 1$.

The most widely developed model for describing BE effects is the `LUBOEI` model [32] implemented in `JETSET`. In this model the final state particles are redistributed to reproduce the expected two-boson momentum correlations. However in order to do this the momenta of non-identical particles also has to be shifted in order to respect energy and momentum conservation. This procedure can introduce spurious long-range correlations which may have implications for the measured W mass. Other models introduced by the same authors, (BE_2 and BE_{23})

introduce event weights [33]. In these models bigger weights are given to events with pairs of equal sign particles closer in momentum. This method arises naturally in a quantum mechanical approach using matrix elements, however it is a lengthy procedure since all final state particle permutations must be computed.

Chapter 3

Experimental Apparatus

3.1 Introduction

The Large Electron Positron Collider (LEP) is the largest machine of its kind in the world. The main purpose of its construction was the study of the Z^0 and W massive vector bosons, along with searches for new physics beyond the Standard Model. ALEPH [34] is one of the four experiments built at LEP to study electron-positron collisions, the others are DELPHI [35], L3 [36] and OPAL [37].

The first part of this chapter describes LEP and the measurement of the beam energy of the collider, which is an important component of the measurement of the W boson mass. The second part of the chapter is devoted to a description of the ALEPH detector.

3.2 The LEP Collider

LEP [38] is a circular collider of circumference 26.66 km located at the European Organization for Nuclear Research (CERN) in Geneva, Switzerland, as shown in Figure 3.1. It is located in a tunnel that varies in depth between 50 m and 150 m underground, and for geological reasons has a tilt of 1.42%. The accelerator is not in fact quite circular but consists of eight straight sections, each approximately 500 m long, and eight circular arcs. The electrons and positrons are accelerated by radio frequency superconducting cavities installed along the straight sections and guided round the arcs by dipole bending magnets. The beam is contained in

LEP by a complex system of quadrapoles, sextupoles and corrector magnets, and made to collide at four interaction points (IPs) around the ring where the four experiments are located.

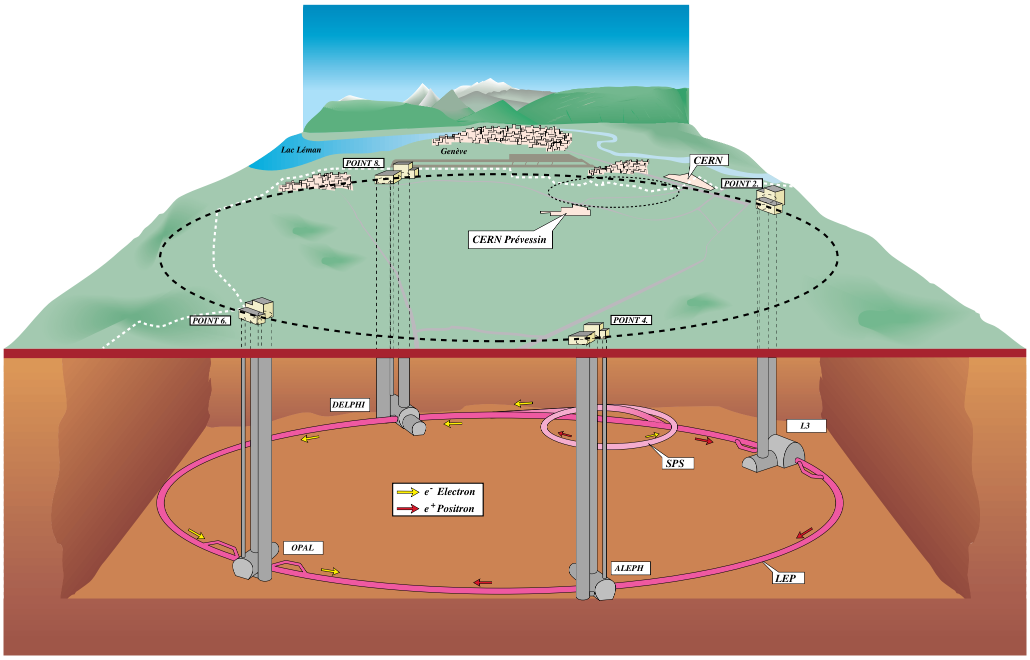

Figure 3.1: An overview of the LEP accelerator.

The series of accelerators at CERN which produce positrons and electrons for injection into LEP are illustrated in Figure 3.2. Electrons are produced by a pulsed electron gun and then accelerated to 200 MeV by a linear accelerator (LINAC). A fraction of these electrons are used to create positrons by collisions with a fixed tungsten target, which produces e^+e^- pairs. A second LINAC, the LEP Linear Injector (LIL), then accelerates the electrons and positrons to an energy of 600 MeV when they are fed into the Electron Positron Accumulator (EPA). The EPA is a 0.12 km storage ring which separates the particles into bunches and stores them until an intensity of $\sim 10^{10}$ particles is achieved. The particles are then injected into the Proton Synchrotron (PS) where they are accelerated to an energy of 3.5 GeV before injection into the Super Proton Synchrotron (SPS). The SPS accelerates the beams to an energy of 22 GeV before final injection into LEP.

Once injected into LEP, the electrons and positrons are accelerated to the nominal physics energy by super-conducting NbTi r.f. cavities, and also normal cop-

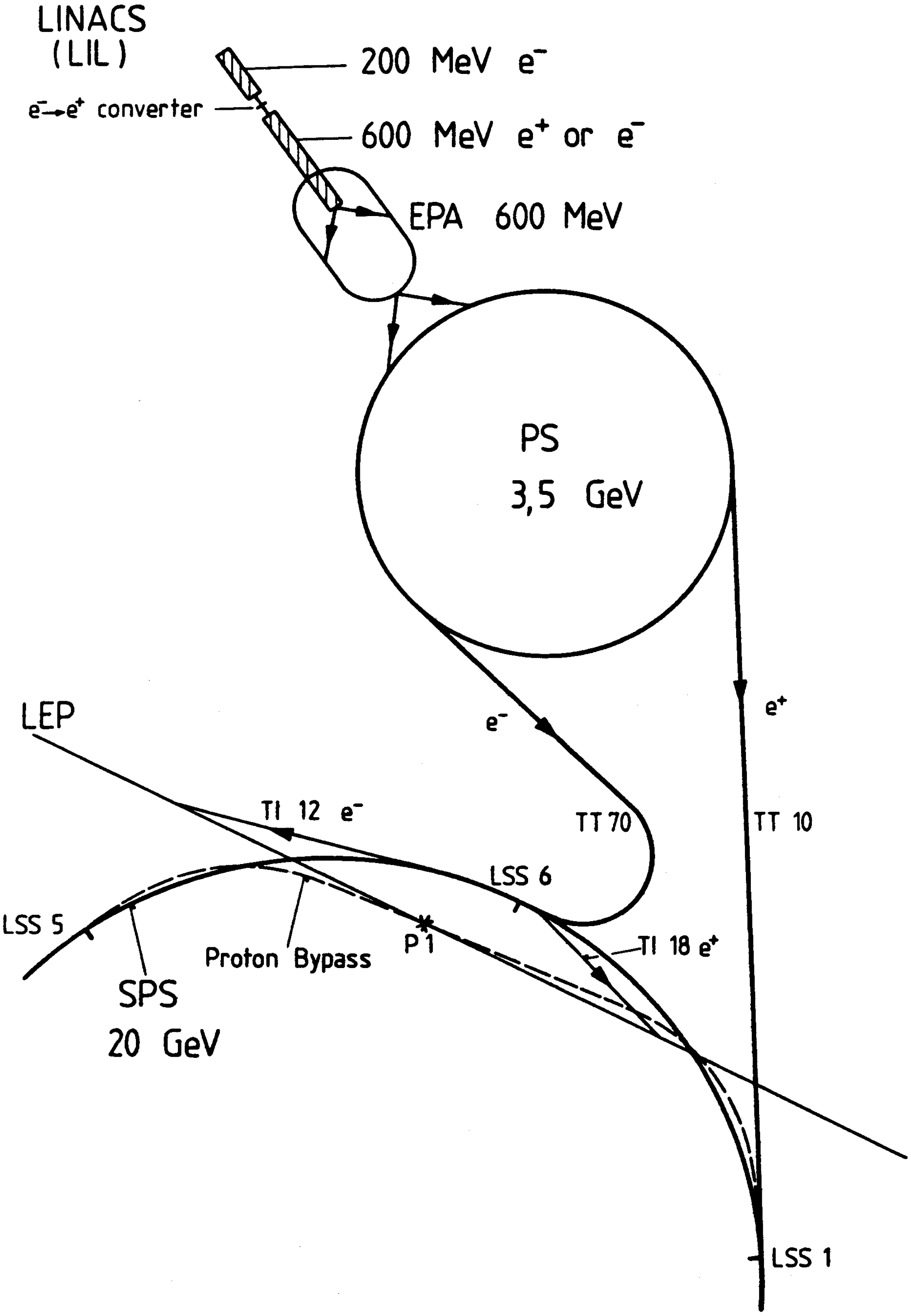

Figure 3.2: The LEP injection scheme.

per r.f. cavities, operating at a frequency of 352 MHz. In 1998 the centre of mass energy, $\sqrt{s}$, of LEP was 188.6 GeV [39], and in 1999 the machine operated at energies between 192 GeV and 202 GeV [40]. In both years a small amount of data was collected at the Z^0 resonance for calibration purposes. The data delivered by LEP and collected by ALEPH is summarised in Table 3.1. The beams have a revolution frequency in LEP of 11245 Hz, taking a time of 88.9 μs per revolution. The particles in each beam are grouped into four bunches, separated by approximately 22 μs. At the interaction points each bunch is approximately 2 cm long, 190 μm wide horizontally and 4 μm wide vertically. When the beam is not focused for collisions it is typically 4 mm wide and 1 mm tall. Typical total beam currents are 6 mA, 750 μA per bunch, corresponding to 3.3×10^{12} particles in total.

Year	Average $\sqrt{s}$ (GeV)	Data Delivered by LEP (pb^{-1})	Data Collected by ALEPH (pb^{-1})	ALEPH Collection Efficiency (%)	Data Used for this Analysis (pb^{-1})
1998	91.0	3.3	3.1	95.0	3.0
1998	188.6	192.7	179.4	93.1	174.2
1999	91.0	4.2	3.9	93.0	3.5
1999	191.6	30.7	29.1	95.0	28.9
1999	195.5	88.1	83.0	94.1	79.9
1999	199.5	91.1	88.3	97.0	86.3
1999	201.6	44.0	42.3	96.1	41.9
1998–99	188.6–201.6	446.6	422.1	94.5	411.2

Table 3.1: Summary of the data used in this thesis.

3.2.1 Determination of the LEP Energy

The measurement of the LEP beam energy is very important to the W mass analysis. The energy is used in a kinematic fit, as described in further detail in Section 5.2. The consequence of this is that the relative uncertainty on the LEP beam energy is directly related to the relative uncertainty on the W mass:

$$\frac{\sigma_{M_W}^{LEP}}{M_W} = \frac{\sigma_{E_{beam}}}{E_{beam}}, \tag{3.1}$$

making a precise measurement of the LEP energy crucial.

At LEP1 the beam energy was measured very precisely, to a level of 1 MeV [41], allowing the precise measurement of the Z^0 boson mass. To perform this measurement the technique of resonant depolarisation (RDP) was used [42]. RDP makes use of the fact that the electrons in the beam can obtain a degree of transverse polarisation through their interaction with the magnetic field, the Sokolov-Ternov effect [43]. The spin vector will precess ν times in one revolution of the ring, where ν is the spin tune and is given by the expression:

$$\nu = \frac{a_{\mathrm{e}} E_{beam}}{m_{\mathrm{e}} c^2} = \frac{E_{beam}\,[\mathrm{MeV}]}{440.6486(1)\,[\mathrm{MeV}]}\,, \tag{3.2}$$

where E_{beam} is the LEP beam energy, m_{e} is the mass of the electron and $a_{\mathrm{e}} = (g_{\mathrm{e}} - 2)/2$ is the anomalous magnetic moment of the electron and is known to 20 parts per billion. Thus a measurement of ν gives E_{beam} to high precision.

The method of RDP cannot be used at LEP2, since transverse polarisation of the beam cannot be maintained at the higher energies used for physics. The beam energy is therefore obtained by extrapolation of RDP measurements at lower energies to physics energies. The beam energy is proportional to the total magnetic bending field in LEP:

$$E_{beam} = \frac{e}{2\pi c} \oint \mathbf{B}.d\ell\,, \tag{3.3}$$

and so magnetic measurements can be used to obtain the beam energy. The magnetic field is measured at 16 points around the LEP ring by nuclear magnetic resonance (NMR) probes inside the bending dipoles. The precise relationship between these measurements and the beam energy is established by calibration using RDP at low energies and then extrapolated to NMR measurements made at LEP2 physics energies. The difference between NMR probe and RDP measurements is shown in Figure 3.3. It can be seen that the differences are small and stable over years, but non-linear. To check the non-linearity and also since the NMR probes do not measure the *total* bending field further measurements are carried out using flux loops. These flux loop measurements are the result of integrating magnetic field measurements from all 3400 bending magnets, covering $\sim$ 97% of the bending field, however with less precision than the NMR probes.

The agreement between the flux loop and NMR measurements is shown in Figure 3.4. It can be seen that there does seem to be some offset between the measurements and this provides the major contribution to the systematic uncertainty on the beam energy measurement. The total uncertainty on the LEP beam energy was determined to be 20 MeV in 1998 [44] and 21 MeV in 1999 [45].

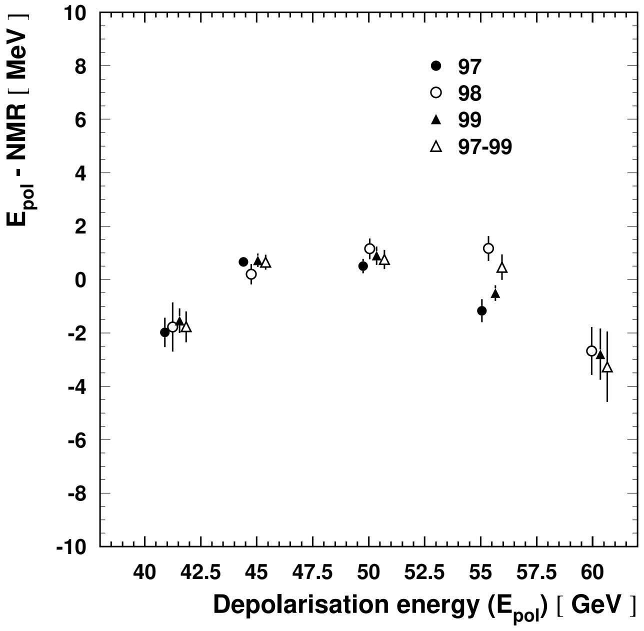

Figure 3.3: Comparison of NMR and RDP measurements, taken from [45].

Once the overall normalisation is fixed, various corrections are applied to the beam energy to take into account variations as a function of time, such as the gravitational pull of the moon, temperature effects and leakage currents from the Geneva-Paris TGV. Corrections also have to be applied to determine the precise energy at each interaction point due to the exact accelerating RF configuration. All of these effects were studied in great detail at LEP1 [41] and so contribute a systematic uncertainty of less than 10 MeV at LEP2.

3.3 The ALEPH Detector

The ALEPH (Apparatus for LEp PHysics) detector was designed to study all types of Standard Model processes at LEP without restricting searches for new

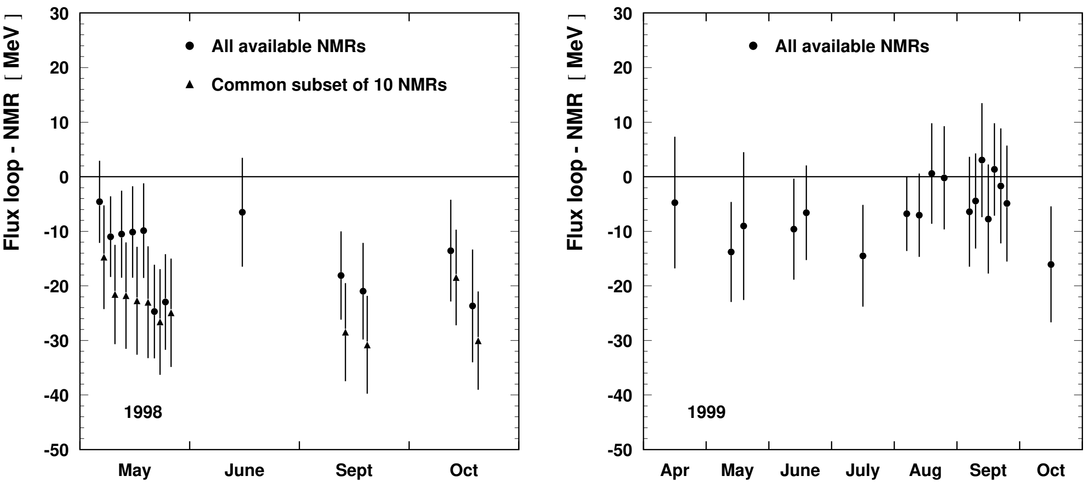

Figure 3.4: Comparison of flux loop and NMR measurements, taken from [45].

physics. The detector was thus designed to cover as much solid angle as possible, with high hermeticity and granularity. In practice a coverage of $\sim 3.9\pi$ sr was achieved. The detector is located at experimental point number four of the LEP ring (near to the village of Echenevex in France), in a cavern 143 m below the surface. It has the approximate shape of a cylinder of diameter 12 m and length 12 m built around the interaction point, weighing over 3000 tons and having some 700 000 readout channels. The ALEPH coordinate reference system is defined as follows: the z direction is along the beam direction, positive in the direction travelled by electrons. This is not quite horizontal since LEP is slightly tilted. The x direction is horizontal and points towards the centre of the LEP ring. The y direction is orthogonal to x and z and points upwards, deviating 3.5875 mrad from the vertical. Cylindrical polar coordinates (r, ϕ, z) are often used, due to the symmetry of the detector, along with θ, the polar angle. A cut-away view of the ALEPH detector is shown in Figure 3.5. The ALEPH detector is described in [34, 46, 47] and its performance is described in [48].

ALEPH consists of several sub-detectors; the major sub-detectors are arranged in six cylindrical layers. The inner three layers consist of the charged particle tracking detectors. A vertex detector surrounds the IP, then a drift chamber which is also an important part of the trigger system, and finally a large time projection

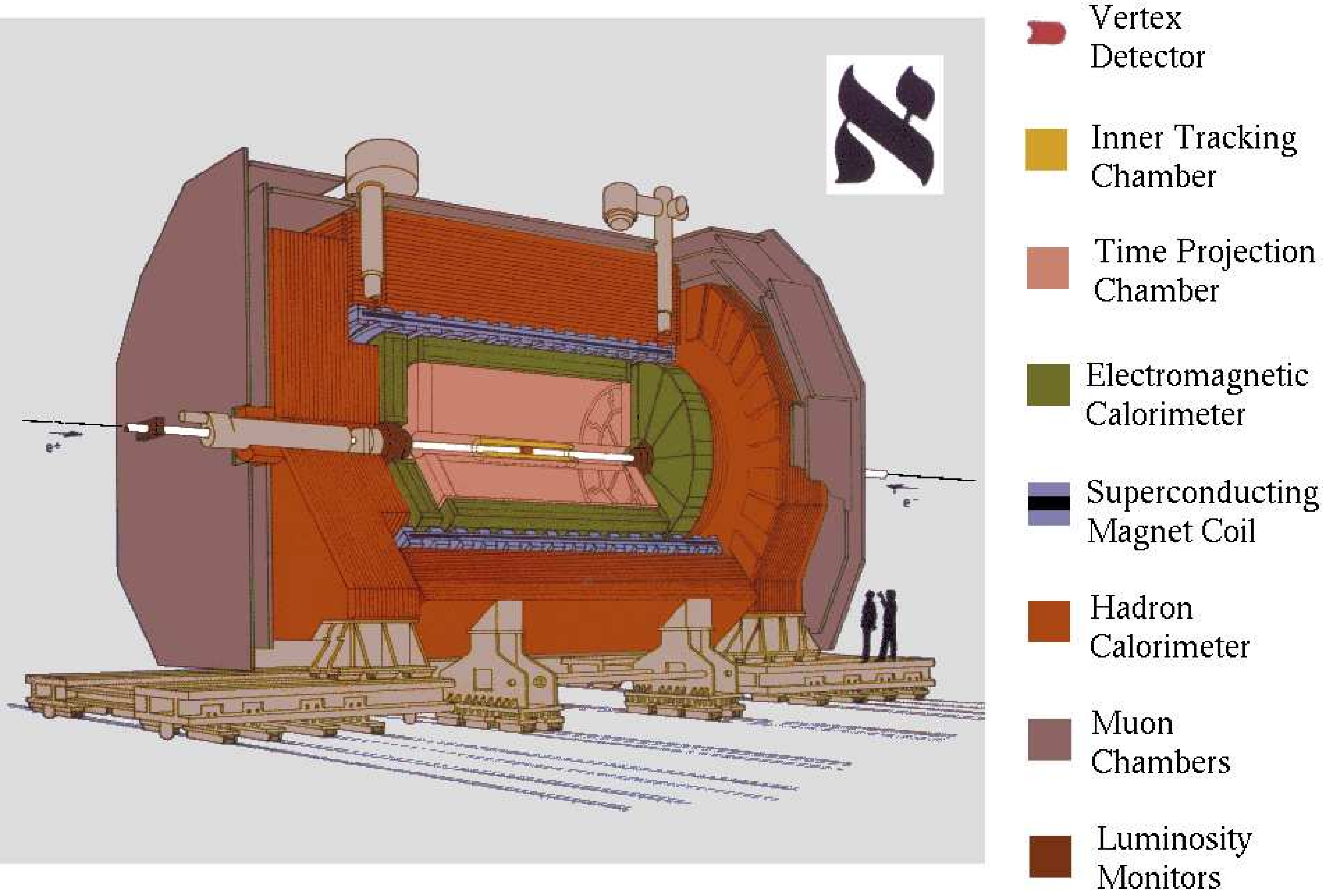

Figure 3.5: The ALEPH detector.

chamber extending to a radius of 1.8 m. In order to obtain charged particle momentum measurements from the tracking detectors a 1.5 Tesla magnetic field is provided by a superconducting solenoid. Measurement of energy is provided by the calorimeters. The highly granular electromagnetic calorimeter provides measurements of the energy of photons and electrons, while the large iron hadronic calorimeter measures the energy of hadronic particles. The iron also acts as the return yolk for the solenoid. The outermost layer is used to identify muons, which generally penetrate all of the other sub-detectors. In addition to these six sub-detectors smaller detectors are installed close to the beam pipe principally to measure Bhabha scattered electrons and positrons for the luminosity measurement, however, these detectors also increase the coverage of the calorimetry.

3.4 Tracking

3.4.1 Vertex Detector

The Vertex Detector (VDET) [49] is the sub-detector closest to the IP. It is a silicon microstrip device occupying a region whose radius extends from 6.3 cm, close to the beam pipe, to 11.0 cm, close to the inner tracking chamber, and has a length of 40 cm. The main purpose of the VDET is to enable the reconstruction of short-lived particles, mainly those containing bottom and charm quarks, with a high efficiency. The current VDET was installed at the start of LEP2 providing improved angular coverage, less passive material and a higher tolerance to radiation than the original VDET. The main physics reason for the upgrade was to improve the efficiency for finding the Higgs boson, which is expected to decay predominantly to bottom quarks.

The VDET is constructed from two layers of silicon wafers, having readout electronics on both sides. Strips running parallel to the beam direction measure the azimuth angle, ϕ, of tracks, while strips running perpendicular to the beam direction measure the z coordinate. For tracks with a normal incidence to the detector spatial resolutions of $\sim$ 10 μm and 15 μm are achieved in the $r\phi$ and z measurements respectively [49]. An angular acceptance of $|\cos\theta| < 0.95$ is achieved for tracks required to hit at least one layer of the VDET.

3.4.2 Inner Tracking Chamber

The Inner Tracking Chamber (ITC) [50] is the second layer of the ALEPH tracking system. The ITC is a 2 m long cylindrical drift chamber, with inner radius of 13 cm and outer radius 29 cm. The chamber has 960 anode sense wires running parallel to the beam arranged in eight layers. The innermost four layers contain 96 wires each, while the outer layers have 144 wires. Each sense wire is surrounded by six field wires held at ground potential, defining hexagonal drift cells. Neighbouring cells share two wires. The cell structure is shown in Figure 3.6. The chamber is filled with a mixture of argon (80%) and carbon dioxide (20%). A small amount of alcohol is added to the mixture as it is believed that this may slow the aging process.

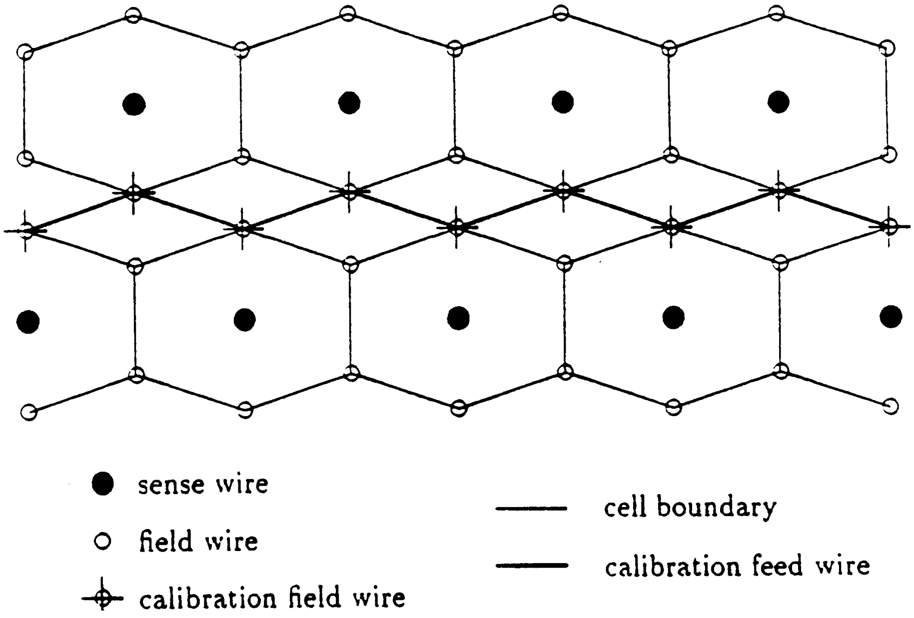

Figure 3.6: The ITC cell structure.

The $r\phi$ resolution of the ITC is determined largely by the properties of the gas, such as the drift velocity, and is $\sim$ 150 μm for high energy muons [48] and $\sim$ 200 μm for all tracks. The z coordinate of the track is determined by the time of arrival of the signal at each end of the sense wire, and the resolution is a few centimetres. A maximum of eight coordinates per track can be provided, giving a three dimensional readout of the trajectories of charged particles. The drift cells are small, with a width between 0.9 and 1.3 cm, so the information provided by the ITC is available extremely quickly, making the ITC invaluable for first stage of the trigger system, Level 1 (see Section 3.6.1), and in fact the ITC provides the only tracking information available to the Level 1 trigger. An $r\phi$ trigger decision is available in 500 ns and a full three dimensional decision including z information in ~ 2 μs.

3.4.3 Time Projection Chamber

The Time Projection Chamber (TPC) [51] is the main tracking detector in ALEPH. It is a large cylindrical drift chamber covering a radial region between 31 cm and 1.8 m, filled with a mixture of argon and methane. A cut-away view of the TPC is shown in Figure 3.7. Electrons produced by the ionisation of the gas by the passage of charged particles drift towards the ends of the chamber due to the presence of a highly uniform electric field of magnitude 11 kV/m created by a central membrane held at -27 kV and annular electrodes situated in the inner and outer cylinder walls. At the ends of the chamber, the signal is recorded by a system of proportional wire chambers arranged into 18 sectors, and read out by a system of cathode pads arranged into 21 circular layers. The $r\phi$ coordinates are given by the centroid of the signal detected at the cathode pads. The z coordinate is determined by measuring the drift time and using knowledge of the drift velocity. Up to 21 coordinates per track are provided by the TPC.

A view of part of the end of the TPC is shown in Figure 3.8, showing a cross section of a wire chamber. A cathode wire plane held at ground potential forms the boundary of the drift volume. Anode sense wires held at $+1250$ V collect the electrons produced in avalanches initiated by the ionisation electrons. Cathode pads underneath the sense wires collect an induced signal. Above the cathode wire plane there is a further grid of wires called the TPC gate. This grid is used to prevent the build up of space charge in the drift region due to positive ions that result from the avalanches close to the sense wires. If a space charge did build up then the local electric field would be influenced leading to the distortion of tracks. In the "open" state the gating wire grid has a negative potential of

~ -67 V applied to it, making it transparent to the passage of charged particles. In the "closed" state alternate wires have potentials of $\sim -67 \pm 100$ V applied. The resulting dipole fields prevent the passage of charged particles. The gate is opened 2 μs before a beam crossing, and if the first level of the trigger system, Level 1, gives a positive decision then the gate is held open for a further 45 μs to allow the ionisation electrons to be collected. If the Level 1 decision is negative then the gate is closed until the next beam crossing.

The resolution of the measured coordinates depends on the drift length and the orientation of the charged particle trajectory with respect to the pads and wires. The $r\phi$ resolution is 173 μm for leptonic Z^0 decays. The z resolution is 740 μm for tracks with polar angles within 10° of perpendicular to the beam direction [48].

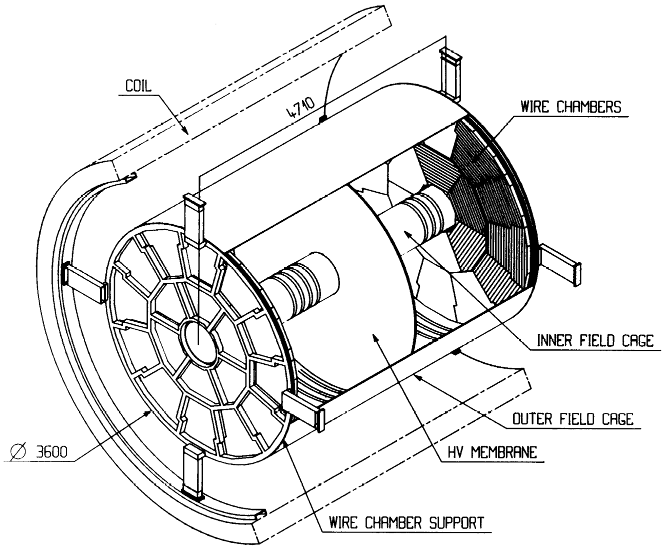

Figure 3.7: The ALEPH time projection chamber.

The TPC also measures energy loss by ionisation, dE/dx, since the magnitude of the signals on the sense wires is proportional to this quantity. The dE/dx depends only on the particle velocity for a given material, so a combination of this and the momentum of the particle allows the mass and so identity of the

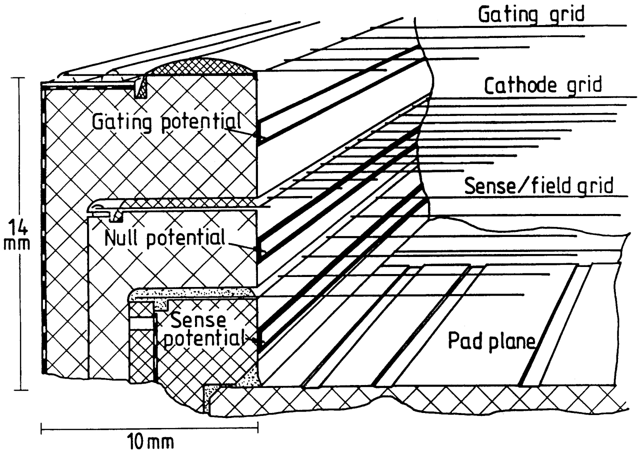

Figure 3.8: Detail of a TPC multiwire chamber.

particle to be deduced. Figure 3.9 shows the measured dE/dx for a sample of 40,000 tracks, along with the fitted parametrisation for various different particles and also the average separation between particle types determined from tracks in hadronic Z^0 decays.

3.4.4 Track Reconstruction

Information from all three tracking detectors is used to reconstruct the passage of charged particles, or "tracks". Track reconstruction begins in the TPC. Hits in neighbouring layers are joined together to form track segments, which are then connected to other segments if the hypothesis that a helix is described is satisfied. This track is then extrapolated into the ITC and VDET, consistent hits being assigned to the track. A final fit is then performed, taking into account the errors on the tracks, to provide a reconstructed track. Table 3.2 summarises the momentum resolution of the different stages obtained from $Z^0 \rightarrow \mu^+\mu^-$ events.

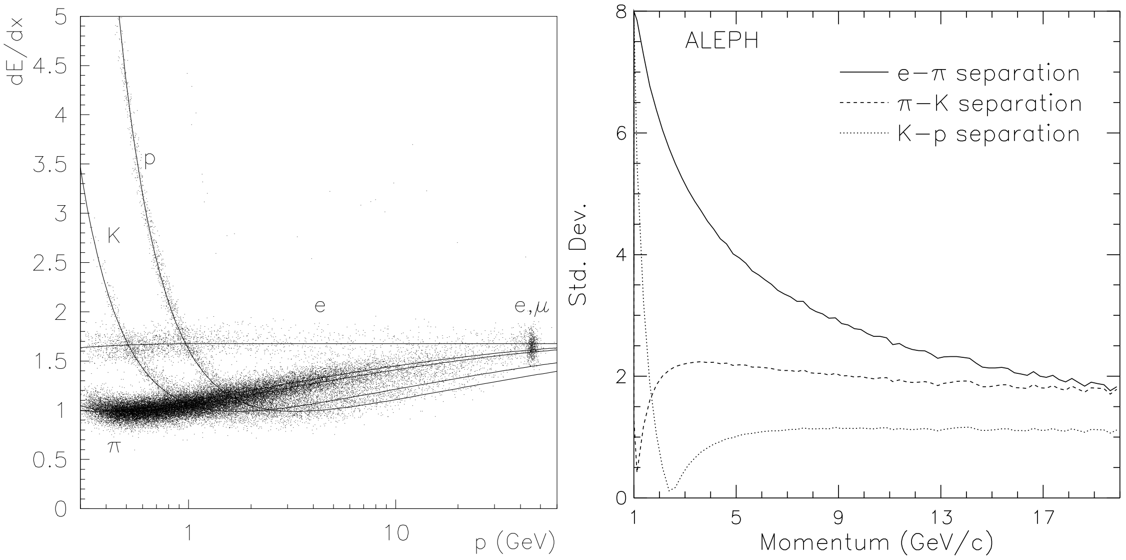

Figure 3.9: The left figure shows the measured dE/dx versus particle momentum for a sample of about 40,000 tracks. Each track was required to have at least 150 dE/dx measurements. The fitted parametrisation is shown for electrons, muons, pions, kaons and protons. The right figure shows the average dE/dx separation in standard deviations between different particle types as a function of momentum. This has been computed using all tracks in hadronic Z^0 decays having at least 50 dE/dx measurements. Taken from Reference [48].

Tracking Detector	σ_p/p^2 (GeV/c)$^{-1}$
TPC	1.2×10^{-3}
+ ITC	0.8×10^{-3}
+ ITC and VDET	0.6×10^{-3}

Table 3.2: The momentum resolution σ_p/p^2, where p is the momentum, of the ALEPH tracking detectors. Taken from Reference [48].

3.5 Calorimetry

3.5.1 Electromagnetic Calorimeter

The Electromagnetic Calorimeter (ECAL) detects energy deposited by electrons and photons and also any energy deposited by hadrons. The ECAL consists of a 4.77 m long barrel around the TPC and end-caps at both ends. The barrel and each end cap consist of 12 modules, each of which covers 30 degrees in ϕ, made from 45 interleaved layers of lead sheets and wire chambers. The ECAL has $\sim$ 40 cm of lead, corresponding to 22 radiation lengths, X_0.

Electrons, positrons and photons which penetrate the lead sheets produce an electromagnetic shower of electron-positron pairs that is sampled by the wire planes. The showers produce ionisation in the xenon and carbon dioxide gas mixture that forms an avalanche towards the anode wires, inducing signals on small cathode pads. The cathode pads are read out in groups, called towers, which point towards the interaction point, of angular size $0.9^\circ \times 0.9^\circ$. These 74000 towers thus have a high granularity, and so give spatial separation of electromagnetic showers, aiding in particle identification. The towers are further segmented into three sections along their length, known as storeys, corresponding to $4X_0$, $9X_0$ and $9X_0$. This allows the shower profile to be studied, aiding further in particle identification. An ECAL layer is illustrated in detail in Figure 3.10.

The energy resolution of the ECAL has been studied using Bhabha scattered electrons, comparing their measured ECAL energy with the track momentum or beam energy. The resolution has been parametrised as [48]:

$$\frac{\sigma(E)}{E} = \frac{0.18}{\sqrt{E(\mathrm{GeV})}} + 0.009\,. \tag{3.4}$$

The signal from the ECAL wire planes is available to the trigger processors.

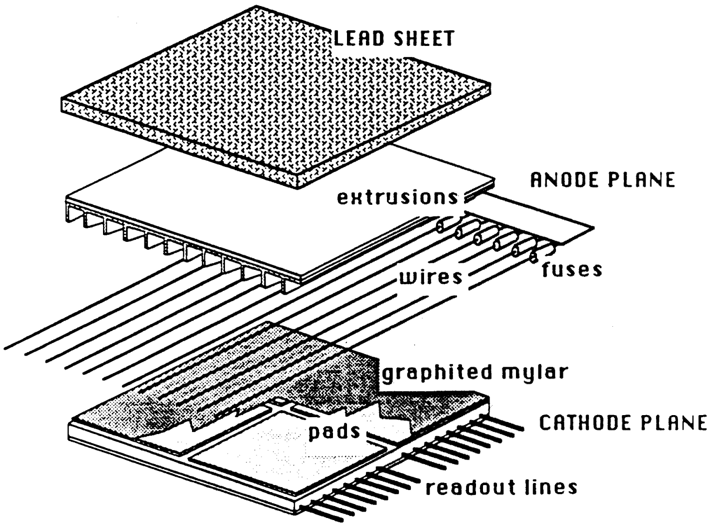

Figure 3.10: Detail of an ECAL layer.

3.5.2 Hadron Calorimeter and Muon Chambers

The Hadron Calorimeter (HCAL) measures the energy deposited by hadrons and the trajectories of muons. It is made from iron and also acts as the return flux of the magnet and the main mechanical support of the ALEPH detector. The HCAL structure is similar to that of ECAL, being made up of a barrel and two end caps, however it is slightly rotated with respect to ECAL so that the inactive "cracks" in the detectors do not overlap, as shown in Figure 3.11.

The principle of operation is also similar to that of ECAL, but the showers produced by hadrons propagate through nuclear processes rather than electromagnetic ones. Hadronic showers are generally more spread out laterally and also more penetrating, so the calorimeter must have a greater depth than ECAL. HCAL modules consist of 23 iron layers separated by plastic streamer tubes. These tubes are coated with graphite and contain eight wire counter cells. The tube layers are read out with pad electrodes that give an integrated energy measurement and with parallel digitising strips which are used to reconstruct the shower structure in $r\phi$ in the barrel. The pads are connected together to form projective readout towers pointing to the interaction point, as in ECAL.

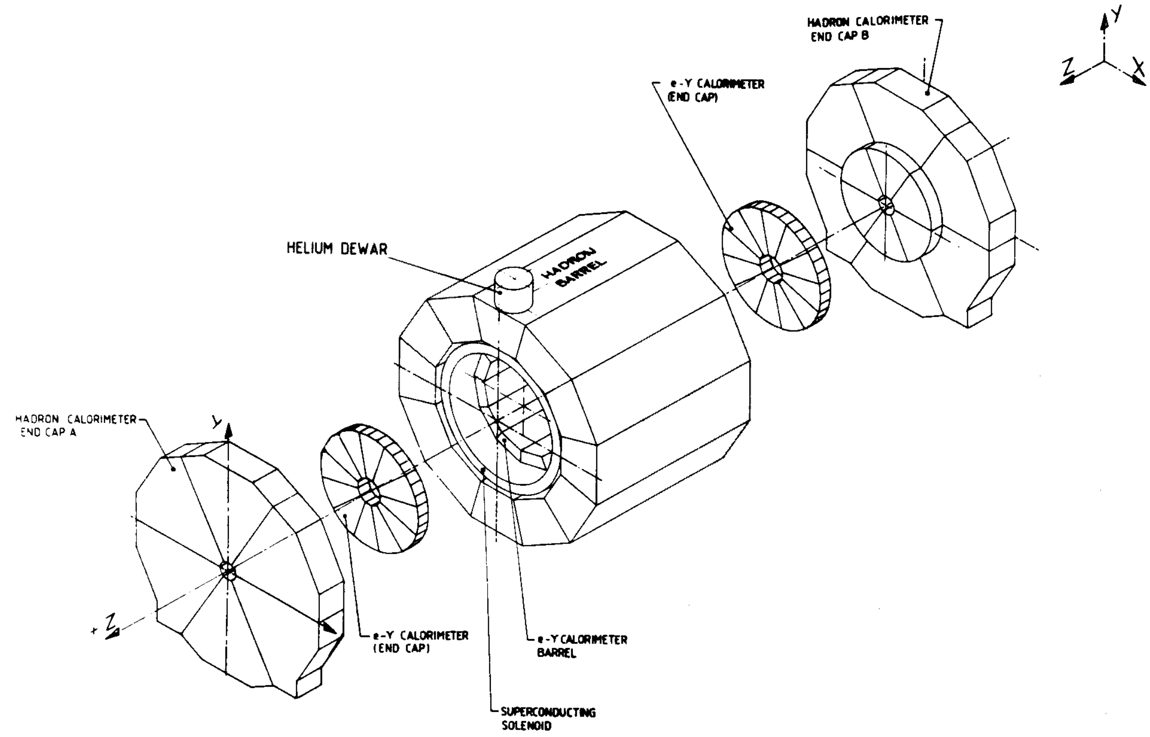

Figure 3.11: The ALEPH Hadron Calorimeter.

The energy resolution is obtained by studying pions at normal incidence, and is given by [48]:

$$\frac{\sigma(E)}{E} = \frac{0.84}{\sqrt{E(\mathrm{GeV})}} \,. \tag{3.5}$$

Muons have a characteristic signal in both the calorimeters. They leave a single trail of hits with no shower development. Outside the HCAL are two further planes of streamer tubes, known as muon chambers, which act as tracking detectors for muons. In the barrel they are radially separated by 0.5 m, which enables track segments to be measured with an accuracy of 10-15 mrad.

3.5.3 Luminosity Monitors

The instantaneous luminosity is defined as the ratio of the rate of $e^+e^- \rightarrow e^+e^-$ (Bhabha) interactions to the theoretical cross-section for this process, which is known with a high accuracy. The integrated luminosity is defined as the ratio of the number of these events in a certain time to the cross section. Its value is important in the calculation of observed cross sections, e.g. the Z^0 and W^+W^-

lineshapes. The cross section for Bhabha scattering is strongly peaked at polar angles close to the beam pipe, so to aid the cross section measurement three small specialist calorimeters are installed in this position in ALEPH.

The Luminosity Calorimeter (LCAL) is a lead-wire sampling calorimeter, similar in construction to the ECAL. The LCAL consists of two detectors covering a region with radii between 10 and 52 cm, situated at ±2.62 m from the IP, making it sensitive down to angles of $\sim 2.6^\circ$ from the beam direction. The luminosity is measured by counting Bhabha events which have the characteristic signature of symmetric back-to-back energy deposits. LCAL provides the primary luminosity measurement for ALEPH.

The Solid-State Luminosity Calorimeter (SiCAL) extends the coverage down to a polar angle of $\sim 1.4^\circ$. It consists of two detectors on either side of the IP that are constructed from 12 tungsten sheets separated by silicon pads. SiCAL provided the primary luminosity measurement for the LEP1 period of data taking, however, at the beginning of LEP2 low angle tungsten shielding was installed to protect the central trackers from the increased beam related background. This shielding obscures part of SiCAL, providing a source of systematic uncertainty in the luminosity measurement, and so it is now used to extend the coverage of the overall ALEPH calorimetry.

The Bhabha Calorimeter (BCAL) has two modules located 7.7 m from the interaction point, each consisting of 12 tungsten-scintillator layers. The rate of Bhabha events is much higher in BCAL due to its position, allowing higher statistical precision on the luminosity measurement. However, its position also places it close to a LEP focusing quadrapole magnet, making it more sensitive to beam related backgrounds and consequently the measurement has to be calibrated with LCAL. BCAL is therefore used to provide an instantaneous luminosity measurement and also to monitor the background conditions.

3.6 Data Collection and Reconstruction

3.6.1 Trigger

The bunch crossing rate of the electrons and positrons in LEP is of the order of 45 kHz, too high for ALEPH to record the result of every interaction. Most interactions are not in fact electron positron interactions but the result of interactions between the beam and gas in the accelerator or the scattering of off-momentum particles by collimators close to the IP. To reduce the amount of unwanted data recorded a trigger system is used. The trigger system is built in three stages, each stage using more information from the different sub-detectors in order to make an informed logical decision on whether to keep the data from a particular event. The three stages are summarised in Table 3.3.

Stage	Decision Time	Rate (Hz)	Information Used
Level 1	5 μs	Few 100	Hit Patterns in ITC Pad/wire readout from ECAL+HCAL+LCAL
Level 2	50 μs	10	TPC tracking
Level 3	62 ms	1-3	All sub-detectors

Table 3.3: Summary of the ALEPH trigger system.

The Level 1 trigger makes a quick decision on whether to wait for TPC trigger signals. If a Level 1 decision is negative then the readout system is stopped and reset ready for the next event and the TPC gate is closed, otherwise the TPC gate is left open and Level 2 checks that the tracks in the TPC originate from close to the IP. If a Level 2 decision is positive then the readout of the entire detector is initiated, otherwise the readout system is reset. Finally Level 3 looks at all the sub-detector information using an online analysis program. At the end of this process the rate of information is such that the events can easily be written to tape. The trigger system is highly efficient and flexible, being sensitive to both jets and single particles produced in electron positron collisions.

3.6.2 Data Acquisition

The ALEPH data acquisition system mirrors the ALEPH detector in that it is divided into modules for each sub-detector which readout those particular data, and then combines these data together to record the whole event.

The readout electronics for each sub-detector is synchronised with the bunch crossing by the Main Trigger Supervisor (MTS). The MTS communicates with each sub-detector's readout controller (ROC) via their Trigger Signal Receiver (TSR). The job of the ROC is to initialise the electronics for the sub-detector and to read out this electronics if a Level 2 decision is positive. At sub-detector level an event is built by the Event Builders (EB's), which pass the subevent onto the Main Event Builder (MEB). The MEB combines all the information about the event before passing it to an online computer. The Level 3 trigger then decides which events to keep by applying a basic event selection, before the event is stored on disk by the Main Readout Computer. Data are taken in a "run" which lasts either two hours or when 600 MB of data have been stored, whichever happens first. When a run is finished the data are written to tape.

3.6.3 Event Reconstruction

As soon as a run has been taken the events in that run are reconstructed fully. This is done using the Facility for ALeph COmputing and Networking (FALCON), running the ALEPH program `JULIA` [52]. This program converts the signals readout from the detectors into coordinates and energy deposits, which are then grouped, by pattern recognition software, into particle trajectories in the tracking chambers, as described in Section 3.4.4, and energy clusters in the calorimeters. Particle identification algorithms are also used on track and calorimeter information, as well as an energy flow algorithm, described in the next section, which uses all the information in an event to determine as well as possible the energy and momentum of individual particles and the whole event. The events are then stored in data files which can be read in by the `ALPHA` software package [53] to be used in physics analyses.

3.6.4 Energy Flow

The energy flow algorithm [48] uses the tracks and calorimeter information to reconstruct a set of energy flow "objects" for use in physics analyses. The overall energy resolution is improved by making use of as much information as possible to identify different particles. This includes track momenta, the TPC dE/dx information, the shape of the showers deposited in the calorimeters and the muon chamber information.

The algorithm uses only those tracks with at least four hits in the TPC, or eight hits in the TPC and one in the ITC if the momentum is greater than 15 GeV/c. The tracks must originate from a cylinder of length 20 cm and radius 2 cm round the IP, thus rejecting tracks coming from secondary decays or interactions, such as $\gamma \rightarrow \mathrm{e}^{+}\mathrm{e}^{-}$, which produce so-called V^0 secondary vertices. The absence of hits in the ITC is used as a cross-check for secondary vertices. Persistent noisy calorimeter channels are masked. Fake energy signals from noise in the detector are removed by checking the compatibility of pad and wire signals in the calorimeters.

Charged tracks are extrapolated through the calorimeters and matched to energy clusters to form a set of energy flow objects called "charged calorimeter objects". Electrons and muons are identified using the ECAL shower shape and the muon chambers, the remaining charged objects are treated as if they were pions. The energy of the charged objects is calculated using their track momenta and mass and subtracted from the calorimeter cluster energy.

The remaining energy clusters are then assumed to come from neutral particles. The ECAL shower shape is used to identify photons and π^0 particles. All other calorimeter clusters are attributed to neutral hadrons. Neutrino energies can be inferred from the missing energy in the event.

After this process a list of objects is produced which is expected to be a good representation of the true particles in the event. If the measured energy found in the calorimeters is summed with no regard for particle identification then the energy resolution is [48]:

$$\sigma(E) = 1.2\sqrt{E\,(\mathrm{GeV})} \tag{3.6}$$

for hadronic decays of the Z^0. After the algorithm has been run the resolution is [48]:

$$\sigma(E) = (0.59 \pm 0.03)\,\sqrt{E\,(\mathrm{GeV})} + (0.6 \pm 0.3)\ \mathrm{GeV}\,. \tag{3.7}$$

The list of objects produced by the energy flow algorithm is available for analysis, and in fact energy flow objects are used as the basis of the measurement described in this thesis.

3.7 Event Simulation

Crucial to the W mass analysis presented in this thesis and to many high energy physics experiments is the simulation of real data using Monte Carlo techniques. These simulated data (hereafter referred to as "Monte Carlo") are used to optimise and check the analysis at many stages, and many comparisons between data and Monte Carlo are carried out which lead to a better understanding of the analysis.

The simulation of data by ALEPH is carried out in three stages. Firstly, electron-positron interactions are simulated by one of many different programs according to the particular physics process under study. The programs used for this analysis are presented in the next section. This simulation is done under the ALEPH specific `KINGAL` framework [54], which ensures that the events are all produced with the same format to simplify further processing. The result of the simulation is the kinematics of all the particles in the final state. This information is passed to the second step in the process, the response of the ALEPH detector to the final state particles. This is done using the `GALEPH` program [55], based on `GEANT` [56]. `GALEPH` simulates interactions between the particles and the sub-detectors and the response of the sub-detectors to these interactions, producing an output which is the same as a real event. Finally the events are reconstructed using `JULIA` in the same way as real data to produce data files which can be analysed in exactly the same way. The only difference between data and Monte Carlo files is that the latter contain information about the true simulated process, thus enabling useful studies to be carried out.

3.7.1 Physics Generators

The simulation of an electron-positron event typically takes place in two stages. Firstly the underlying hard-scattering event is generated by one package, giving as output the leptons and quarks produced in the interaction. A second program is then used to perform the hadronisation of the event where the QCD processes involved are simulated. The output of this stage is a set of stable hadrons that may be seen in the detector. The Monte Carlo packages used in this thesis are now described.

Signal Processes

`KORALW` [57] version 1.21 [58] generates signal WW processes using either the `CC03` diagrams shown in Figure 2.1 or the set of four-fermion diagrams giving WW like final states computed using the `GRACE` package [59]. The four-fermion diagrams can be classified according to the final state of the process as shown in Table 3.4. The simplest cases, denoted by bold type in Table 3.4, are those diagrams involving either doubly or singly resonant W bosons only. For example, processes giving rise to a fully hadronic u$\bar{\text{d}}\bar{\text{c}}$s final state involve eleven such diagrams, known as the `CC11` diagrams. These consist of the three `CC03` diagrams and eight further diagrams similar to that shown in Figure 3.12, involving quark-antiquark production through a Z^0 or photon and then radiation of a W by one of the quarks. Additional *t*-channel diagrams have to be included for final states involving an electron and electron-neutrino. Final states involving particle-antiparticle pairs, denoted by italic type in Table 3.4, have additional diagrams involving Z boson pair production.

	$\bar{\text{d}}$u	$\bar{\text{s}}$c	$\text{e}^+\nu_\text{e}$	$\mu^+\nu_\mu$	$\tau^+\nu_\tau$
d$\bar{\text{u}}$	*43*	**11**	20	**10**	**10**
$\text{e}^-\bar{\nu}_\text{e}$	20	20	*56*	18	18
$\mu^-\bar{\nu}_\mu$	**10**	**10**	18	*19*	**9**

Table 3.4: The number of Feynman diagrams for WW like four fermion final states.

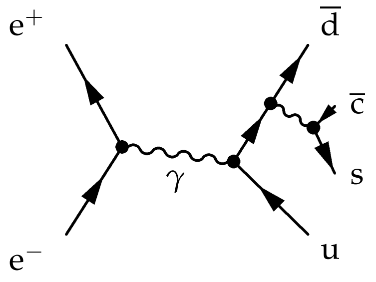

Figure 3.12: One of the `CC11` diagrams of four-fermion production.

Multiple initial state radiation photons with transverse momentum are simulated by `KORALW` using Yenni-Frautschi-Suura exponentiation, and final state radiation is generated with a separate package, `PHOTOS` [60]. The Coulomb correction is included.

Background Processes

`KORALZ` [61] is used to generate the major background to the fully hadronic WW decay, quark-antiquark production. `PYTHIA` [22] can also be used to generate this background along with Z^0Z^0 pair production and other minor backgrounds. Any WW like four-fermion final states are removed from the Z^0Z^0 sample to deal with the overlap with the `KORALW` WW sample, although this overlap is extremely small.

Hadronisation

Hadronisation is carried out by one of two packages. `JETSET` [22] is used for the standard Monte Carlo production, while `HERWIG` [23, 24] is used for systematic studies.

3.7.2 Other Samples

Additional Monte Carlo is used at $\sqrt{s} = 188.6$ GeV for studies of the systematic uncertainties on the W mass measurement, in particular for the studies of the final state interactions. This is described in detail in Section 7.7.

Monte Carlo Used

The number of Monte Carlo events generated is typically far greater than the number expected in the real data. A summary of the Monte Carlo data used for this analysis is shown in Table 3.5.

Generator	Cross Section (pb)	Events Generated $\times 10^3$	Equivalent Luminosity (fb^{-1})
$\sqrt{s} = 188.6$ GeV			
`KORALW` WW 4f M_W = 80.35 GeV/c^2	16.9	1000	60
`KORALW` WW 4f M_W = 79.35–81.35 GeV/c^2		500	30
`KORALW` WW `CC03` M_W = 80.35 GeV/c^2	16.7	150	9
`KORALZ` $\mathrm{q\overline{q}}$	100.3	600	6
`PYTHIA` $\mathrm{Z^0\,Z^0}$	2.8	90	32
$\sqrt{s} = 192$ GeV			
`KORALW` WW 4f	17.3	100	5.8
`KORALZ` $\mathrm{q\overline{q}}$	95.8	500	5.2
`PYTHIA` $\mathrm{Z^0\,Z^0}$	2.8	50	17.7
$\sqrt{s} = 196$ GeV			
`KORALW` WW 4f	17.6	200	11.4
`KORALZ` $\mathrm{q\overline{q}}$	91.0	500	5.5
`PYTHIA` $\mathrm{Z^0\,Z^0}$	2.9	50	17.5
$\sqrt{s} = 200$ GeV			
`KORALW` WW 4f	17.8	200	11.2
`KORALZ` $\mathrm{q\overline{q}}$	86.6	1000	11.5
`PYTHIA` $\mathrm{Z^0\,Z^0}$	2.9	50	17.5
$\sqrt{s} = 202$ GeV			
`KORALW` WW 4f	17.9	200	11.2
`KORALZ` $\mathrm{q\overline{q}}$	84.5	500	5.9

Table 3.5: Summary of the main Monte Carlo samples used in this thesis.

Chapter 4

Event Selection

4.1 Signal and Background Characteristics

The first step in the measurement of the W mass is to select those electron positron interactions in which W pairs have been produced, while rejecting events involving other physics processes. The hadronic WW events are known as "signal" and all other events as "background". A schematic of a fully hadronic W pair event is shown in Figure 4.1, while an ALEPH event display of a fully hadronic WW candidate is shown in Figure 4.2. Fully hadronic events are characterised by the production of at least four jets of hadronic particles, and therefore have a large multiplicity and a spherical topology. There should be little missing energy in the event, and so the total energy should be close to the LEP centre of mass energy.

There are several different physics processes that can give final states similar to the fully hadronic WW decay, and consequently these may be selected falsely as an hadronic WW event. In decreasing order of importance, these are:

$$\mathrm{e^+e^-} \rightarrow \mathrm{q\overline{q}}$$

$$\mathrm{e^+e^-} \rightarrow \mathrm{Z^0Z^0}$$

$$\mathrm{e^+e^-} \rightarrow \mathrm{W^+W^-} \rightarrow \mathrm{q\overline{q}}\ell\nu$$

$$\mathrm{e^+e^-} \rightarrow \mathrm{Z^0e^+e^-}$$

$$\mathrm{e^+e^-} \rightarrow \mathrm{W^+W^-} \rightarrow \ell\nu\ell\nu$$

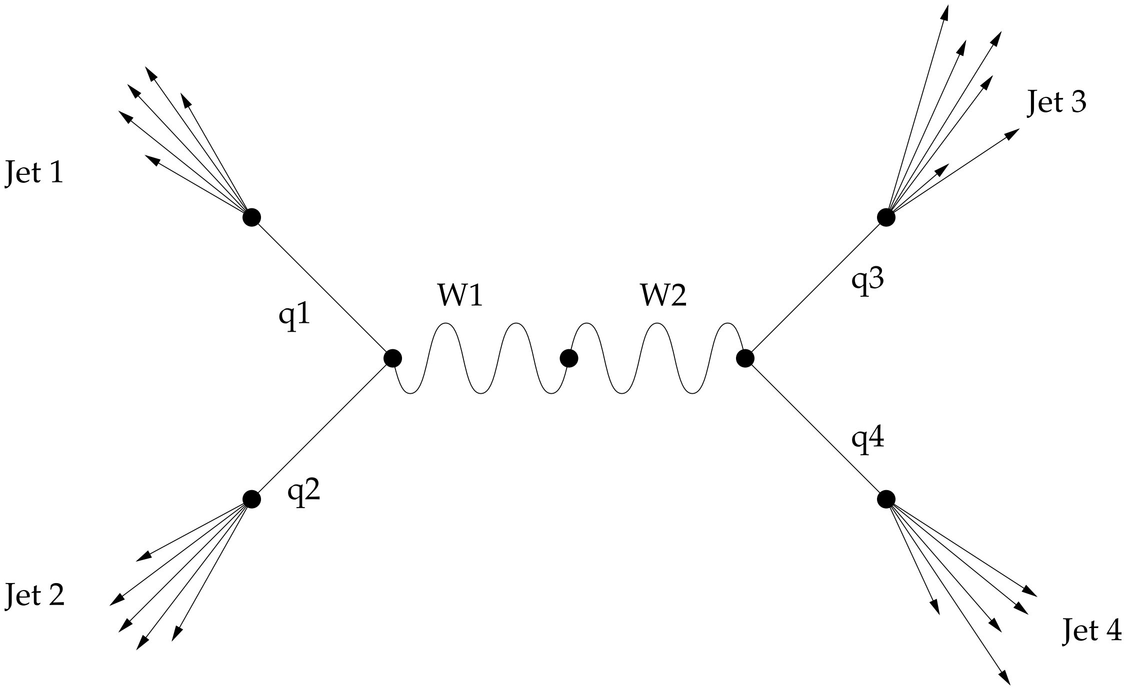

Figure 4.1: A schematic fully hadronic event.

The biggest contribution to the background comes from the $q\overline{q}$ process, which has a cross section of over 100 pb compared with the WW production cross section of 17 pb. Over 50% of $q\overline{q}$ events are characterised by radiative return to the Z^0 resonance. In these events enough energy has been emitted by the incoming electron and positron through initial state radiation that their centre of mass energy is equal to the Z^0 mass. Such events have a large amount of missing energy and an invariant mass close to the Z^0 mass, or in some cases the ISR photon is produced in the detector acceptance and a large amount of isolated electromagnetic energy is seen. A large number of $q\overline{q}$ events do not possess the typical four jet topology of hadronic WW events, instead they have a longitudinal two jet structure. Semileptonic WW decays are characterised by having one energetic lepton that is usually isolated from the two jets produced. They also have a large amount of missing energy due to the presence of a neutrino which is not detected by ALEPH. Fully leptonic W pair events are characterised by two energetic leptons and a large amount of missing energy. Z^0Z^0 events have many different final states, the ones important to this analysis are the fully hadronic decays in which both Z^0 decay to a pair of quarks.

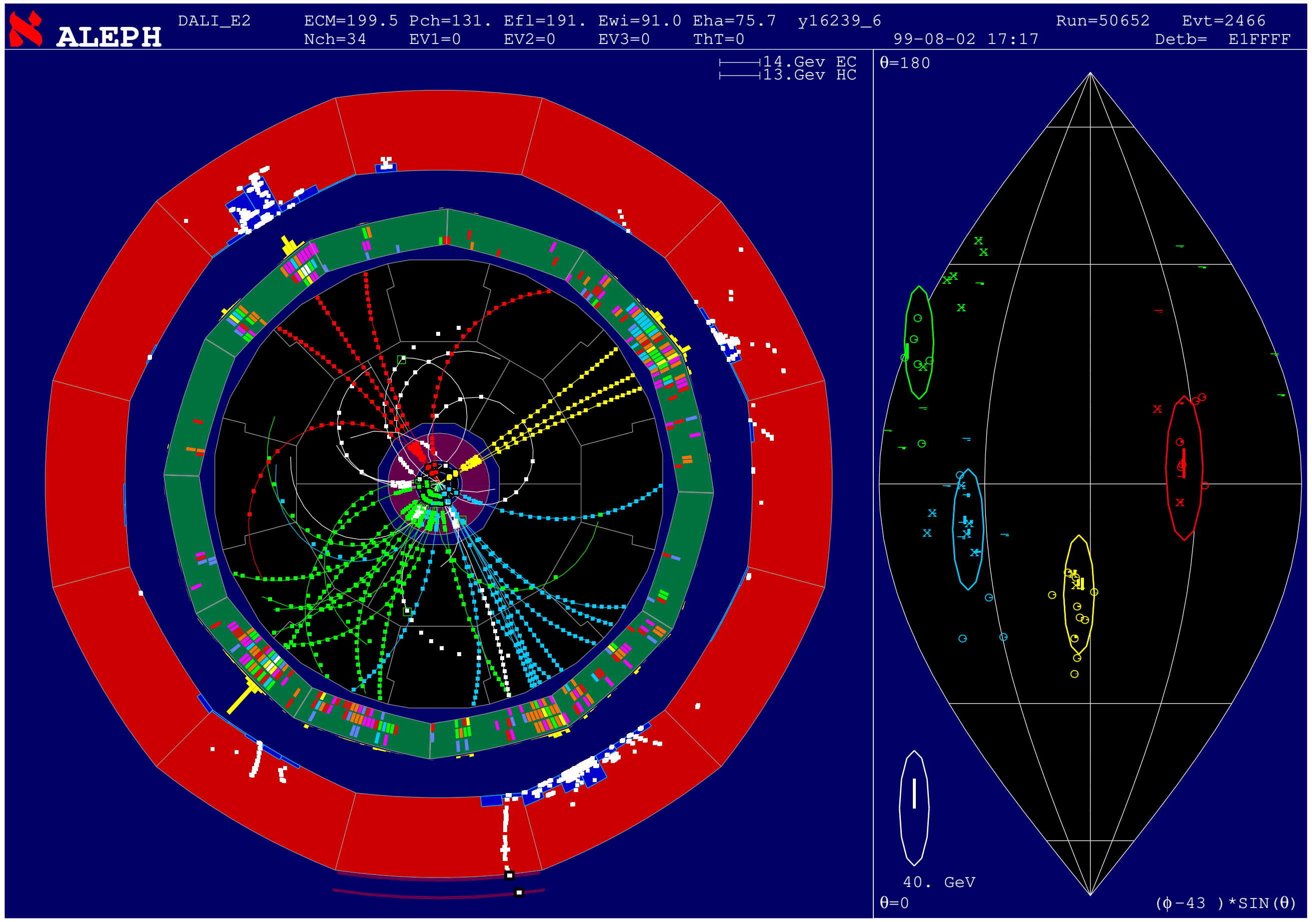

Figure 4.2: A fully hadronic WW candidate event. The four jets are coloured differently as a visual aid. The left hand view is an $r\phi$ projection of the ALEPH detector. The TPC is represented by the large black area showing the charged particle trajectories. The ITC is shown in purple in the centre. The ECAL is shown in green, the amount of energy deposited being indicated by yellow histograms. The HCAL is the outermost sub-detector shown in red, with energy deposited indicated by the blue histograms. The right hand view is a $\theta\phi$ view showing energy flow objects. The four jets are clearly seen.

The goal of the event selection is to use the different characteristics of the signal and background events to construct an algorithm that can differentiate as much as possible between them. The algorithm should have a high efficiency for selecting fully hadronic W pair events, and also a high purity, that is with little contamination from background processes.

4.2 Selection

The selection of hadronic WW events is carried out in two stages. First a rough preselection is used to remove a large proportion of background events that are clearly not signal-like, then a more complicated selection algorithm is used to separate signal from the remaining background. The rest of this chapter describes these two steps in more detail.

4.2.1 Preselection

The preselection is designed to remove as much background as possible without removing signal events, using simple criteria. Selection requirements are applied to several variables in turn, events being removed at each stage. The criteria used are as follows:

- "`CLASS16`". At the event reconstruction stage the events are classified according to different criteria in order to simplify later analysis. `CLASS16` was originally designed to select hadronic events at the Z^0 resonance, but it can equally be applied in this analysis. All `CLASS16` events must have at least five good charged tracks within the detector acceptance, and the total energy of all charged tracks must be at least 10% of the LEP centre of mass energy. A good track must have at least four hits in the TPC and come from a region close to the interaction point that is defined by a cylinder of radius 2 cm and length 20 cm. The polar angle of the track must also satisfy $|\cos\theta < 0.95|$. The `CLASS16` requirement removes low multiplicity background events such as fully leptonic WW events, but also events not originating from e^+e^- collisions such as beam-gas, beam-beampipe interactions and cosmic rays.

- $|p_z| < 1.5\,(M_{vis} - M_Z)$, where p_z is the z component of the total momentum of all the energy flow objects observed in the event. M_{vis} is the total invariant mass of all energy flow objects. This criterion removes radiative returns to the Z^0 resonance in $q\overline{q}$ events.

- $y_{34} > 0.001$. y_{34} is the value of the jet clustering parameter y_{cut} where the transition between three and four jets takes place. The parameter y_{cut} is described in more detail in Section 5.1. This requirement selects events which look more like four jet events, rather than the two and three jet like $q\overline{q}$ events. At this stage the events are forced into four jets using the `DURHAM PE` algorithm as described in Section 5.1.

- The fraction of the jet energy due to charged objects must be less than 90% of the total energy in the jet. This requirement rejects semileptonic WW events, which often contain a highly energetic isolated charged lepton that has been classed as a jet.

- The energy belonging to electromagnetic particles in a 1° cone around any particle must be less than 95% of the total energy in that cone. This requirement rejects events in which an initial state radiation photon is produced within the detector acceptance.

The cumulative effects of the preselection criteria on the 1998 high energy data sample (see Table 3.1) after `CLASS16` selection are shown in Figure 4.3. Also shown in Figure 4.3 are the same distributions obtained from the `KORALW` WW, `KORALZ` $q\overline{q}$ and `PYTHIA` Z^0Z^0 and $Z^0e^+e^-$ Monte Carlo data samples generated at $\sqrt{s} = 188.6$ GeV listed in Table 3.5. The Monte Carlo distributions have been normalised to the observed data luminosity and are divided into WW signal, that is all fully hadronic WW events, WW background, and all other backgrounds. Good agreement is observed between data and Monte Carlo in the signal region. The selection criteria applied are shown on the plots by arrows. The performance of the preselection is shown in Table 4.1. The preselection criteria give a sample which is $\sim 37\%$ pure with negligible loss of hadronic WW events. Good agreement is seen between the expectations, for signal plus background, Monte Carlo and the observed number of events remaining in the data.

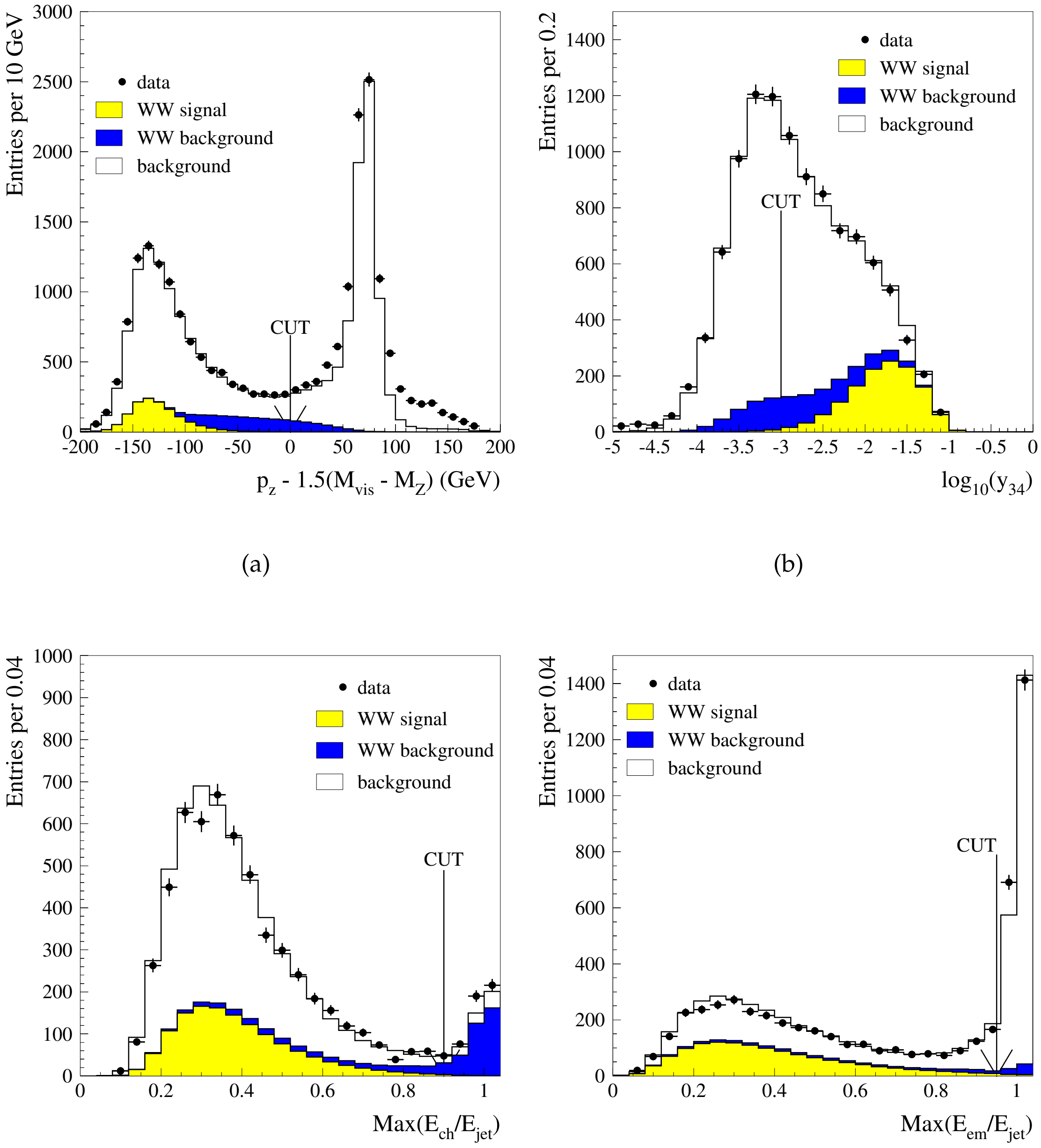

(a)

(b)

(c)

(d)

Figure 4.3: The preselection variables (see text) for the $\sqrt{s} = 188.6$ GeV data and Monte Carlo.
(a) $|p_z| < 1.5\,(M_{vis} - M_Z)$ distribution after `CLASS16` selection.
(b) y_{34} distribution for data surviving the cut illustrated in Figure (a).
(c) $\max\left(E_{ch}/E_{jet}\right)$ distribution for data surviving the cut illustrated in Figure (b).
(d) $\max\left(E_{em}/E_{jet}\right)$ distribution for data surviving the cut illustrated in Figure (c).

Selection Criteria	Efficiency (%)	Purity (%)	Events Expected	Events Observed
`CLASS16`	100.0	7.0	18972	21724
$\lvert p_z \rvert < 1.5\,(M_{vis} - M_Z)$	99.6	12.6	10546	10849
$y_{34} > 0.001$	98.6	22.0	5991	5955
$\max\left(E_{ch}/E_{jet}\right) < 0.9$	98.3	23.7	5545	5451
$\max\left(E_{em}/E_{jet}\right) < 0.95$	97.4	37.4	3485	3293

Table 4.1: Performance of the preselection criteria, applied cumulatively to `CLASS16` events for the $\sqrt{s} = 188.6$ GeV data and Monte Carlo.

4.2.2 Neural Networks

After the preselection a sample of events is obtained in which signal and the remaining background events have more similar characteristics. To separate the events a more sophisticated algorithm has to be used that takes into account several different properties of the event at once. Such a multivariate technique is now common in event selection for high energy physics, combining different variables in some way to give a single number as output. This number gives an indication of how probable it is that a particular event is signal or background. Several multivariate techniques exist, however previous studies at lower centre of mass energies [62, 63] have indicated that the optimal method for selecting fully hadronic WW pair events is to use a neural network.

Neural networks are widely used in pattern recognition problems with a large number of variables, as in the case of event selection. Neural networks may be expected to have a better performance than other multivariate techniques because variables are combined in a non-linear fashion, ensuring that the correlations between the variables are taken into account.

A typical neural network as used for event selection is generally a feed forward network consisting of several layers of neurons. This means that each neuron in a particular layer is directly connected to each neuron in the following layer, but there are no connections between the neurons in the same layer. The first layer is the input layer and consists of one node for each of the variables under consideration. These are then connected to neurons in the first hidden layer, and so on according to how many layers are used. One or two hidden layers are typical. Finally each of the neurons in the last hidden layer is connected to the output layer, which for event selection purposes generally consists of just one node giving as output a number that usually varies between zero and unity. The higher the number the more likely an event is to be a signal event. The output from each of the neurons is a non-linear function of the weighted sums of the inputs to it. A typical neural net architecture is shown in Figure 4.4.

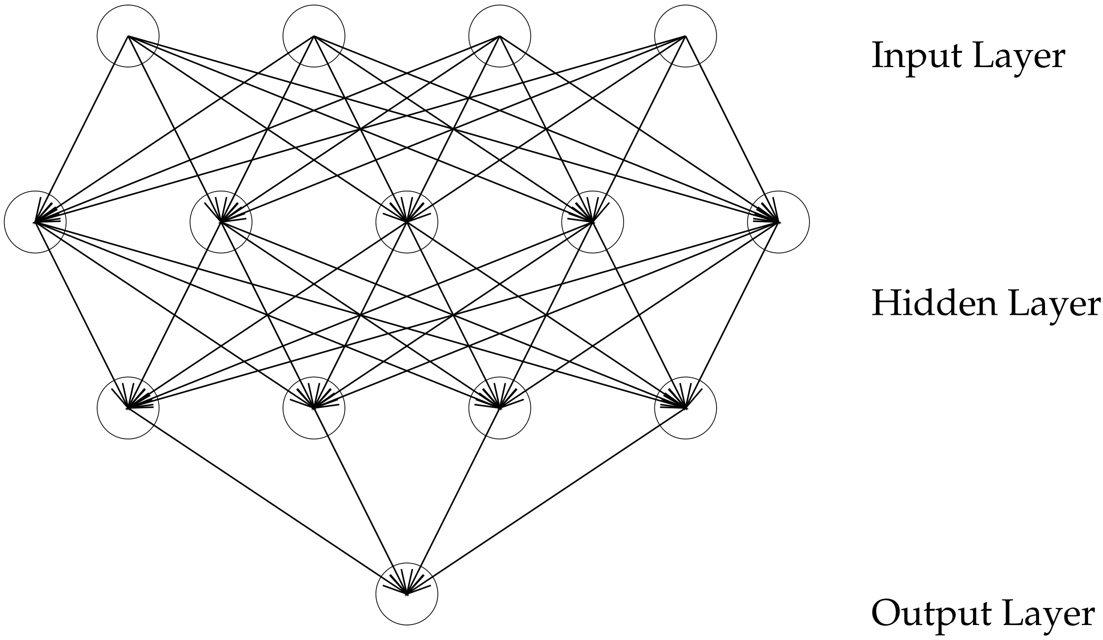

Figure 4.4: The architecture of a typical neural network.

Neural Net Training

One of the most important steps in the use of neural networks is the training of the network to differentiate signal and background events. This is when the weights of the connections between the different neurons are determined. Samples of Monte Carlo signal and background events are used to perform the training. For each event in the Monte Carlo data sample the values of the variables used as input to the neural network are calculated. These values are then input to the network along with an indication of whether the event is signal or background. The weights are then varied in order to minimise the error function, which for a network with a single output node is defined as:

$$E = \sum_{i=1}^{N} (O_i - d_i)^2 \ , \tag{4.1}$$

where N is the number of events in the training sample, O_i is the output of the neural network for event i and d_i is the desired output, typically zero for background and unity for signal events. The minimisation is carried out in an iterative process, using the gradient descent method.

Once the weights have converged to stable values then the performance of the neural network has to be validated. This is carried out using different samples of Monte Carlo events to those used for training. The classification of the event is not provided to the neural network as input, but instead is compared with the output. Once this has been done then the neural network is ready to be used for the classification of real data events.

Neural Net Input Variables

Neural networks are only useful for event classification if the information provided to them has some discriminating power between signal and background. The choice of variables to use is thus important and not necessarily straightforward due to correlations between variables. Studies have shown that good performance can be obtained with the use of 14 different variables [63, 64], relating to global event properties, properties of individual jets, and WW kinematics. These variables are listed in Figure 4.5.

Since the training of the neural network is performed using Monte Carlo events, it is important that there is good agreement between data and Monte Carlo, particularly in those variables that are used as input to the net. This agreement has been checked and is shown in Figures 4.6–4.9 for events surviving the preselection criteria. The data and Monte Carlo sample used are the same as that for Figure 4.3.

Neural Net Performance

The output of the neural network is shown in Figure 4.10 for 188.6 GeV data and Monte Carlo. It can be seen that the output peaks at zero and unity pro-

Global Variables	1	Thrust†
	2	Sphericity†
	3	Missing Energy
Jet Properties	4	Maximum electromagnetic energy fraction of a jet in any 1 degree cone
	5	Maximum charged track energy fraction of a jet
	6	Minimum number of charged particles in a jet
WW Kinematics	7	Sum of the four smallest interjet angles
	8	Angle between 2nd and 3rd jets (ordered by decreasing energy)
	9	Maximum jet energy
	10	2nd minimum jet energy
	11	Minimum jet energy
	12	2nd minimum jet mass
	13	Minimum jet mass
Flavour Tagging	14	Probability of an event to be a light quark (uds) event based on impact parameter significance of charged particles in the event (anti b-tag)

Figure 4.5: The 14 variables used as input to the neural network. The variables labelled with † are defined in Appendix A.

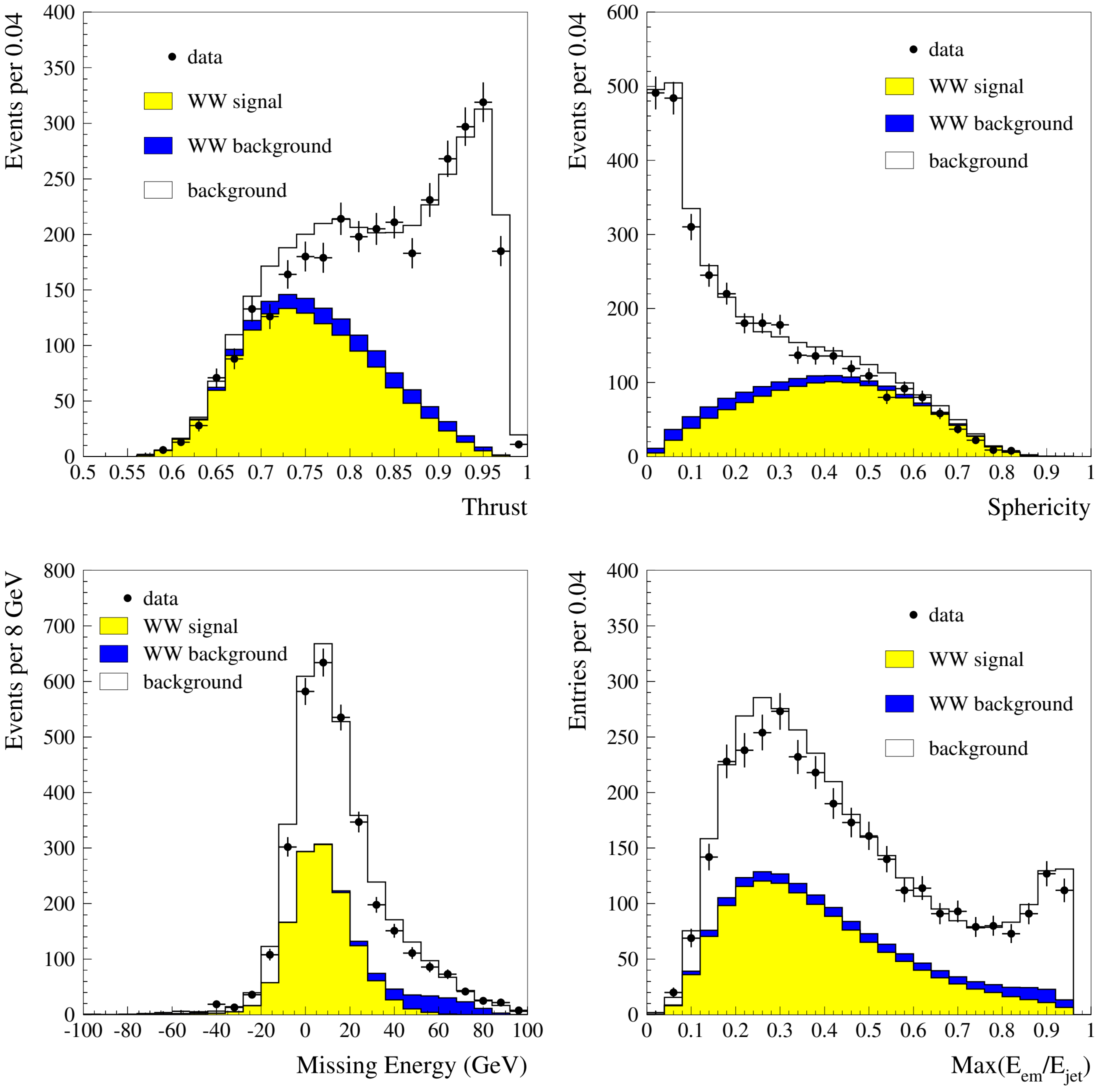

Figure 4.6: Neural network variables 1–4, (see text). The open histogram represents the total Monte Carlo expectation, the contribution from WW Monte Carlo is shaded. Data are shown as points.

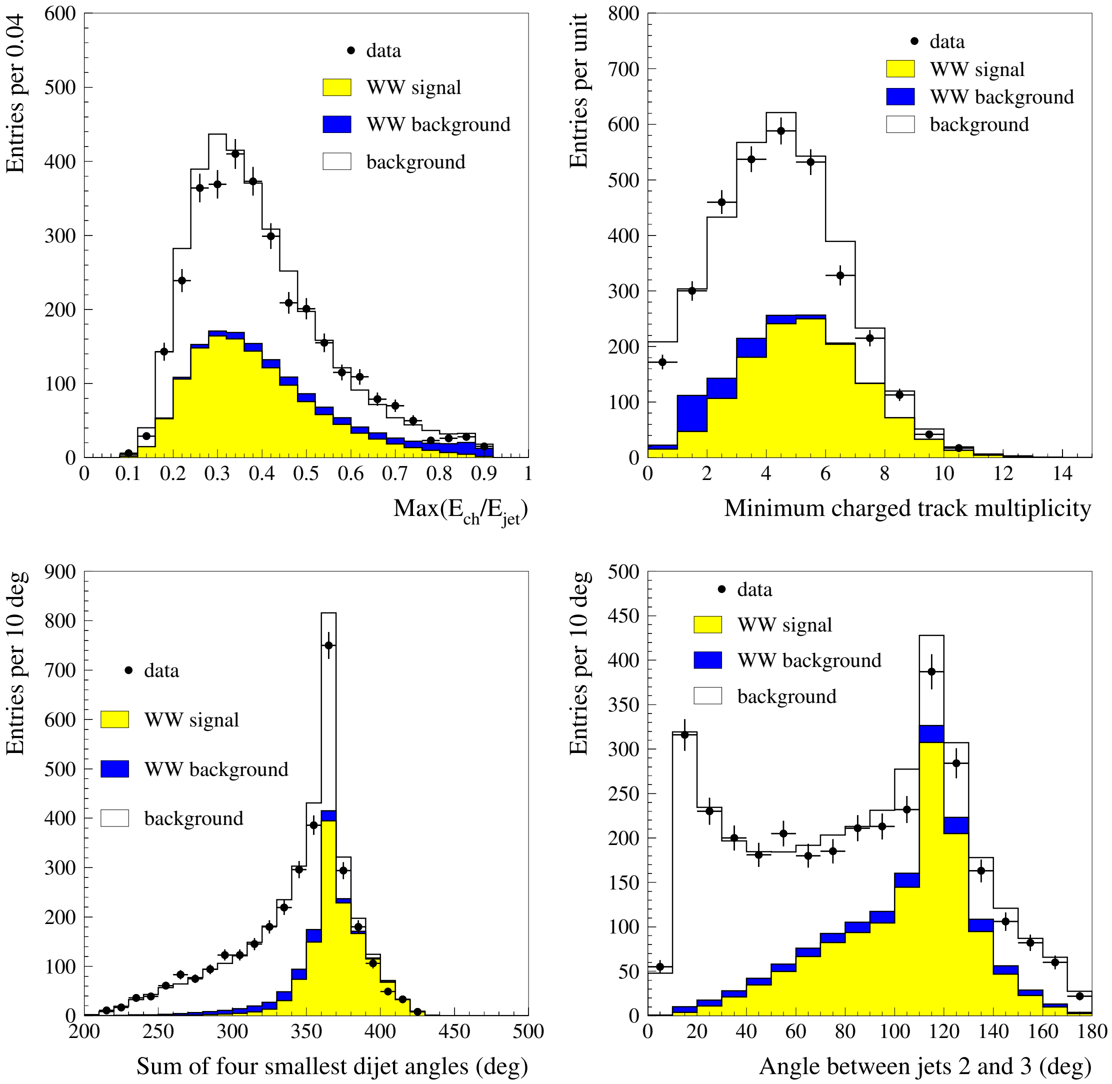

Figure 4.7: Neural network variables 5–8, (see text). The open histogram represents the total Monte Carlo expectation, the contribution from WW Monte Carlo is shaded. Data are shown as points.

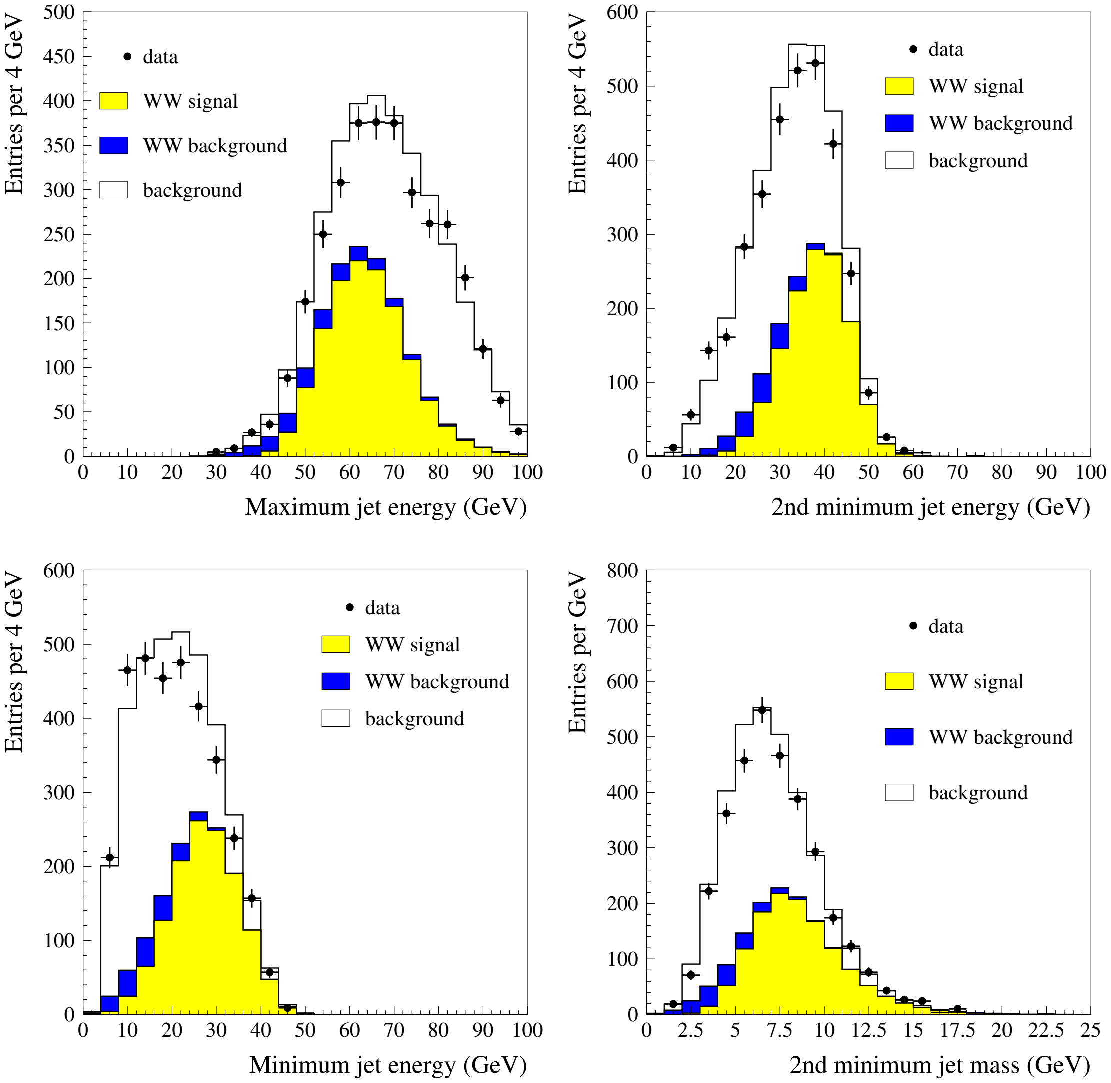

Figure 4.8: Neural network variables 9–12, (see text). The open histogram represents the total Monte Carlo expectation, the contribution from WW Monte Carlo is shaded. Data are shown as points.

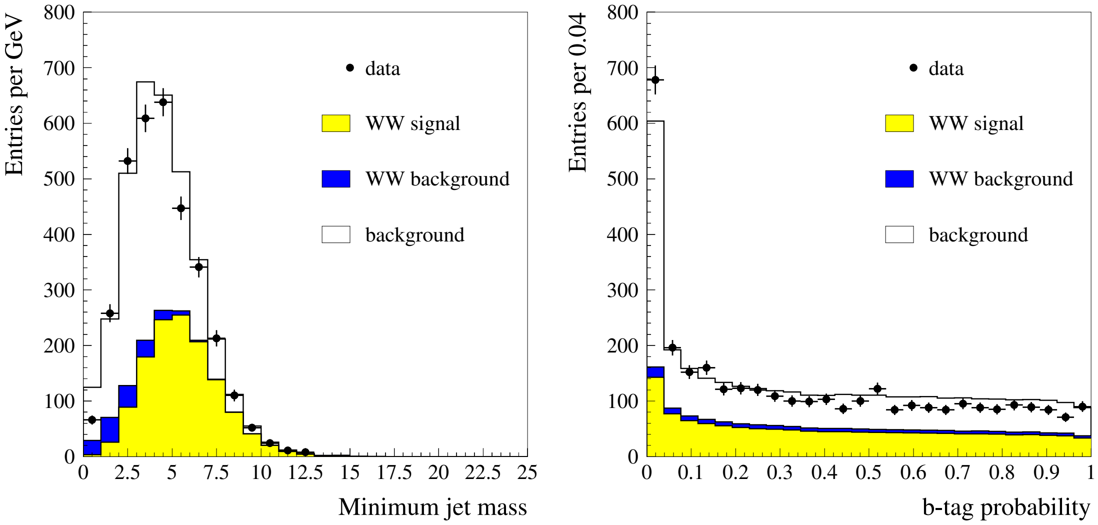

Figure 4.9: Neural network variables 13–14, (see text). The open histogram represents the total Monte Carlo expectation, the contribution from WW Monte Carlo is shaded. Data are shown as points.

viding good separation between signal and background events. There is reasonable agreement between data and Monte Carlo except for the most signal like bin where there are less events observed than expected. To perform the separation a value of the neural net output variable is chosen above which events are kept and below which events are rejected. The performance of the neural network may be evaluated using its efficiency, $\mathcal{E}$, for selecting signal events and the purity, $\mathcal{P}$, of the event sample selected. These two variables may be combined into one variable, the quality, defined as:

$$\mathcal{Q} = \sqrt{\mathcal{E}\mathcal{P}}\,. \tag{4.2}$$

These three variables are illustrated in Figure 4.11, showing their dependence on the value of the selection criteria applied to the neural network output. It can be seen that the quality is reasonably flat over a wide range. One may also look at the expected statistical uncertainty for the W mass measurement described in this thesis as a function of the cut on the neural network output, the goal being to minimise this uncertainty. This is illustrated in Figure 4.12, and again is rather flat. A value of 0.3 for the neural network output was chosen as the criteria for deciding whether or not to keep events. The performance of the selection at each centre of mass energy is shown in Table 4.2. A small decrease in performance is observed as the centre of mass energy increases. This can be explained by the fact that the training of the neural network was carried out at $\sqrt{s} = 188.6$ GeV. The table also shows that the number of events observed is less than the number of expected events for all energies except $\sqrt{s} = 191.6$ GeV, as expected from Figure 4.10. This observation is confirmed by the measurement of the WW cross section [64] which is 5.5% lower than the `GENTLE` [65] prediction. Many studies were performed to try and understand this discrepancy, mainly based on using different selection algorithms. These included a different neural network with nineteen variables, a six variable neural network based on charged track information only and a linear discriminant with six input variables based purely on calorimeter information. Several linear discriminants with between four and sixteen variables were also used. All of these various selection algorithms give a measured cross section at 188.6 GeV that is consistently lower than the `GENTLE` prediction. Recently, however, new calculations which include full $\mathcal{O}(\alpha)$ electroweak corrections calculable in the double pole approximation [66] have become available from two Monte Carlo programs, `YFSWW3` [67] and `RacoonWW` [68]. These calculations predict a cross section some 2–2.5% lower than the `GENTLE` calculation. Unfortunately these Monte Carlo programs could not be used to generate events for this analysis, however the effect on the fitted mass of observing less events than expected is very small since the measurement depends upon the shape of the invariant mass distribution and not the normalisation.

$\sqrt{s}$ (GeV)	$\mathcal{E}$ (%)	$\mathcal{P}$ (%)	$\mathcal{Q}$ (%)	Events Expected	Events Observed
188.6	90.6	79.8	85.0	1519	1426
191.6	89.9	79.3	84.4	256	276
195.5	89.4	78.3	83.7	728	706
199.5	88.5	77.2	82.6	797	772
201.6	88.2	77.0	82.4	388	352

Table 4.2: Performance of the selection after requiring a neural network output greater than 0.3. A small decrease in performance is observed as the centre of mass energy increases, as explained in the text.

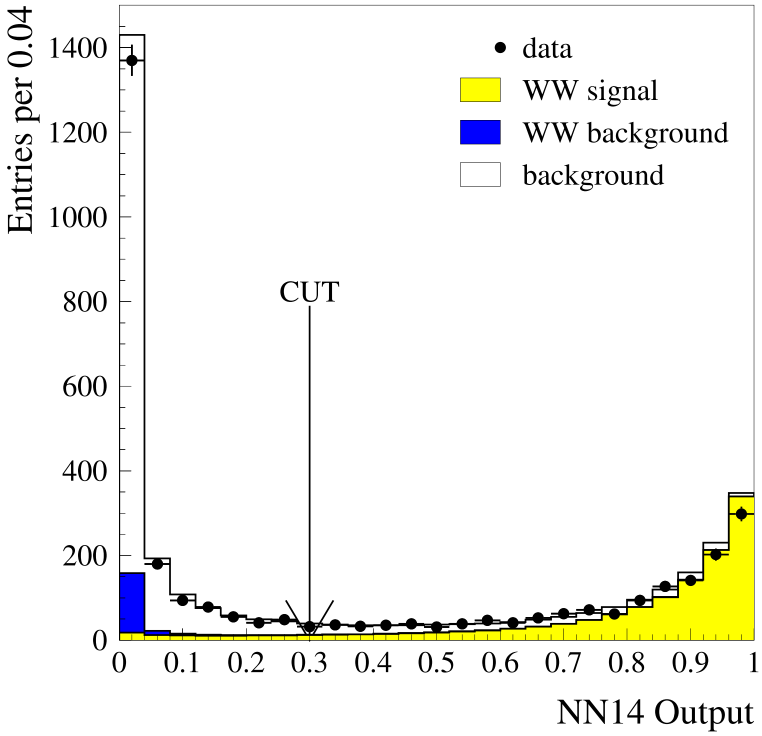

Figure 4.10: The output of the neural network, showing the discrimination between signal and background events.

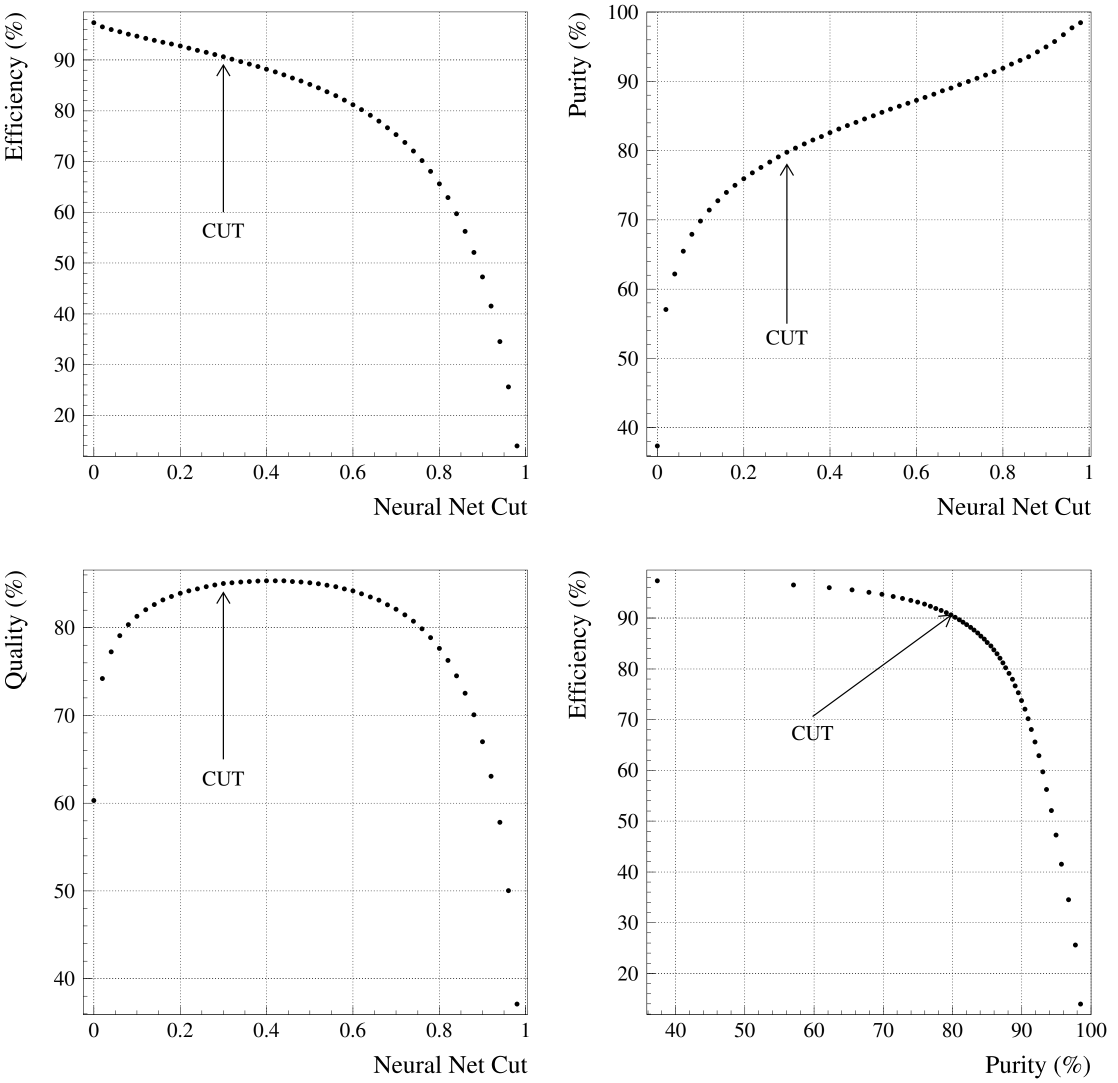

Figure 4.11: Efficiency, purity and quality of the neural network as a function of the cut on the output value. The final plot shows the efficiency as a function of the purity. The selection criteria used in the analysis is indicated by the arrow in each plot.

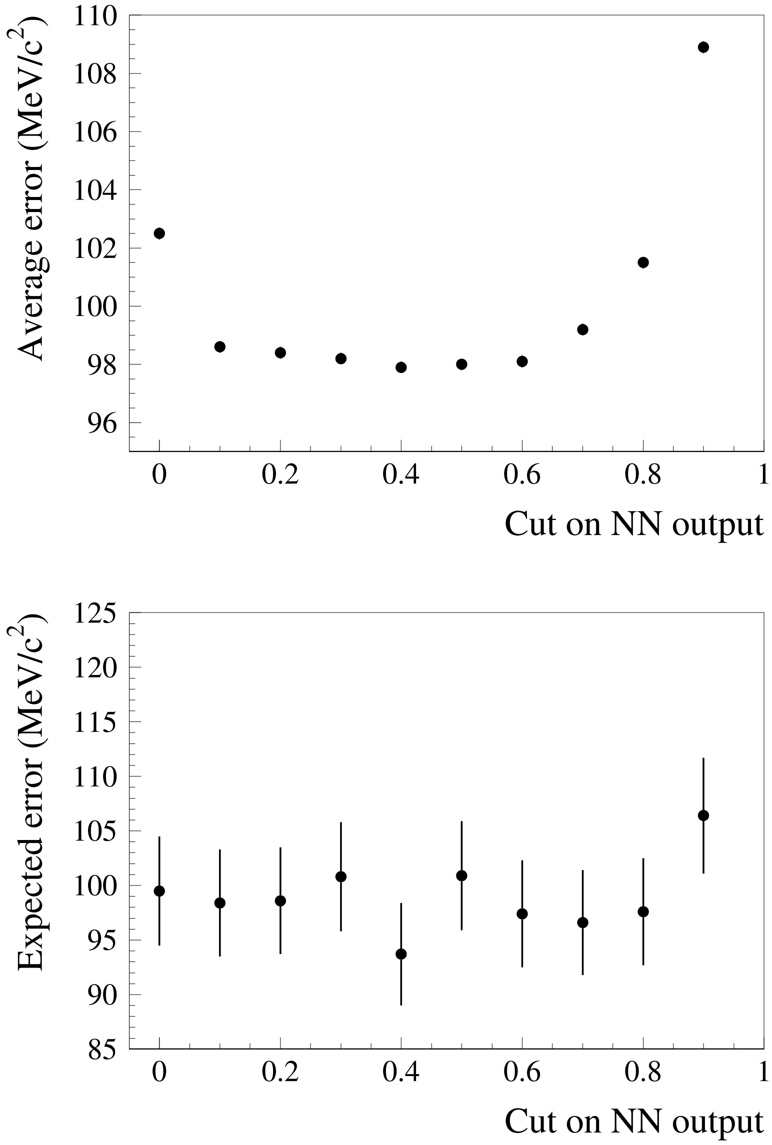

Figure 4.12: The expected statistical uncertainty on M_{W} as a function of the cut on the neural network output. The top plot is the average W mass error for 200 Monte Carlo samples the same size as the data, the bottom plot is the r.m.s. of the mass distribution for the same samples.

Neural Net Checks

An important quality of any event selection must be that it does not bias the measured W mass by having a mass dependent efficiency. This can be checked using several Monte Carlo samples generated with different W masses. The results of the check are shown in Figure 4.13, where it can be seen that any dependence on the input W mass is very small. The second point to be checked is that the choice of the value of the cut on the neural network output does not bias the measured W mass. This is checked using Monte Carlo of a known input W mass, and is shown in Figure 4.14. No bias is observed.

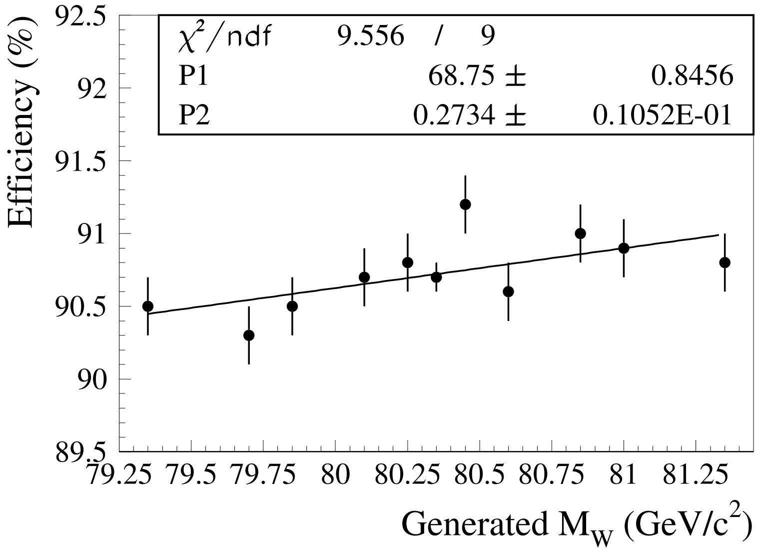

Figure 4.13: The neural network efficiency as a function of W mass value input to the Monte Carlo. Little dependence on the W mass is seen. The parameters P1 and P2 are the offset and slope of a straight line fit to the data in the plot. The χ^2/ndf of the fit is also given.

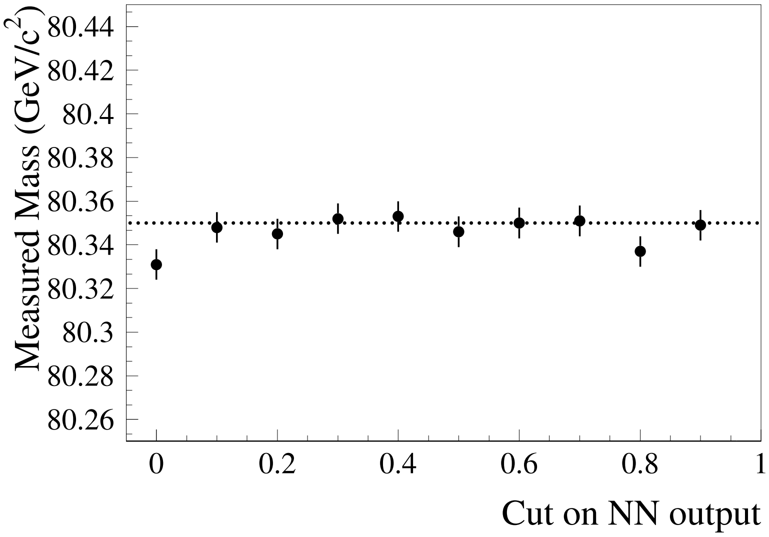

Figure 4.14: The measured W mass for a sample of Monte Carlo as a function of the cut on the neural network output. The true W mass is 80.35 GeV/c^2, as shown by the dotted line.

Chapter 5

Event Reconstruction

Once W pair candidate events have been selected all the individual particles observed in the ALEPH detector must be associated with one or the other of the two W bosons produced in the event, the aim being to to form variables from which the W mass may be extracted. The most obvious of these variables is the invariant mass:

$$M_{inv}^2 = \left(\sum_{i=1}^{n} E_i \right)^2 - \left(\sum_{i=1}^{n} \vec{p}_i \right)^2 , \tag{5.1}$$

where the sum is carried out over each particle assigned to the W in question.[1] This process is known as event reconstruction and takes place in several steps, each of which is described in detail in the following sections. Unless otherwise stated all the studies in this chapter have been performed using 188.6 GeV data and Monte Carlo.

5.1 Jet Clustering

The first step in event reconstruction is to cluster the individual objects produced in an event into so called "jets". The goal of jet clustering is to reproduce as closely as possible the jets resulting from the hadronisation process of the quarks produced by the decay of the W bosons. In the fully hadronic decays considered in this thesis four primary quarks are produced and so in general four jets of particles may be expected. Events selected as fully hadronic WW candidates are

---

[1] In this analysis the particles are the energy flow objects described in Section 3.6.4.

thus forced to form four jets. Hard gluon radiation takes place in a fraction of events however, leading to five or even six jet final states. A separate treatment of these events is not considered in this thesis but may be the source of future improvements to the analysis.

5.1.1 Jet Clustering Algorithms

Several algorithms exist to carry out the process of jet clustering, but most use a similar procedure. A "distance parameter", y_{ij}, is calculated between each pair of objects i and j in the detector. The pair with the minimum value of this parameter are combined to form a new pseudo-particle by adding their momenta. This minimisation step is repeated until y_{ij} is greater than some predefined cut-off value, y_{cut}. The pseudo-particles remaining at this stage are considered to be the jets. The distance parameter y_{ij} can be defined in many ways, and it is this definition that distinguishes different jet clustering algorithms. Usually y_{ij} is defined as some mass variable, M^2_{ij}, scaled by the visible energy in the detector:

$$y_{ij} = \frac{M^2_{ij}}{E^2_{vis}} \,. \tag{5.2}$$

The definitions of M^2_{ij} used in different jet clustering algorithms are shown in Table 5.1.

Algorithm	Mass Variable M^2_{ij}
`JADE`	$2E_iE_j\left(1-\cos\theta_{ij}\right)$
`DURHAM`	$2\left(\min\left[E_i^2, E_j^2\right]\right)\left(1-\cos\theta_{ij}\right)$
`GENEVA`	$\frac{8}{9}E_iE_j\left(1-\cos\theta_{ij}\right)/\left(E_i+E_j\right)$

Table 5.1: Definition of the mass variable M^2_{ij} for different jet clustering algorithms.

The first jet clustering algorithm was developed by the `JADE` collaboration [69]. This algorithm uses the invariant mass of the two objects, calculated assuming the objects are massless. The disadvantage of this approach is that two low energy objects can be clustered together even if they have a large opening angle. The algorithm may then not be sensitive to gluon jets which tend to be softer than quark jets. The `DURHAM` algorithm [70] in effect evaluates the transverse momentum of the lower energy object with respect to the higher one, making it more sensitive to gluon radiation. The `GENEVA` algorithm [71] is similar to the `DURHAM` algorithm.

Each of the different clustering algorithms may be modified by using different methods to calculate the jet four momentum. These schemes are summarised in Table 5.2. The `P` and `E0` schemes form massless jets whereas the `E` scheme forms massive jets, the jet four-momentum being simply the sum of the individual particle four momenta.

Scheme	Jet four-momentum calculation
`E`	$E_{ij} = E_i + E_j, \vec{p}_{ij} = \vec{p}_i + \vec{p}_j$
`P`	$E_{ij} = \lvert\vec{p}_{ij}\rvert, \vec{p}_{ij} = \vec{p}_i + \vec{p}_j$
`E0`	$E_{ij} = E_i + E_j, \vec{p}_{ij} = E_{ij}\left(\vec{p}_i + \vec{p}_j\right) / \lvert\vec{p}_i + \vec{p}_j\rvert$

Table 5.2: Different schemes of defining the jet four momentum in jet clustering algorithms.

Two other algorithms exist, `LUCLUS` [72] and `PTCLUS` [73], that include an additional step in the jet clustering process. In these algorithms once the initial jets have been formed particles may be assigned to a different jet by consideration of the particles transverse momentum with respect to the jet.

The choice of jet clustering algorithm was made after studies performed for previous analyses [62, 63]. Monte Carlo studies were made to compare the reconstructed invariant mass of a pair of jets with the true generated W mass using different jet clustering algorithms, considering both the size and resolution of the mass shift. It was found that the `DURHAM` algorithm gave the smallest shift and resolution when used in the "`PE`" scheme. In this scheme the objects are clustered into jets using the `P` scheme, assuming they are massless, as this is found to minimise misassignment of objects to jets. The four-momenta of the objects are then combined to form massive jets as in the `E` scheme.

After jet clustering the invariant mass of a reconstructed W boson candidate is just that of a pair of jets, hereafter referred to as the dijet mass.

5.1.2 Jet Energy Corrections

The whole of this W mass measurement depends on good agreement between data and Monte Carlo, in particular the W mass extraction, as explained in Chapter 6. It is important that this agreement is checked at different stages throughout the analysis. The reconstruction of the jets may be studied, in particular the jet energy. This is carried out using the calibration data taken at the Z^0 resonance, shown in Table 3.1. Events with two jets resulting from the fully hadronic decay of a Z^0 boson are selected in both the data and Monte Carlo. Since the Z^0 bosons are produced at rest the jets are produced with equal and opposite momenta. The energy carried by each jet should on average be equal to the LEP beam energy, E_{beam}, however, the measured jet energy will not in general be equal to the true jet energy due to the response of the detector. To check the simulation of the detector in Monte Carlo the ratio of the measured jet energy to the beam energy may be compared to the same ratio in data. The double ratio, R, is formed:

$$R = \frac{\left(E_{jet}/E_{beam}\right)_{data}}{\left(E_{jet}/E_{beam}\right)_{MC}} . \tag{5.3}$$

This ratio is shown in Figure 5.1 as a function of polar angle. If the Monte Carlo reproduces the data perfectly the ratio should be unity. Small differences between data and Monte Carlo are seen, particularly in the overlap region between the barrel and endcap calorimeters, rising to approximately 3% in the regions close to the beam pipe. To take these differences into account any Monte Carlo data used in the analysis has its jet energies corrected by this ratio, depending upon which bin of Figure 5.1 the jet polar angle falls.

5.2 Kinematic Fitting

Kinematic fitting is one of the most important steps in the W mass measurement. Since LEP is an electron positron collider then in principle both the centre of mass energy of the event and the total momentum are known. The total energy and momentum of the observed particles in the detector should be equal to these quantities, however, detector related effects such as the finite energy resolution

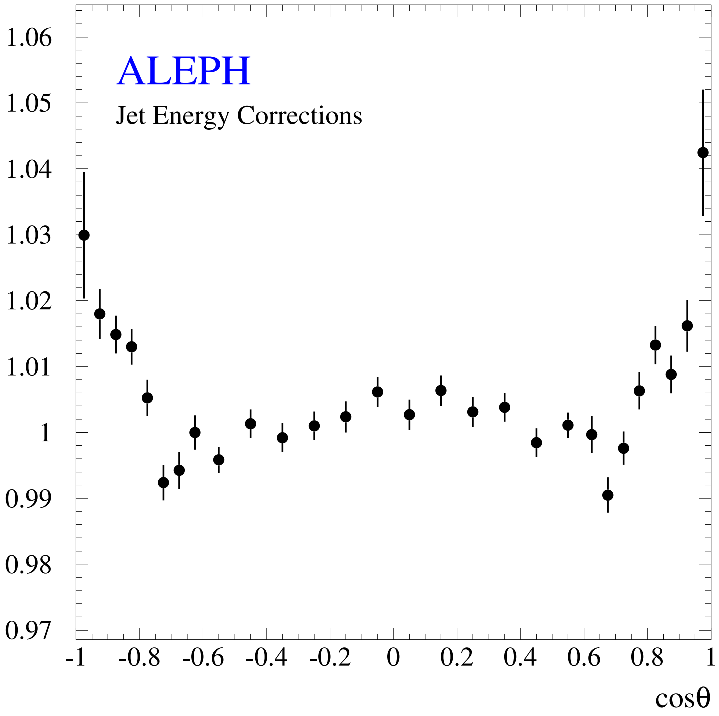

Figure 5.1: The ratio $\frac{\left(E_{jet}/E_{beam}\right)_{data}}{\left(E_{jet}/E_{beam}\right)_{MC}}$ derived from 1998 Z^0 data and Monte Carlo as a function of jet polar angle, taken from Reference [74].

of the detector and particle losses in the beam pipe mean that this will not be the case. The kinematic fit exploits the knowledge of the total energy and momentum in order to improve significantly the resolution of the jets and therefore the dijet invariant mass resolution.

5.2.1 Kinematic Fit Principles

Kinematic fitting works by varying the energy and momentum of the measured particles, in this analysis the four jets, until the constraints of energy and momentum are satisfied:

$$\begin{aligned} \sum_{i=1}^{4} E_i &= 2E_{beam} \\ \sum_{i=1}^{4} \vec{p}_i &= \vec{0}\,. \end{aligned}$$

The variation of the four vectors is carried out by minimising an appropriate χ^2 function derived from the measured and fitted four-momenta, whilst imposing the energy and momentum constraints in a suitable fashion. In addition to these constraints equal dijet masses may be imposed, since the W bosons are expected to be produced with approximately equal masses.

Two kinematic fitting packages have been studied, `ABCFIT` [75] and `KINFIT` [76], taking different approaches to the different steps involved in a kinematic fit; these are now explained in detail.

5.2.2 `ABCFIT`

`ABCFIT` [75] imposes the constraints through Lagrange multipliers, using an iterative process to minimise the quantity

$$S\left(\vec{y},\vec{\lambda}\right) = \left(\vec{y}-\vec{y_0}\right)^T \mathbf{V}^{-1}\left(\vec{y}-\vec{y_0}\right) + 2\vec{\lambda}.\vec{f}\left(\vec{y}\right)\,, \tag{5.4}$$

where $\vec{y}$ are the fitted correction factors, $\vec{y_0}$ the expected correction factors, $\vec{\lambda}$ the Lagrange multipliers, $\vec{f}\left(\vec{y}\right)$ the vector of constraint functions, and $\mathbf{V}$ is the covariance matrix.

The correction factors are three variables for each jet, a_j, b_j, c_j, that transform the measured momenta of the jets into the fitted momenta by scaling and introducing shifts in the θ and ϕ directions:

$$\vec{p}_j^{\,fit} = \exp\left(a_j\right) \vec{p}_j^{\,meas} + b_j \vec{u}_j^{\,\theta} + c_j \vec{u}_j^{\,\phi} \,, \tag{5.5}$$

where $\vec{u}_j^{\,\theta}$ and $\vec{u}_j^{\,\phi}$ are unitary vectors in the θ and ϕ directions perpendicular to the measured momentum. If the jets were measured perfectly then the correction factors would all be zero. The jet energy is scaled by the same factor as the momentum, in other words the jet velocity β is assumed to be constant:

$$\beta = \frac{\left|\vec{p}_j^{\,meas}\right|}{E_j^{meas}} = \frac{\left|\vec{p}_j^{\,fit}\right|}{E_j^{fit}} \,. \tag{5.6}$$

The correction factors a_j, b_j, and c_j and the covariance matrix $\mathbf{V}$ are determined from Monte Carlo data as described in Section 5.2.4. The correction factors are parametrised as functions of the measured jet energy and polar angle. They are assumed to follow Gaussian distributions and thus the value of S at the minimum is distributed like a χ^2 distribution. A χ^2 distribution is characterised by the number of degrees of freedom, defined as the number of measured quantities minus the number of independent fitted parameters. There are twelve fitted parameters, the three correction factors for each jet, and four constraints, giving eight independent fitted parameters. There are twelve measured quantities, the expected correction factors for each jet, and so the distribution of the minimum values of S should be described by a χ^2 function having four degrees of freedom.

To minimise S we require that the derivatives of S with respect to the correction factors and the Lagrange multipliers must both be zero:

$$\begin{array}{lcll} \frac{\partial S}{\partial \vec{y}} & = & 2\mathbf{V}^{-1}\left(\vec{y} - \vec{y}_0\right) + 2\vec{\lambda}\frac{\partial \vec{f}(\vec{y})}{\partial \vec{y}} & = 0 \\ \frac{\partial S}{\partial \vec{\lambda}} & = & 2\vec{f}\left(\vec{y}\right) & = 0 \end{array} \tag{5.7}$$

The derivatives are calculable analytically and so the minimisation is typically fast.

5.2.3 `KINFIT`

The `KINFIT` package [76] varies from `ABCFIT` in both minimisation technique and imposition of the constraints, which is performed implicitly through the description of the WW decay kinematics. There are 16 measured kinematic variables in a fully hadronic event, the four-vectors of the four jets. These may be reduced to a set of twelve independent variables under the assumption that the event is a fully hadronic WW decay. These parameters, shown in Figure 5.2, are:

- M_{W_1} and M_{W_2}, the masses of the two W bosons, or more properly the invariant masses of the two jets assigned to each W.
- θ and ϕ, the polar and azimuthal angles of W_1 in the laboratory frame. The direction of W_1 must be opposite to that of W_2.
- θ_1^* and ϕ_1^*, the angles describing the direction of jet 1 in the rest frame of W_1, with respect to the direction of W_1. The direction of jet 2 is opposite to that of jet 1 in this frame.
- θ_3^* and ϕ_3^*, the angles describing the flight direction of jet 3 in the rest frame of W_2, with respect to the direction of W_2. The direction of jet 4 is opposite to that of jet 3.
- M_1, M_2, M_3 and M_4, the masses of the four jets in the final state.

These twelve variables define a space in which an appropriate χ^2 function is minimised. Once the minimisation is complete the variables are transformed back to give the four vectors of the fitted jets. Since two of the variables in the minimisation space are the dijet masses then the errors on the fitted masses are easily available after minimisation.

The χ^2 function is constructed using four parameters to describe each jet. These are:

- $\Delta\beta = \Delta\left(p/E\right)$, the velocity difference between the measured and fitted jets.
- ΔE, the energy difference between the measured and fitted jets.

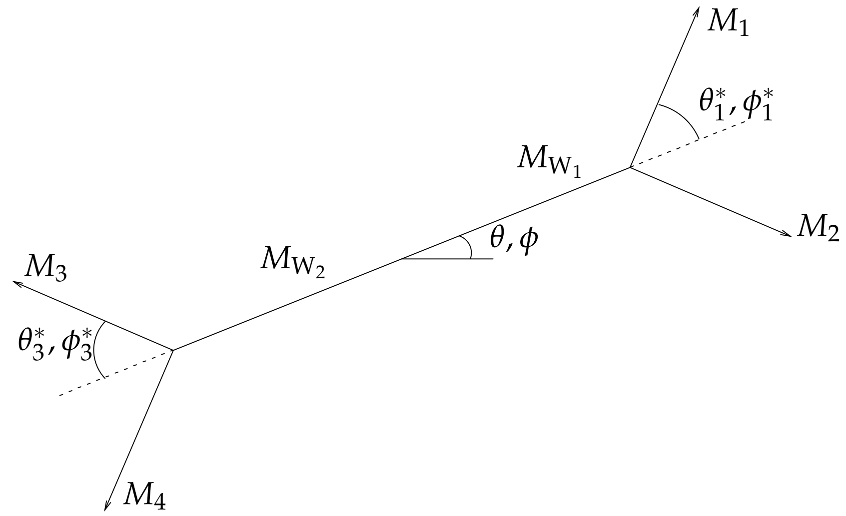

Figure 5.2: Variables describing W pair decay.

- Two components of the transverse momentum of the measured jet with respect to the fitted jet, perpendicular to each other, as shown in Figure 5.3.
  - p_T^θ, the component lying in the plane containing the beam axis and the fitted jet.
  - p_T^ϕ, orthogonal to the plane containing the beam axis and the fitted jet.

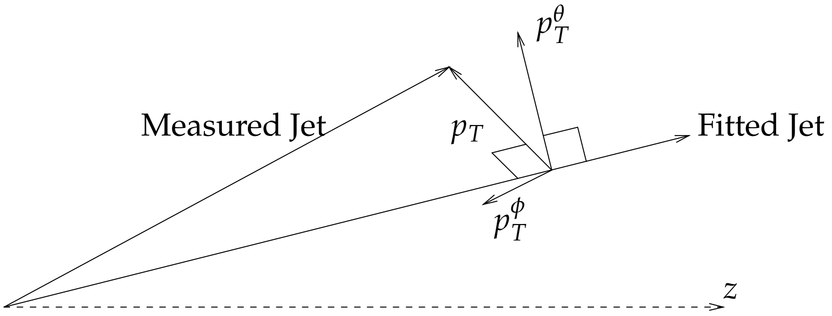

Figure 5.3: The parameters p_T^θ and p_T^ϕ.

As with the a_j, b_j and c_j parameters for `ABCFIT` the average values and resolutions of these parameters are determined from Monte Carlo simulation. The χ^2 function has a contribution from each jet:

$$\chi^2 = \sum_{j=1}^{4} \chi_j^2 \,, \tag{5.8}$$

this being constructed as:

$$\chi_j^2 = \begin{pmatrix} \Delta E' \\ \Delta \beta' \\ \Delta p_T^{\theta\prime} \\ \Delta p_T^{\phi\prime} \end{pmatrix}^T \mathbf{V}^{-1} \begin{pmatrix} \Delta E' \\ \Delta \beta' \\ \Delta p_T^{\theta\prime} \\ \Delta p_T^{\phi\prime} \end{pmatrix} . \tag{5.9}$$

Where **V** is the correlation matrix and the primed quantities are defined as

$$\Delta E' = \frac{\Delta E^{meas} - \Delta E^{fit}}{\sigma_{\Delta E^{fit}}} . \tag{5.10}$$

The χ^2 function is again characterised by four degrees of freedom since there are sixteen measured parameters, four for each jet, and twelve independent fitted parameters. The minimisation is performed using the `MINUIT` package [77], and is much more CPU intensive than `ABCFIT`. The major differences between the two kinematic fitting packages are:

- Choice of correction factors.
- Minimisation technique.
- `KINFIT` allows the β of the jets to vary while `ABCFIT` keeps it constant.
- CPU time.

5.2.4 Parametrisation of Corrections

Both kinematic fitting packages depend on correction factors that are applied to the jets. These corrections depend on the energy of the jet and its direction. The average values and resolutions are determined using WW Monte Carlo data making use of the true jet properties before detector simulation and the measured properties after detector simulation.

A large sample of fully hadronic WW events is taken from Monte Carlo simulated data. The `DURHAM PE` algorithm is used to cluster both the reconstructed energy flow objects and the true particles before detector simulation into four jets. An association is then carried out between the jets at each level of reconstruction. The jets are divided into different bins depending on their energy and polar angle. The appropriate correction factor is calculated for every jet, e.g. $\Delta\beta = \beta_{meas} - \beta_{true}$ for `KINFIT` or $a_j = \ln\left(\left|\vec{p}_j^{true}\right| / \left|\vec{p}_j^{meas}\right|\right)$ for `ABCFIT`. Distributions of each correction factor are made for each bin, and a Gaussian function fitted to each distribution. The distributions for the `ABCFIT` parameters in one bin are shown in Figure 5.4 along with the fitted Gaussian distributions. It can be seen that the fits are not perfect mainly due to effects such as the different resolutions of the particles in the jet such as neutral hadrons and charged particles. The resulting mean values and resolutions of the fitted Gaussian distributions together with the errors on these values are used to construct two dimensional histograms in energy and cosine of the polar angle. Finally two dimensional polynomial functions are fitted to the histograms to obtain descriptions of the energy and polar angle dependence of the correction factors. The measured and fitted values of the a_j parameter are shown in Figure 5.5. The correlations between the correction factors may be obtained in the same way, or alternatively an average value of the correlation over the whole energy and angular range may be taken.

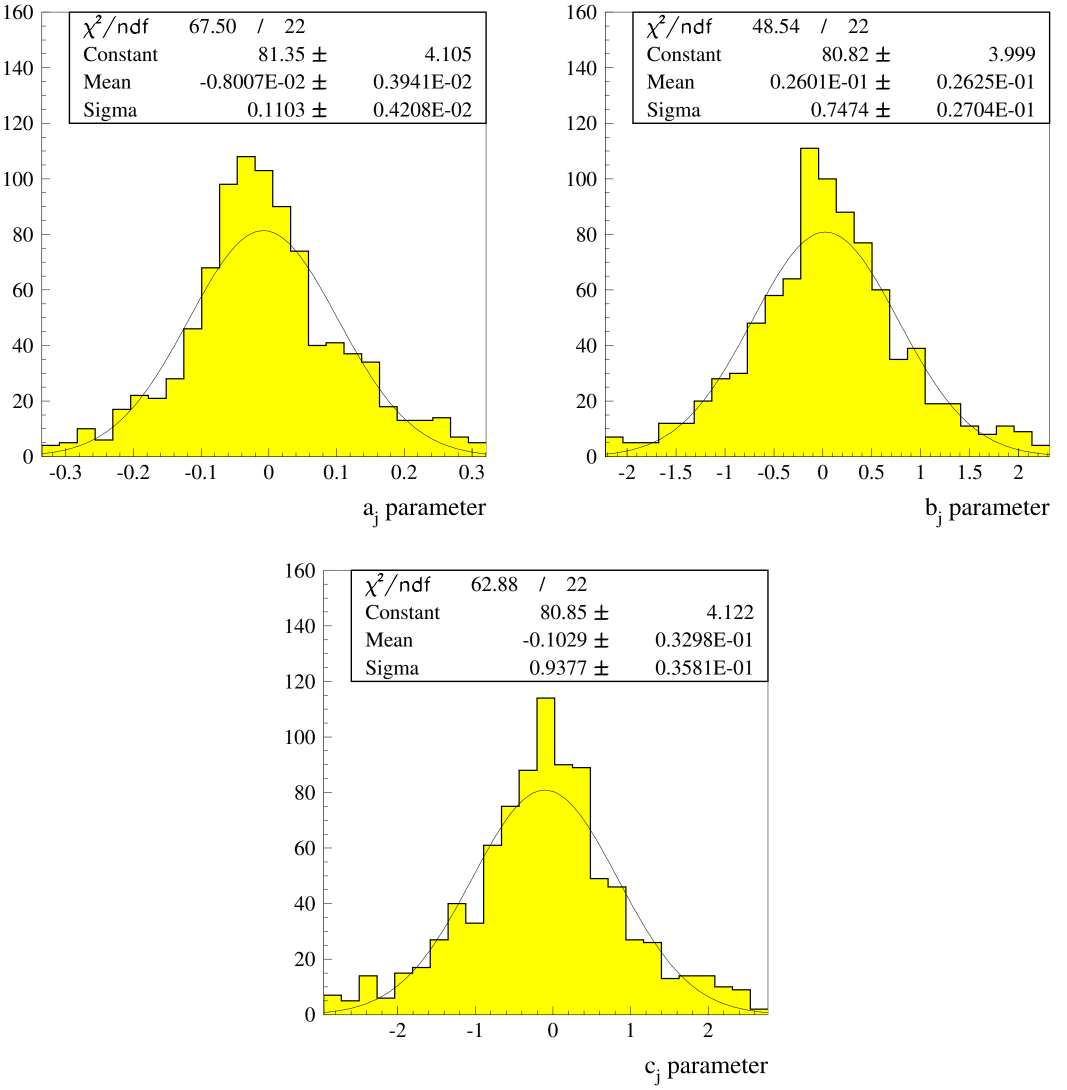

Figure 5.4: Distributions of the `ABCFIT` parameters a_j, b_j and c_j for jets in the range 45 GeV $< E <$ 51 GeV, $0.0 < \cos\theta < 0.1$, together with fitted Gaussian distributions. The χ^2 of the fit is shown together with the mean and resolution.

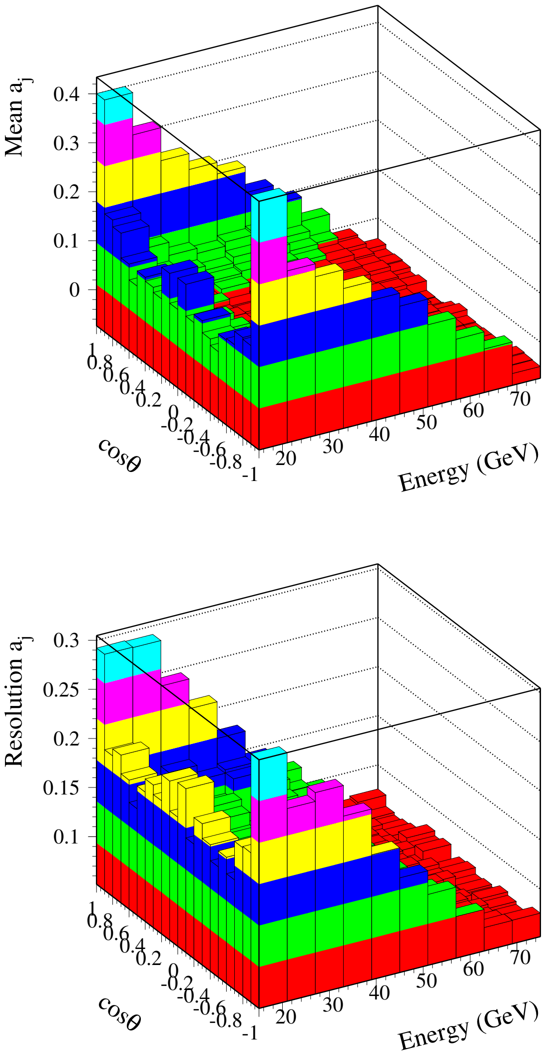

Figure 5.5: Distributions of the measured and fitted mean and resolution of the `ABCFIT` correction factor a_j.

5.2.5 Performance

The performance of the different kinematic fits may be evaluated using Monte Carlo events, ensuring that a different sample than that used to parametrise the correction factors is used. Firstly the difference between the dijet invariant mass obtained after kinematic fitting and the true generated W mass may be examined. Naïvely it may be expected that this distribution would have a mean of zero, indicating that the kinematic fit has introduced no bias into the mass reconstruction, however this is not the case. Instead a small positive bias is expected due to the presence of initial state radiation (ISR), as explained in detail in Section 5.3. Figure 5.6 shows the difference between the fitted dijet mass and the true W mass for both kinematic fit packages, along with the corresponding distributions for events with an ISR energy less than 0.5 GeV, for which a smaller bias is seen. It can be seen that the mean and resolution is slightly smaller for `ABCFIT` than `KINFIT`.

The χ^2 distribution, or more usefully, the χ^2 probability distribution of the kinematic fits may be plotted. If the values of χ^2 obtained after minimisation are truly drawn from a χ^2 distribution then the probability distribution will be flat. As Figure 5.7 shows this is largely the case over a wide range of probability, apart from very small probability values where there is a large peak. This peak indicates that approximately 10% of events do not fit well the kinematic fit hypothesis of energy and momentum conservation, largely due to mis-measurement of the event in some way, for example particle losses down the beam-pipe, or initial state radiation. The fact that the Gaussian description of the correction factors is not ideal also leads to an underestimation of the resolution on the correction factors for those events in the tails of the distributions in Figure 5.4, thereby leading to a large χ^2 value and thus a very small χ^2 probability. Figure 5.8 shows that the size of the peak in the χ^2 probability in data is well reproduced by the Monte Carlo simulation. Figure 5.7 also shows that the χ^2 probability distribution of `KINFIT` rises slightly for large values of probability. This indicates that the resolution on the correction factors are overestimated for some events, corresponding to those events in the core of the distributions in Figure 5.4. This leads to a smaller than expected χ^2 value.

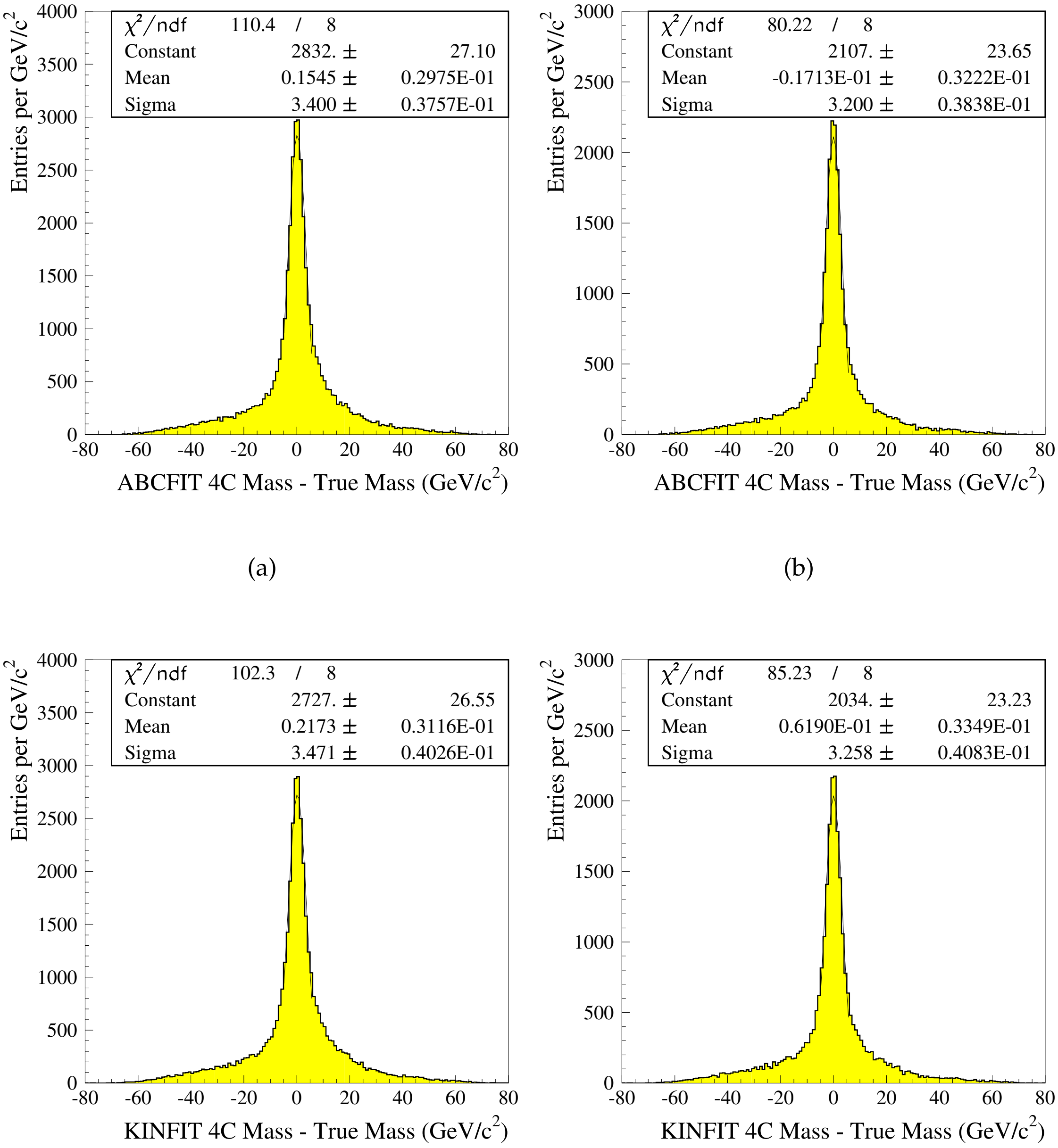

(a) (b)

(c) (d)

Figure 5.6: The difference between the dijet mass after kinematic fitting and the true W mass. Figures (a) and (b) show the results after `ABCFIT`, Figures (c) and (d) the results of `KINFIT`. Figures (a) and (c) are obtained using all WW Monte Carlo events selected as hadronic candidates. The positive bias due to initial state radiation is shown by the results of the fit to the peak position. Figures (b) and (d) are obtained using just those events with an ISR energy of less than 0.5 GeV. The bias in the mass is much smaller.

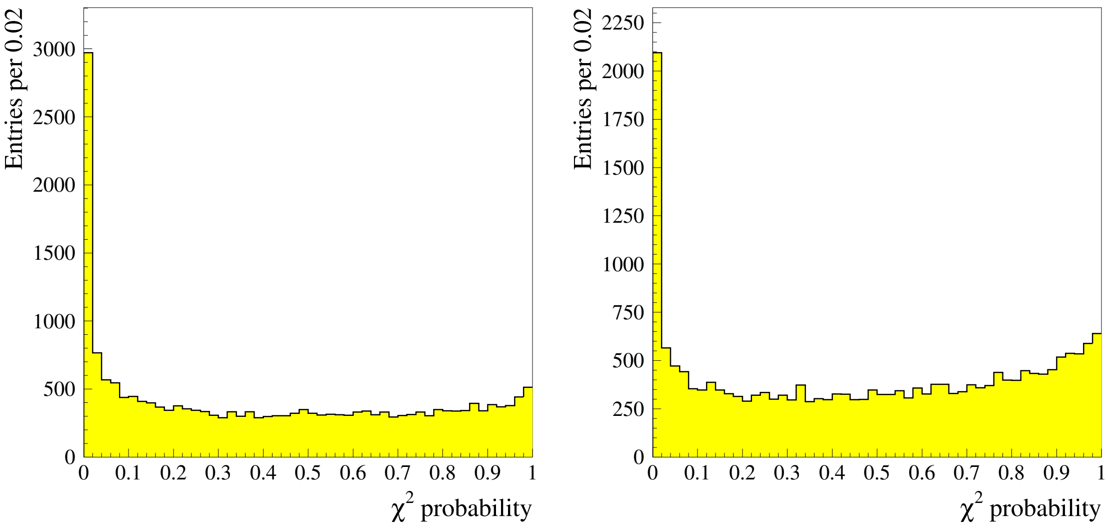

(a) (b)

Figure 5.7: The χ^2 probability distribution for (a) `ABCFIT` and (b) `KINFIT` for WW Monte Carlo events. These plots show a largely flat distribution, indicating that most events fit the kinematic fit hypothesis well. Roughly 10% of events fail the kinematic fit hypothesis in some way leading to large χ^2 values and thus a peak at small values of χ^2 probability.

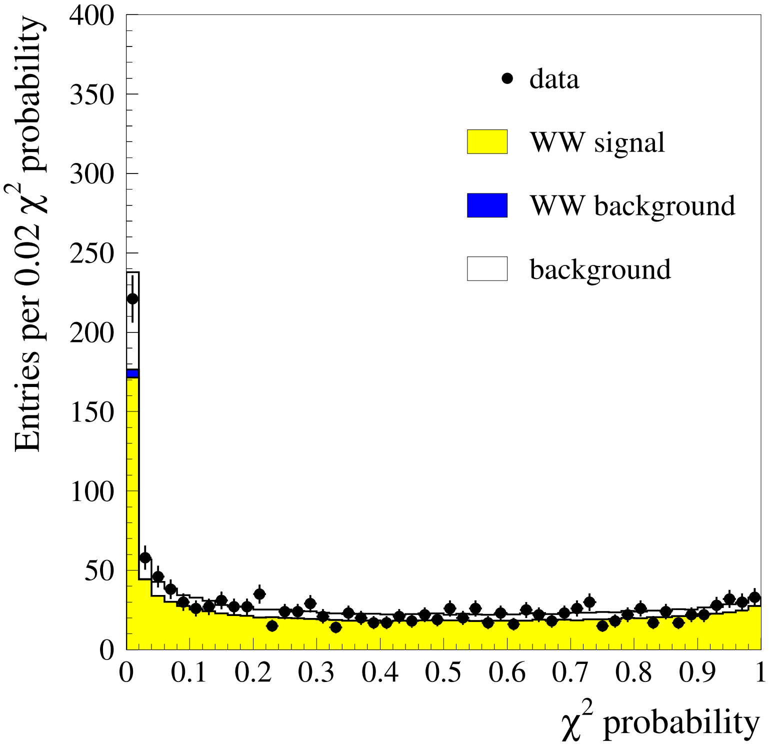

Figure 5.8: A comparison of the data and Monte Carlo distributions of the `ABCFIT` χ^2 probability.

Finally the errors on the fitted dijet invariant mass may be studied using the pull distribution. The pull is defined as

$$\frac{M_{\mathrm{W}_{meas}} - M_{\mathrm{W}_{true}}}{\sigma_{M_{\mathrm{W}_{meas}}}} . \tag{5.11}$$

If the error on the dijet mass is well reconstructed by the kinematic fit then the pulls should be distributed as a Gaussian with a mean of zero and a unit width. Figure 5.9 shows that this is not in fact the case for either kinematic fitting package. The width is larger than expected, and the distributions have tails to large values. This indicates that for at least some events the errors on the dijet masses are underestimated. There are many different contributing factors to why this is the case, including the inadequate parametrisation of the correction factors and the misassignment of particles to jets. In four jet events particles can be wrongly clustered into a jet with particles coming from the other W boson. The error due to this effect is not taken into account in the kinematic fitting and would be difficult to include, involving calculating correlations between the correction factors from different jets. The fact that the errors are poorly described means that it would be hard to justify their use in the W mass measurement.

5.2.6 Choice of Kinematic Fit

The choice of which kinematic fitting package to use was based upon their performance, as described in the previous section, in particular the dijet mass resolution and the χ^2 probability distribution. As shown in Figure 5.6 the mass resolutions are similar, with `ABCFIT` having the slightly better resolution. `ABCFIT` also has a smaller bias when considering those events containing ISR of less then 0.5 GeV. The χ^2 probability distribution of `ABCFIT` is flatter than `KINFIT`, however there are more events in the peak at low χ^2 probability. The performances of both packages are relatively similar, and so it was decided to use `ABCFIT` fit largely for reasons of computation time. `ABCFIT` runs approximately 25 times faster than `KINFIT`, providing a considerable time saving when considering the large number of Monte Carlo events that are used in the analysis. `ABCFIT` is also based directly on the kinematic fitting package used in previous analyses [62, 63]. Figure 5.8 shows the comparison of the `ABCFIT` χ^2 probability distribution function for the $\sqrt{s} = 188.6$ GeV data and Monte Carlo; good agreement is seen.

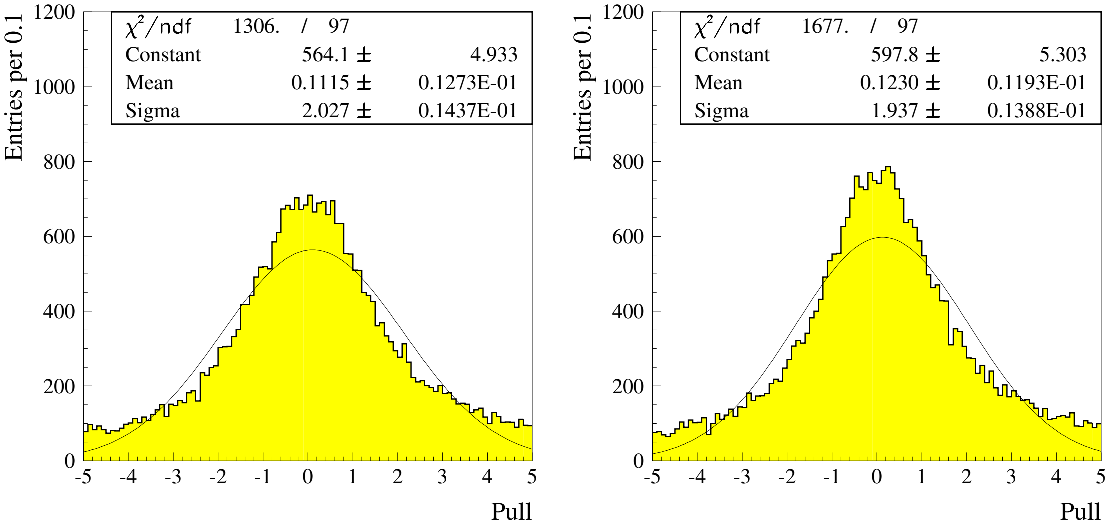

(a) (b)

Figure 5.9: The pull distributions for (a) `ABCFIT` and (b) `KINFIT`. This distribution should be a Gaussian of unit width with a mean of zero. It is clear that this is not the case, indicating that the errors on the fitted dijet masses are not properly understood.

5.2.7 Rescaling

The dijet mass resolution after kinematic fitting can be further improved by rescaling with the LEP beam energy:

$$M_{ij}^{resc} = M_{ij} \times \frac{E_{beam}}{E_i + E_j}, \tag{5.12}$$

where M_{ij} is the invariant mass of jets i and j. The improvement in the invariant mass resolution after kinematic fitting and rescaling is shown in Figure 5.10. The rescaled masses are not in themselves better estimators of the dijet masses, but when combined add more information through their dependence on the W velocities. This is explained in more detail in Appendix B.

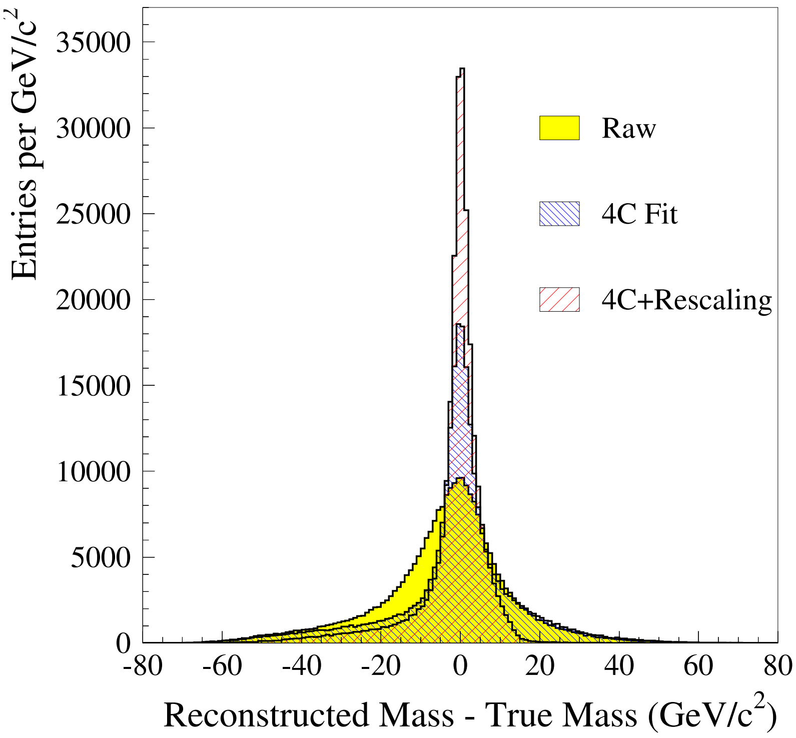

Figure 5.10: The reconstructed dijet mass resolution for measured jets, after a 4C kinematic fit and after rescaling with the beam energy.

5.3 Initial State Radiation

The fundamental idea upon which kinematic fitting is based is that we have knowledge of the centre of mass energy of the event, assumed to be twice the beam energy of LEP, and that the total momentum is zero. However this assumption is wrong in a large fraction of cases due to initial state radiation (ISR), when one or more photons are emitted by the incoming electron and positron. This leads to a reduction in the centre of mass energy in the collision, and also the total momentum will not be zero. In many events the energy lost through ISR will be very small, and so will be indistinguishable from the finite energy resolution of the detector to the kinematic fit. As a result of higher energy ISR the dijet invariant mass peak after kinematic fitting will have a positive bias, since the assumed energy is larger than the true centre of mass energy. As long as the Monte Carlo accurately models the data then this positive bias should have no effect on the fitted W mass due to the mass extraction technique used in this thesis, Monte Carlo reweighting, described in Chapter 6. However, the presence of the ISR also tends to worsen the invariant mass resolution. It may be hoped that an improved treatment of ISR will lead to an improved invariant mass resolution and an improved statistical error on the final fitted W mass. The presence of ISR also leads to a degradation in the performance of the kinematic fit. As shown in Figure 5.8 the χ^2 probability distribution is not flat, there is a peak at very low values of χ^2 probability. This peak corresponds to events that do not fit the kinematic fit hypothesis, and thus have very large χ^2 values. ISR with energies greater than 0.5 GeV is present in over 50% of the events in the peak, and the higher the energy of the ISR emitted the more likely the event is to fail the kinematic fit, as shown in Figure 5.11.

5.3.1 Undetected ISR - Inclusion in the Kinematic Fit

Most ISR is emitted along the LEP beam pipe, since it is produced collinear with the electron or positron. The ALEPH detector therefore has no chance of observing these photons. The hypothesis that collinear ISR has been emitted may, however, be included in the kinematic fit, under the assumption of one photon, as

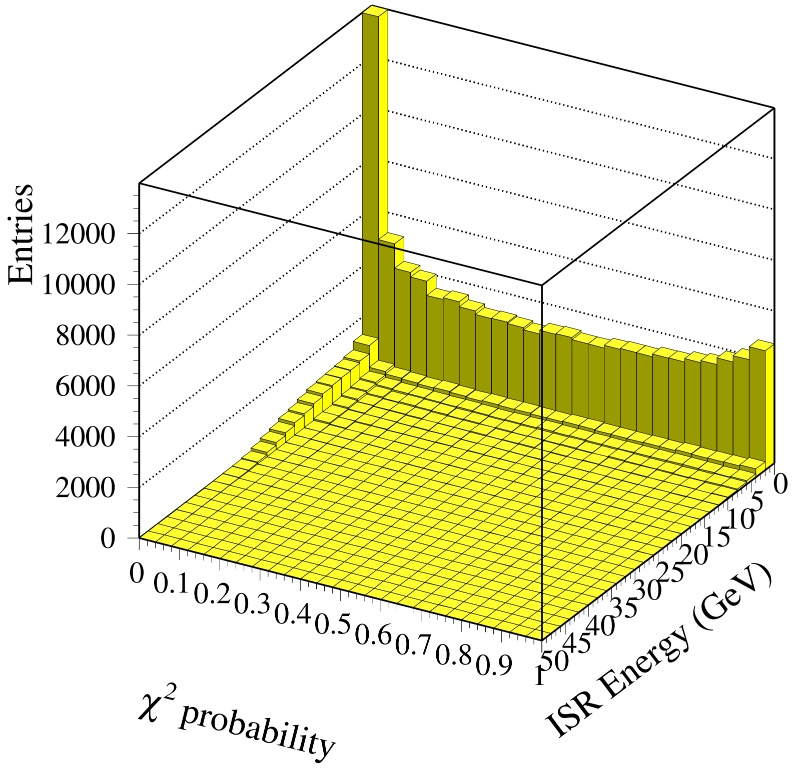

Figure 5.11: The `ABCFIT` kinematic fit χ^2 probability as a function of the energy lost through initial state radiation. Events where a large amount of energy has been lost are more likely to fail the kinematic fit.

described in [78]. There are two stages to this; the first is to change the constraints to take into account the ISR:

$$\left(\sqrt{s}, \vec{0}\right) \rightarrow \left(\sqrt{s} - E_\gamma, 0, 0, -p_\gamma\right) \ , \tag{5.13}$$

where $\left(E_\gamma, 0, 0, p_\gamma\right)$ is the four vector of the emitted photon. The second stage is a modification of the χ^2 of the fit by the addition of an extra term describing the ISR photon. This could be done by introducing the likelihood concept and adding a term such as

$$g\left(p_\gamma\right) = -2\ln\left(F\left(p_\gamma\right)\right) \ , \tag{5.14}$$

where $F\left(p_\gamma\right)$ is the probability distribution of the ISR as a function of the photon energy. To lowest order the ISR spectrum is given by [2]:

$$p\left(x\right)dx = \beta_{\mathrm{e}} x^{\beta_{\mathrm{e}}-1} dx \, , \tag{5.15}$$

where $x = p_\gamma/\sqrt{s}$ and $\beta_{\mathrm{e}} = \frac{2\alpha}{\pi}\left(\ln\left(s/m_{\mathrm{e}}^2\right) - 1\right)$ and has a value of 0.114 at $\sqrt{s} =$ 188.6 GeV. The probability distribution is shown in Figure 5.12. As can be seen this distribution has a pole when $x = 0$ and so the kinematic fit would always take as the preferred value $p_\gamma = 0$. One solution to this problem is to use a cut-off in the ISR energy, excluding photons below a certain energy. However the choice

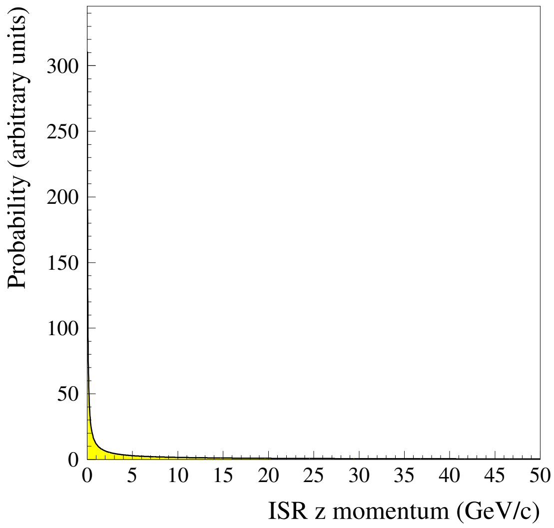

Figure 5.12: The ISR probability distribution as a function of ISR z momentum.

of this cut-off is not necessarily straightforward. Another possible solution is to use the confidence level

$$C(x) = \int_{x}^{\infty} p(y)dy = 1 - x^{\beta_e} . \tag{5.16}$$

The function to be minimised is then not anymore a χ^2 but is constructed as:

$$G(x) = -2\ln\left(\mathcal{P}_{4C}(x)\right) - 2\ln\left(C(x)\right) , \tag{5.17}$$

in order to properly normalise the two different contributions, where $\mathcal{P}_{4C}(x)$ is the kinematic fit χ^2 probability. Two fits are performed to take into account the ambiguity in the ISR probability distribution between the two possible photon directions.

For simplicity and to avoid modification of the `ABCFIT` program code the following procedure was used. A small additional piece of code was written which makes use of the `CERNLIB` routine `RMINFC` [79]. This minimises a function of one variable in a given range, here Equation 5.17 is minimised as a function of the ISR z momentum. `ABCFIT` is called with the appropriate constraints, according to the photon z momentum, and then the correct term to be added to take into account the ISR is calculated. Figure 5.13 shows the outcome of some different fits using Monte Carlo events.

Figure 5.14 shows the outcome of many different fits, where the fitted ISR z momentum is plotted against the true z momentum obtained from Monte Carlo information. In many cases the fit is successful and manages to fit correctly the true ISR in the event. However there are also a large number of cases in which the fit falsely creates ISR when there is actually none present. An example of such a fit is shown in Figure 5.13, where it is clear that the fit recreates the missing z momentum in the event and not the true ISR z momentum. It is also clear that there are some events in which the fitted z momentum is zero but there is ISR present in the event. Figure 5.15 shows the dijet invariant mass resolution before and after performing the fit for ISR, and also the rescaled mass after the jet pairing algorithm, described in Section 5.4, is applied. The effect of including beam ISR is to give a negative bias to the reconstructed mass, due to the inclusion of the "false" ISR. The resolution is only slightly improved.

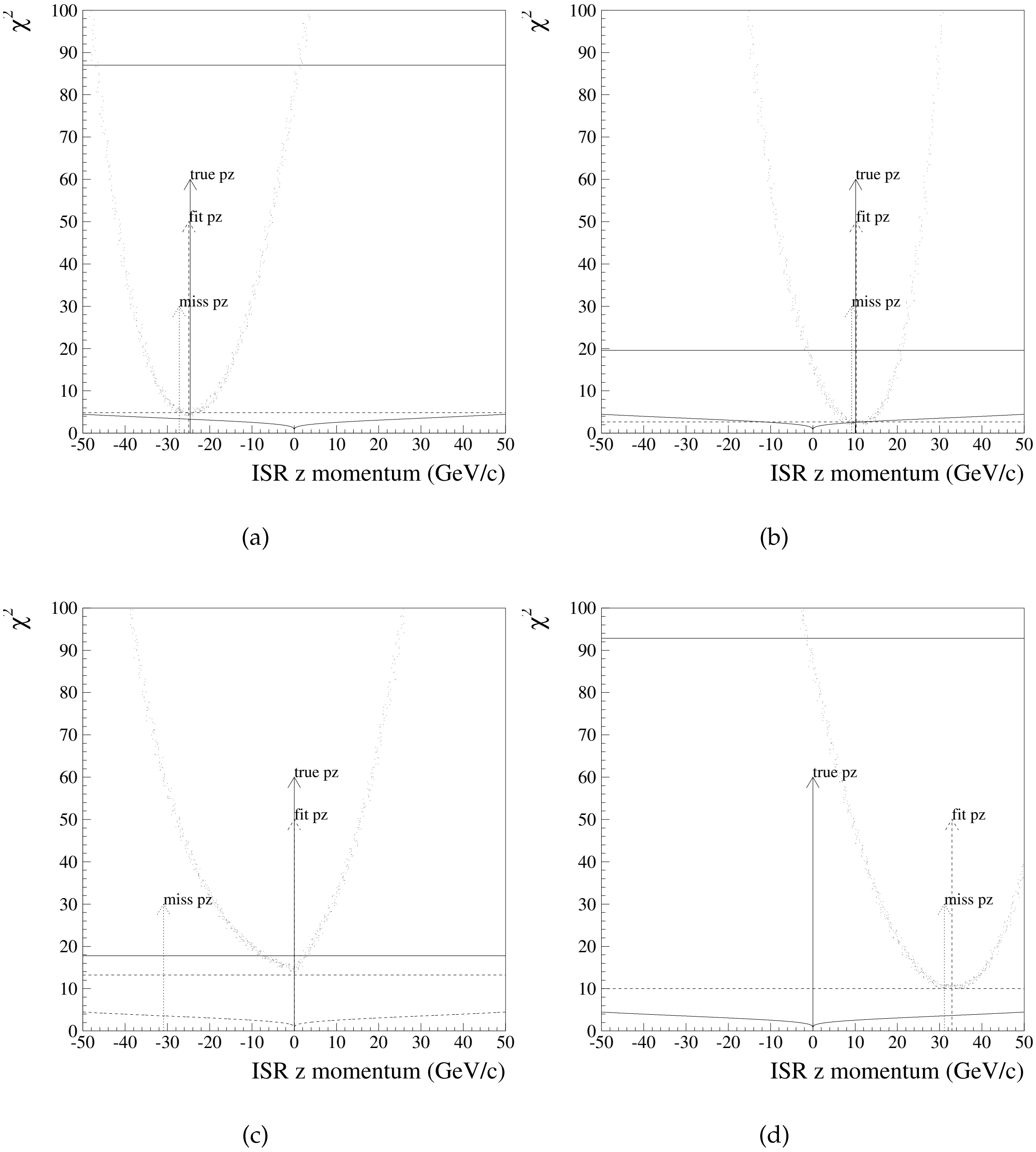

(a)

(b)

(c)

(d)

Figure 5.13: Examples of including the ISR hypothesis in the kinematic fit for four different events. The plot shows the values of the likelihood type function which is minimised. The arrows show the true ISR z momentum, the fitted ISR z momentum and the overall missing z momentum in the event. Figures (a), (b) and (c) show good fits where the fitted z momentum is a reasonable representation of the true z momentum. Figure (d) shows an example of an event in which the fitted momentum is the missing z momentum rather than the true ISR z momentum.

The expected statistical uncertainty for the whole mass analysis was evaluated using the $\sqrt{s} = 188.6$ GeV Monte Carlo as described in Section 6.3.1. With no fit for ISR the average uncertainty for 200 sub-samples of the same luminosity as the data was 99.5 ± 0.2 MeV/c^2. After including the hypothesis of beam ISR for just those events with a bad 4C kinematic fit χ^2 probability (< 0.01) the average uncertainty was 103.4 ± 0.3 MeV/c^2. Thus including the hypothesis of ISR worsens the statistical precision of the W mass measurement and so is not used.

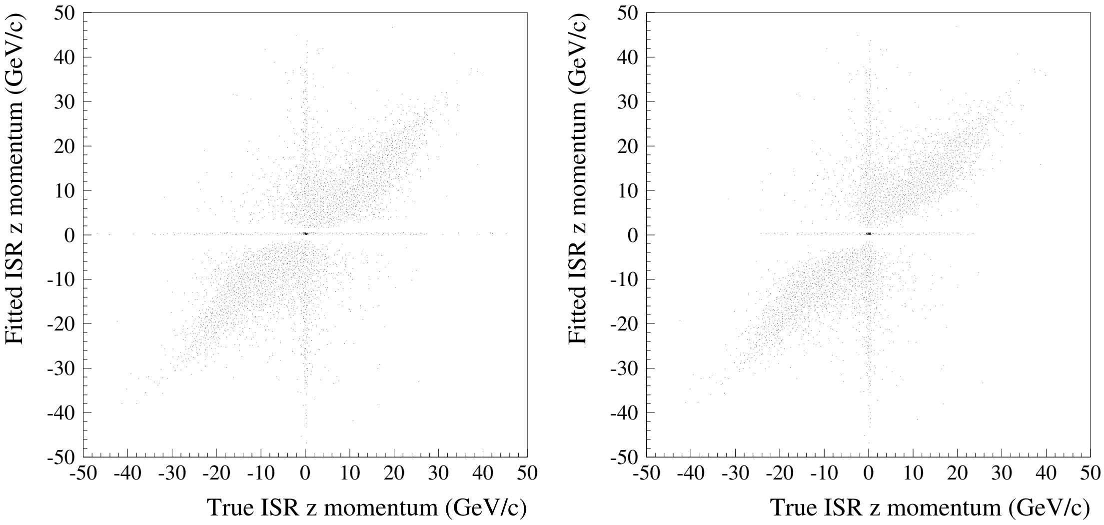

Figure 5.14: The fitted ISR z momentum plotted against the true ISR z momentum, obtained using WW Monte Carlo events. The left hand plot is for all selected events, the right hand plot just those with a bad 4C kinematic fit χ^2 probability.

5.3.2 Detected ISR

A significant number of selected hadronic events have an ISR photon that is not along the z direction but is inside the ALEPH detector acceptance, down to an angle of 1.4° from the beam in SiCAL. Table 5.3 shows the fraction of events with ISR in the detector obtained from Monte Carlo studies of WW events. Figure 5.16 shows the polar angle distribution of ISR photons that are within the detector acceptance. As expected from the ISR probability distribution this is strongly peaked at $|\cos\theta| \sim 1$, but shows that photons are produced throughout the whole angular range. These photons are included in the jets when they are clustered and

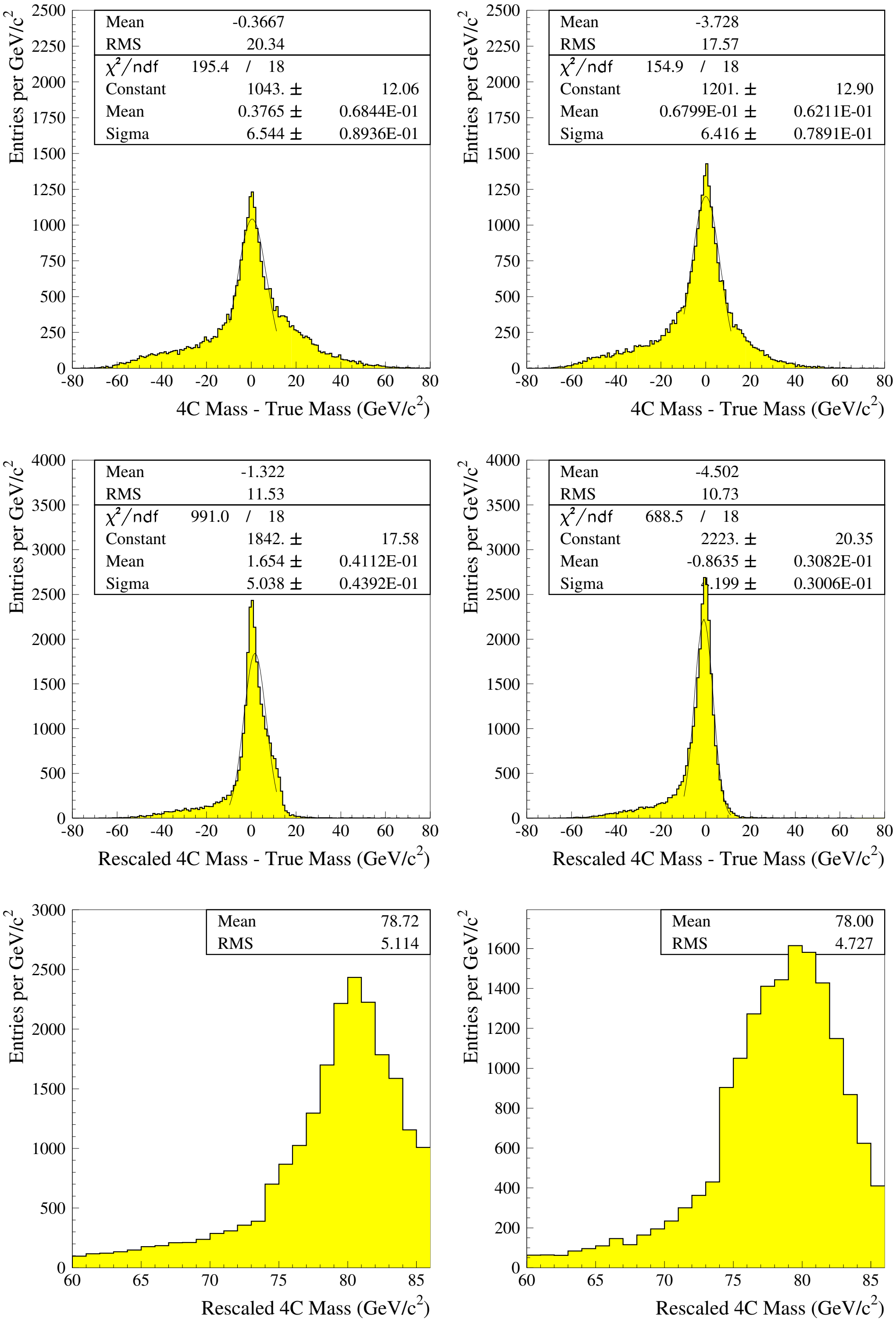

Figure 5.15: The mass resolution before (left hand plots) and after (right hand plots) accounting for collinear ISR in the kinematic fit for selected WW Monte Carlo events with $\mathcal{P}\left(\chi^2\right) < 0.01$. The top plots are the result of a 4C kinematic fit, the middle plots after rescaling, and the bottom plots the result of applying the jet pairing and mass window algorithm.

will therefore introduce a bias into the reconstructed dijet mass, and also worsen the mass resolution.

Photon Energy (GeV)	Total Number of ISR Photons	Fraction of Selected Events (%)	Number of ISR Photons in Detector	Fraction of Selected Events (%)
> 3 GeV	3024	17	1110	6
> 5 GeV	2144	12	777	4

Table 5.3: The number of ISR photons in the detector determined from Monte Carlo studies of WW events.

An algorithm was developed to select ISR photons within the detector acceptance, based upon their energy and angular isolation from other objects. Photons produced as part of the hadronisation process are expected to be close to other objects in the detector, and generally of low energy. ISR photons are not influenced by hadronisation and so more are produced with a greater separation from other objects. The high energy ISR photons are those that introduce larger biases in the reconstructed mass so it is more important to be able to select these. The variable used to describe the isolation of the photon is simply an angle α that is defined as the angle between the photon and the closest energy flow object to it. The energy spectrum and isolation angle of all photons and ISR photons only are shown in Figure 5.17. The criteria chosen to select ISR photons depend on the location of the photon in the detector, so if the candidate photon falls either in SiCAL or LCAL it is required to have an energy greater than 3 GeV and an isolation of $\cos\alpha < 0.99$, corresponding to an angle of approximately 8°. In the ECAL ISR photons are harder to identify due to the much larger number of hadronisation photons and so a minimum energy of 5 GeV is required with an isolation of $\cos\alpha < 0.95$, corresponding to approximately 18°. The performance of this selection is shown in Table 5.4.

Once a photon is selected as an ISR candidate then it is removed from the reconstruction process, so that the four jets are clustered without it. The constraints used in the kinematic fit must be modified as:

$$(E, \vec{p}) = \left(\sqrt{s} - E_\gamma, -\vec{p}_\gamma\right) \ . \tag{5.18}$$

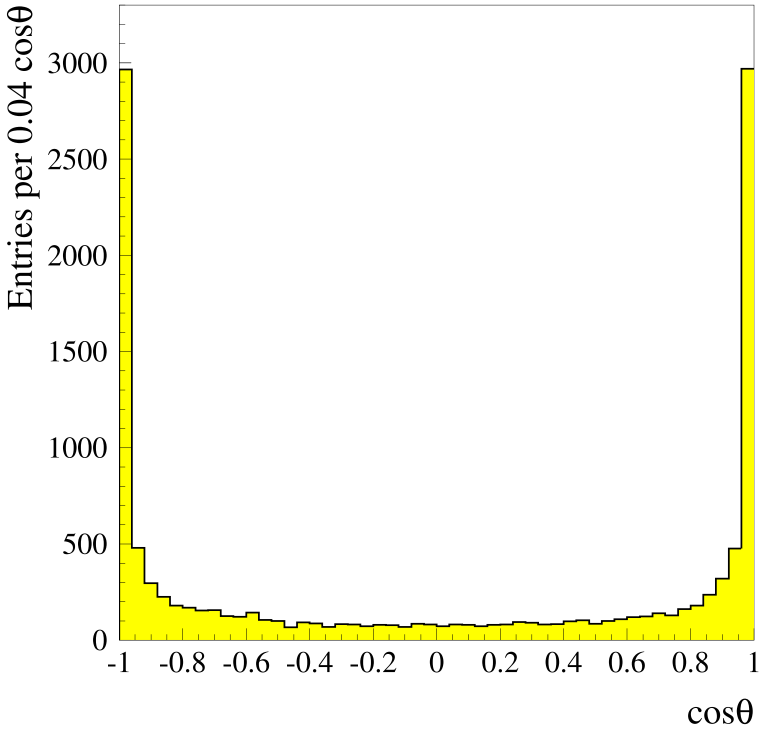

Figure 5.16: The angular distribution of ISR photons produced within the ALEPH angular acceptance in WW Monte Carlo events selected as fully hadronic candidates.

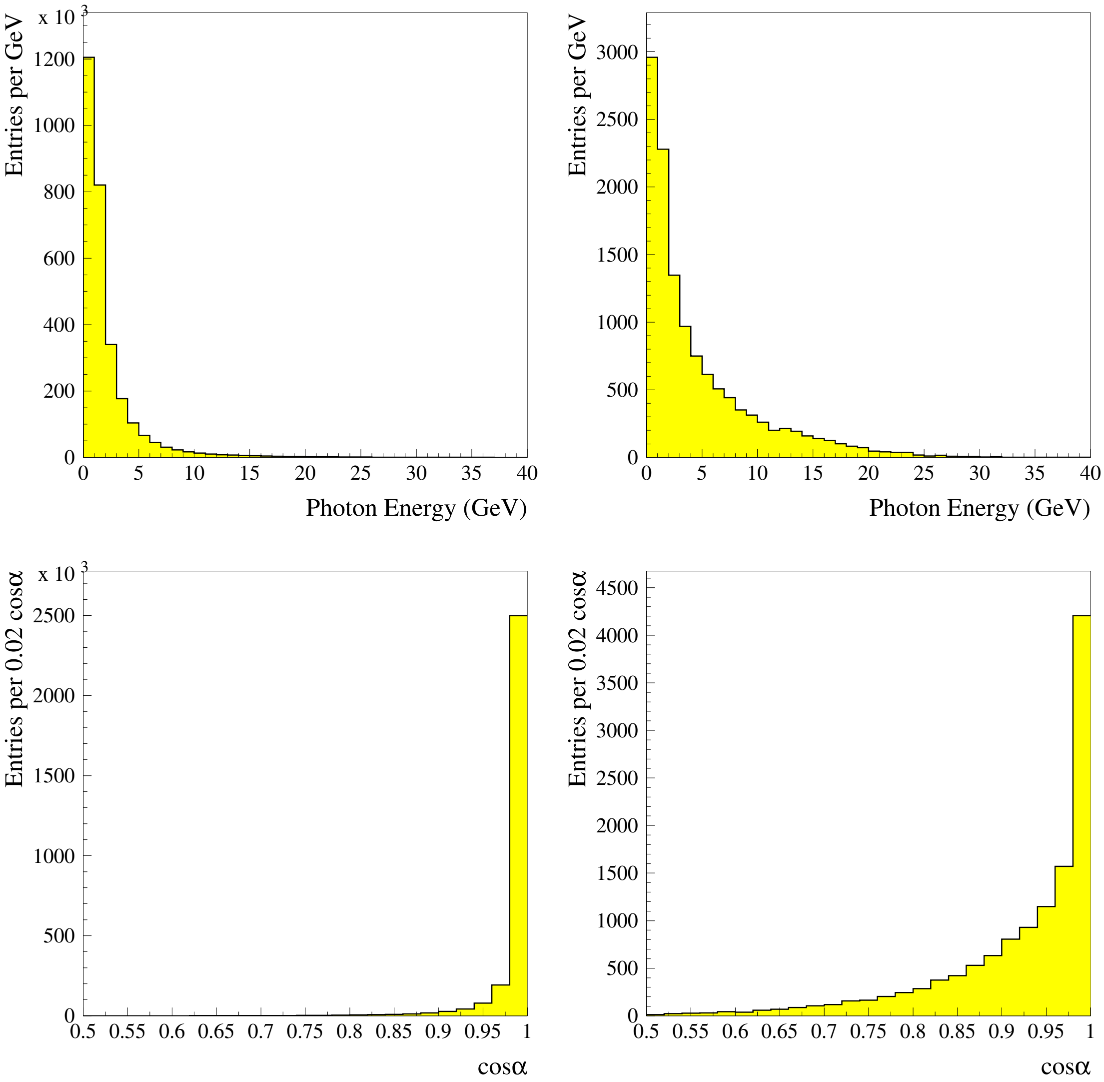

Figure 5.17: The energy and isolation angle distributions of all photons (left) and ISR photons (right) in WW Monte Carlo events selected as fully hadronic candidates. It can be seen that a greater proportion of ISR photons have a high energy and larger isolation angle than for hadronisation photons. The difference in the scales of the y-axes should be noted

Detector	Selection	Total Number of Photons Selected	Matched to ISR	Efficiency (%)	Purity (%)
SICAL	$E > 3$ GeV	234	122	100	52
	+ $\cos\alpha < 0.99$	117	99	81	85
LCAL	$E > 3$ GeV	1067	170	100	16
	+ $\cos\alpha < 0.99$	239	143	84	60
ECAL	$E > 5$ GeV	33784	326	100	1
	+ $\cos\alpha < 0.95$	188	148	45	79
ALL		544	390	63	72

Table 5.4: Efficiencies and purities for ISR photon selection, determined using WW Monte Carlo events selected as fully hadronic candidates. Here the efficiency is defined as the fraction of all ISR photons which are selected and the purity is the fraction of photons selected which are true ISR photons.

The rescaling is performed in the rest frame of the four jets using the correct beam energy.

Figure 5.18 shows a clear improvement in the reconstructed mass resolution after selecting and removing ISR candidates, both in terms of resolution and bias. After carrying out the mass extraction process the average statistical uncertainty on the W mass is reduced from 99.5 ± 0.2 MeV$/c^2$ to 98.2 ± 0.2 MeV$/c^2$, thus although the improvement is small it was decided to use this ISR selection in the reconstruction step of the analysis. Figure 5.19 shows comparisons of the data and Monte Carlo expectations for the photon energy, angular separation, α, and angular distribution. Reasonable agreement is observed. In the 188.6 GeV data 70 ISR candidates are observed, whereas 66 are expected from Monte Carlo.

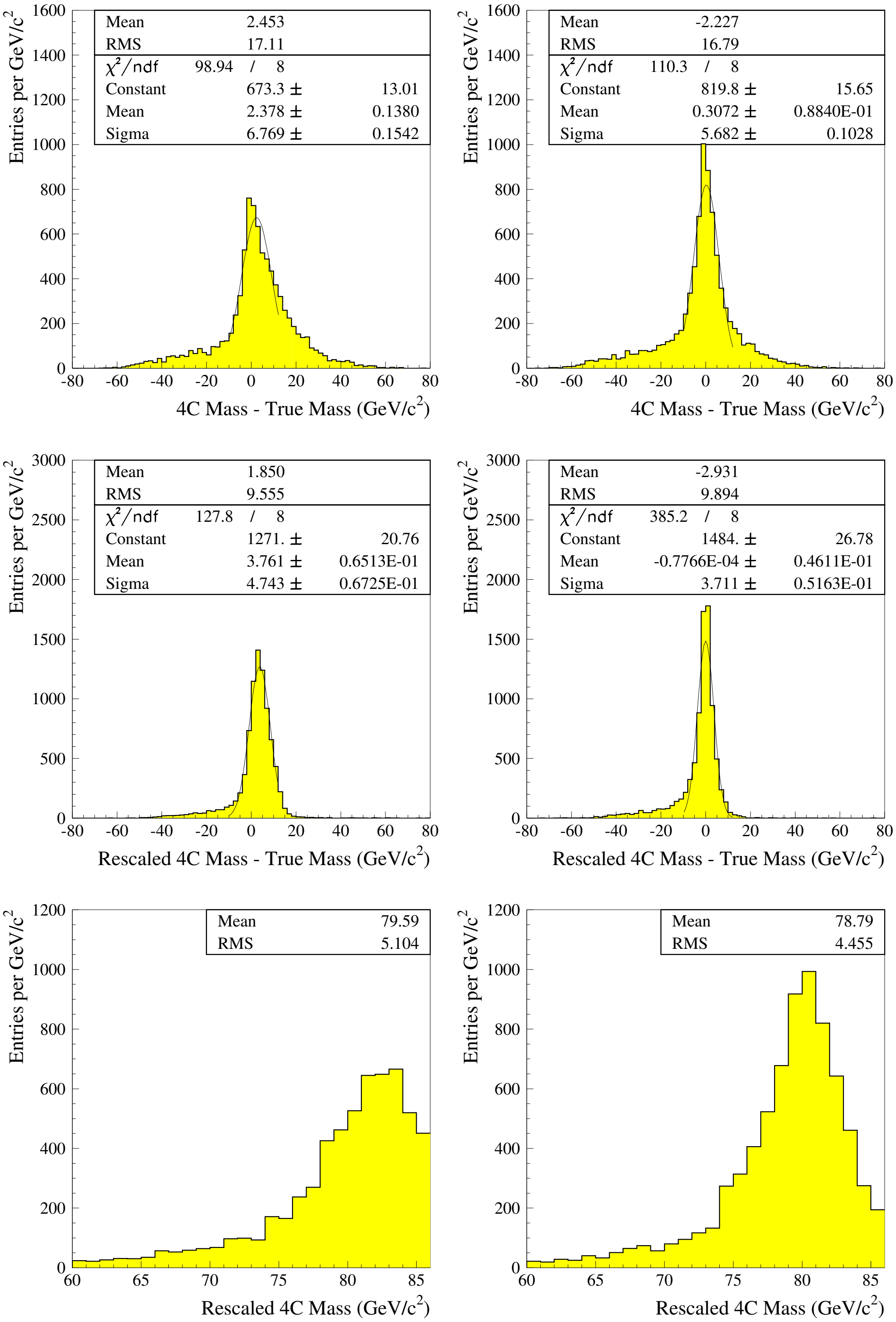

Figure 5.18: The mass resolution before (left hand plots) and after (right hand plots) selecting and removing ISR photons observed in the ALEPH detector, obtained from WW Monte Carlo events containing an ISR candidate photon. The top plots are the result of a 4C kinematic fit, the middle plots after rescaling, and the bottom plots the result of applying the jet pairing and mass window algorithm.

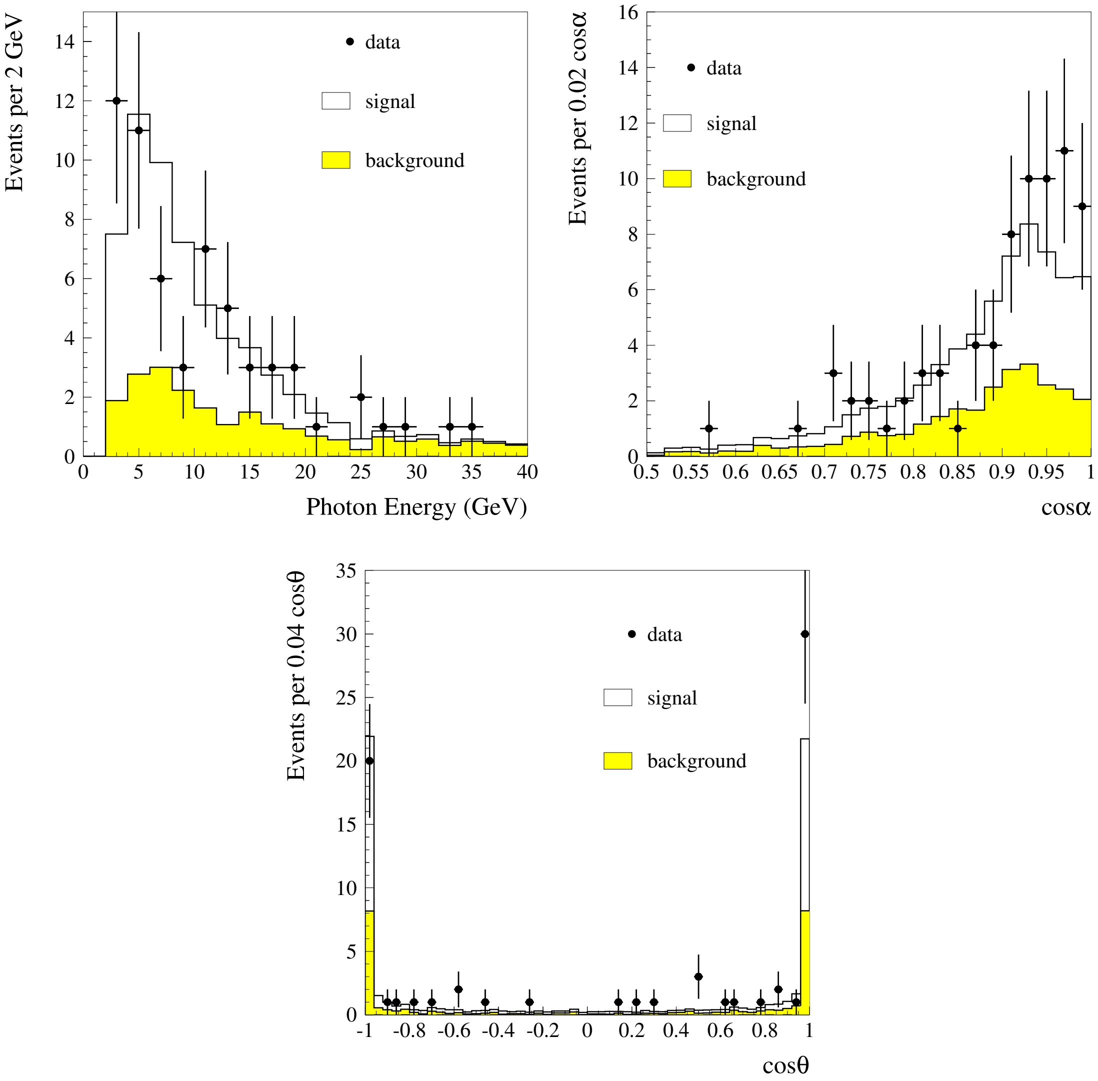

Figure 5.19: The comparison between data and Monte Carlo simulation for the ISR photon energy, angular separation, cos α, and angular distribution, cos θ, for hadronic WW candidate events containing an ISR candidate photon. The Monte Carlo distributions are represented by the histograms and are separated into signal, ie true WW events, and background, non WW events.

5.4 Jet Pairing

Once the kinematic fit has been performed the next step is to assign each of the four jets to one or the other of the two W bosons. There are three ways of doing this, neglecting differences between the W^+ and W^-, as shown in Table 5.5.

Combination	W_1	W_2
1	Jet 1 + Jet 2	Jet 3 + Jet 4
2	Jet 1 + Jet 3	Jet 2 + Jet 4
3	Jet 1 + Jet 4	Jet 2 + Jet 3

Table 5.5: Different jet pairing possibilities.

The algorithm used by ALEPH at 183 GeV [80, 62] was based upon the difference between the two invariant masses formed by the jets assigned to each W, the angle between these jets, and also cuts applied to the dijet invariant masses (the mass-window criterion). For this analysis a new algorithm has been developed in which the `CC03` matrix element is used in place of the dijet invariant mass difference [81]. The combination chosen is the one with the largest value of the matrix element squared:

$$\left| \mathcal{M} \left(M_{\mathrm{W}}^{ref}, \Gamma_{\mathrm{W}}^{ref}, p_i^1, p_i^2, p_i^3, p_i^4, \right) \right|^2 , \tag{5.19}$$

where M_{W}^{ref} is a reference mass chosen to be 80.35 GeV/c^2, $\Gamma_{\mathrm{W}}^{ref}$ is the corresponding Standard Model prediction for the W width, 2.094 GeV/c^2, and p_i^j is the four-momentum of the j-th jet. The first combination is rejected if it has the smallest sum of dijet opening angles, and the combination with the second largest matrix element squared is chosen instead. Both masses must lie between 60 GeV/c^2 and 86 GeV/c^2 and at least one of the masses must lie in the range 74 GeV/c^2 to 86 GeV/c^2. If the first combination does not satisfy the mass window condition then the second combination is chosen if it satisfies the mass window and does not have the smallest sum of dijet opening angles. If the second combination fails these requirements then the event is rejected. The combination with the largest matrix element squared is chosen in 90% of selected events and the second combination 10%. The final number of selected and observed events is summarised in Table 5.6. The number of observed events is less than the number of expected events as explained in Section 4.2.2.

$\sqrt{s}$ (GeV)	$\mathcal{E}$ (%)	$\mathcal{P}$ (%)	Events Expected	Events Observed
188.6	76.4	84.7	1214	1093
191.6	73.5	85.7	194	206
195.5	70.2	86.2	519	487
199.5	65.4	86.5	525	494
201.6	63.1	86.7	247	208

Table 5.6: The expected and observed number of events after all selection cuts.

5.5 Invariant Mass Distribution

After reconstruction of the events a final invariant mass distribution is obtained. Figure 5.20 shows a comparison of this distribution for data and Monte Carlo simulation with an input W mass of 80.35 GeV/c^2. Reasonable agreement is seen, although it is clear from this plot that the data prefers a higher value for the W mass. The W mass is actually extracted from a two dimensional distribution as shown in Figure 5.21, where the data and Monte Carlo distributions are plotted separately to show the fluctuations in the data sample that are smoothed out in the Monte Carlo.

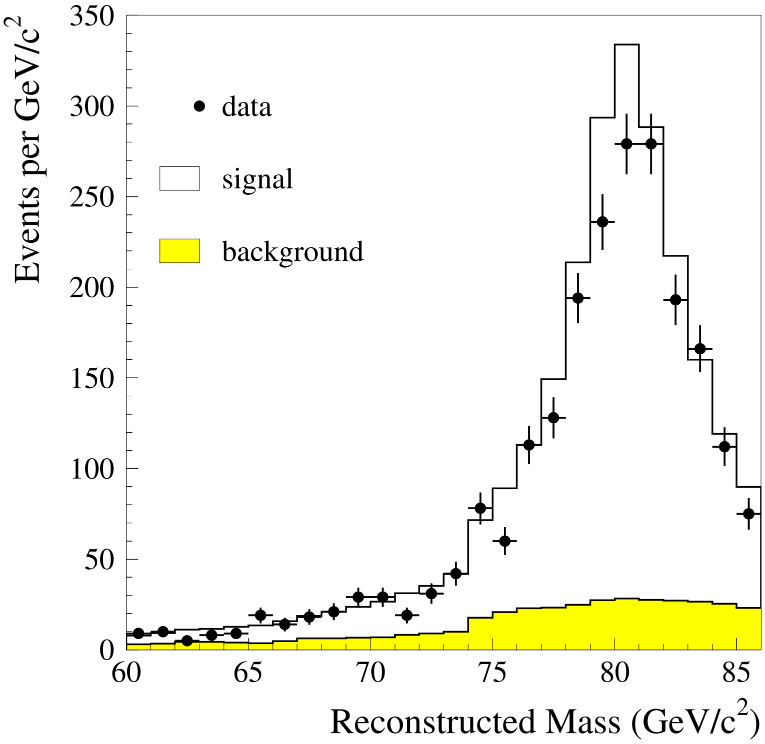

Figure 5.20: The reconstructed mass distribution for the $\sqrt{s} = 188.6$ GeV data and Monte Carlo. The WW Monte Carlo has been generated with an input mass of 80.35 GeV/c^2. The Monte Carlo distributions are represented by the histograms and are separated into signal, ie true hadronic WW events, and background, all other events.

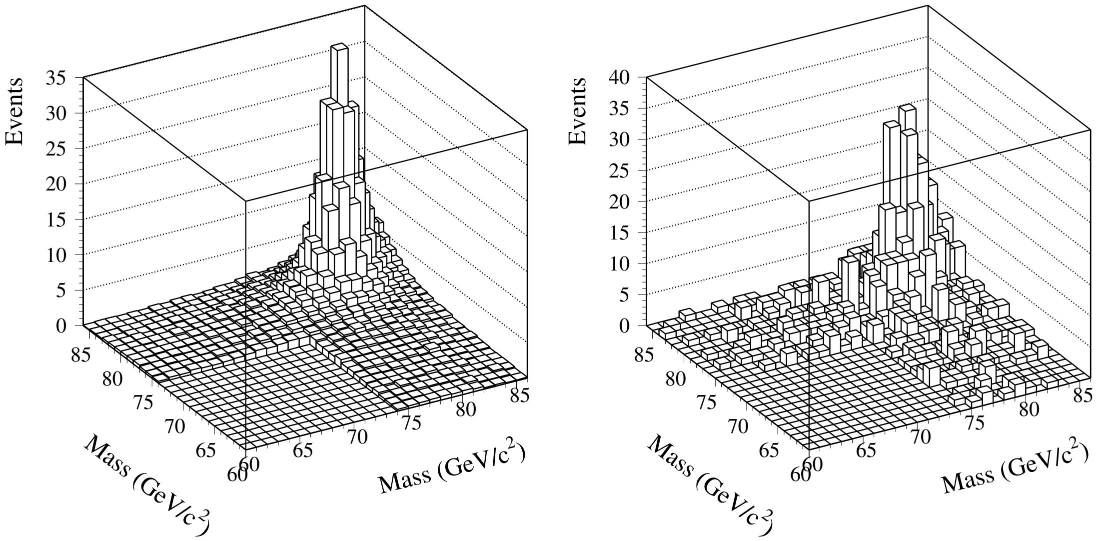

Figure 5.21: The two dimensional reconstructed mass distributions for Monte Carlo (left) and data (right). The statistical fluctuations in the data sample are clear.

Chapter 6

W Mass Extraction

6.1 Mass Extraction Methods

Several different techniques exist for extracting the W mass from the reconstructed dijet invariant mass distribution. A brief description of some of these is now given before the technique of Monte Carlo reweighting as used in this analysis is described in more detail.

6.1.1 Breit-Wigner Fit

An analytical function such as a double Breit-Wigner is used to fit the invariant mass distribution. In general the fitted function will not be able to describe the experimental distribution perfectly due to effects such as initial state radiation, background contamination and detector resolution. This fact leads to a bias in the fitted W mass which must be corrected for using calibration, whereby Monte Carlo samples generated at several different W mass values are treated as data and their W mass fitted. The response of the fitted W mass to the W mass at which the Monte Carlo is generated is then found. This calibration provides a source of systematic uncertainty in the measurement.

6.1.2 Convolution

The convolution method is an extension of the simple Breit-Wigner fit, taking into account the detector response. An analytical function describing the underlying physics of the event is convoluted with a function describing the detector resolution on an event by event basis. Generally the physics function is more complete, and is often the differential cross section in terms of the two invariant masses, usually including an ISR description. This method uses a lot of computation time, making stability and systematic checks difficult. Although as much information as practical is included the convolution method also needs calibrating. Studies have shown this method to be not quite as statistically powerful as the Monte Carlo reweighting technique [82].

6.1.3 Monte Carlo Interpolation

A large number of Monte Carlo samples are generated with different W masses. The event selection and invariant mass reconstruction is carried out for each of these samples in order to obtain an invariant mass distribution that can be directly compared with that obtained from the data. A χ^2 quantity that describes how well the data distribution fits the different Monte Carlo distributions is constructed and then the best estimate for the fitted W mass is obtained by interpolation between the Monte Carlo W mass points. This method has the advantage that the Monte Carlo and data events are treated in exactly the same way so that no calibration is needed. The major disadvantage of this method and the one that stops it being used in practice is the huge number of Monte Carlo events needed, taking far too much computation time to generate.

6.2 Monte Carlo Reweighting

Monte Carlo reweighting is the method used to extract the W mass in the analysis described in this thesis. It follows directly from Monte Carlo interpolation, but the technique of reweighting removes the need for many different samples of Monte Carlo events.

6.2.1 Principle

A large sample of Monte Carlo events are generated at a reference W mass, M_{W}^{ref}, and the invariant mass distribution obtained in the same way as for the data. This distribution can be made to correspond to the invariant mass distribution obtained from a sample of Monte Carlo at a different W mass, M_{W}^{0}, by reweighting. The reweighting is carried out on an event by event basis, the weight for each event being calculated using the `CC03` matrix elements for the event. These matrix elements depend on the W mass, W width, and four-momenta of the four fermions produced by the WW decay. Since the weight, given by

$$w_i\left(M_{\mathrm{W}}^{0},\Gamma_{\mathrm{W}}^{ref}\right)=\frac{\left|\mathcal{M}\left(M_{\mathrm{W}}^{0},\Gamma_{\mathrm{W}}^{ref},p_i^1,p_i^2,p_i^3,p_i^4,\right)\right|^2}{\left|\mathcal{M}\left(M_{\mathrm{W}}^{ref},\Gamma_{\mathrm{W}}^{ref},p_i^1,p_i^2,p_i^3,p_i^4,\right)\right|^2}, \tag{6.1}$$

is an event weight, distributions other than the invariant mass may be reweighted, possibly allowing for improvements in the statistical uncertainty on the measured W mass by fitting several mass dependent distributions at once. Previous studies [62] have shown that the effect on the fitted mass of using the `CC03` matrix element instead of the full four fermion matrix element is negligible, a difference of approximately 3 MeV/c^2 was observed at $\sqrt{s}=172$ GeV [62], whilst taking less computation time to calculate.

Invariant mass distributions are produced by the reweighting technique corresponding to W masses in the region between 79 GeV/c^2 and 82 GeV/c^2, separated by 25 MeV/c^2. These distributions are fitted to the data distribution, with linear interpolation to masses intermediate to those generated. This interpolation has a negligible effect on the fitted W mass and greatly speeds up the fitting process [62]. Previous studies have shown that the statistical precision of the measurement may be improved by using a two dimensional mass distribution [62] in place of a one dimensional distribution. Each dimension in this distribution is one of the two reconstructed masses obtained after the 4C kinematic fit, rescaling and jet pairing procedure. The alternative to using a two dimensional distribution is to reweight two one dimensional distributions independently and then combine the results taking into account the expected correlation between the two fitted masses, and in fact this method was used for the low statistics measurement at $\sqrt{s}=172$ GeV [83]. When the two dimensional distribution is used the improvement in the statistical precision arises because the correlations are taken into account on an event by event basis. At $\sqrt{s}=183$ GeV the improvement in the expected precision of the measurement was 10% [62].

6.2.2 Construction of Probability Density Function

The Monte Carlo reference invariant mass distribution is the sum of two separate distributions, one for signal and one for background, each binned separately. Each event gives a single coordinate on the two dimensional mass plane (M_1, M_2) which is then reflected about the diagonal of this plane in order to reduce statistical fluctuations in the probability density function. The probability density function for a data event to have a particular invariant mass coordinate is then taken as the sum of the signal and background distributions:

$$pdf_{data} = pdf_{signal} + pdf_{bkg} = \mathcal{P}_s \left(M_{\mathrm{W}}^0 \right) \frac{N_{ij}^s \left(M_{\mathrm{W}}^0 \right)}{\Delta_{ij}^s N_{tot}^s} + \mathcal{P}_b \left(M_{\mathrm{W}}^0 \right) \frac{N_{kl}^b}{\Delta_{kl}^b N_{tot}^b}, \tag{6.2}$$

where (i, j) is the signal bin in which the event falls and (k, l) is the background bin. The area of the bin is Δ and is defined as $\left(\delta M_i^s \times \delta M_j^s \right)$ and $\left(\delta M_k^b \times \delta M_l^b \right)$ for signal and background respectively. The number of background events found in the bin (k, l) is N_{kl}^b; for signal the number of events in the bin (i, j) depends on the W mass that the distribution has been reweighted to:

$$N_{ij}^s \left(M_{\mathrm{W}}^0 \right) = \sum_{ievt=1}^{N_{ij}^{ref}} w_{ievt} \left(M_{\mathrm{W}}^0 \right) . \tag{6.3}$$

N_{ij}^{ref} is the number of events in bin (i, j) when the events are unweighted and $M_{\mathrm{W}}^0 = M_{\mathrm{W}}^{ref}$. The event weight, w_{ievt}, is taken from Equation 6.1. N_{tot}^s and N_{tot}^b are the total number of signal and background events on the (M_1, M_2) plane. $\mathcal{P}_s$ is the signal purity, the background purity is just $\mathcal{P}_b = 1 - \mathcal{P}_s$. The signal purity is defined as:

$$\mathcal{P}_s \left(M_{\mathrm{W}}^0 \right) = \frac{\mathcal{E}_s \sigma_s \left(M_{\mathrm{W}}^0 \right)}{\mathcal{E}_s \sigma_s \left(M_{\mathrm{W}}^0 \right) + \mathcal{E}_b \sigma_b}, \tag{6.4}$$

where $\mathcal{E}_s$ and $\mathcal{E}_b$ are the efficiencies for selecting signal and background events respectively and σ_s and σ_b are the signal and background cross sections. The WW cross section depends on the W mass and so this dependence has to be included in the probability density function to ensure the correct signal to background normalisation. In the region where the fit is performed the variation is small and is parametrised with a parabola around $M_{\mathrm{W}}^0 - M_{\mathrm{W}}^{ref}$. The parabola has the form

$\sigma_s\left(M_W^0\right) = \sigma_s\left(M_W^{ref}\right)\left(1 + a\left(M_W^0 - M_W^{ref}\right) + b\left(M_W^0 - M_W^{ref}\right)^2\right)$, and is determined using the `GENTLE` package [65]. The variation of the WW cross section with the W mass is shown in Figure 6.1. The efficiencies are determined from Monte Carlo and are assumed to have no dependence on the W mass, as was shown in Section 4.2.2.

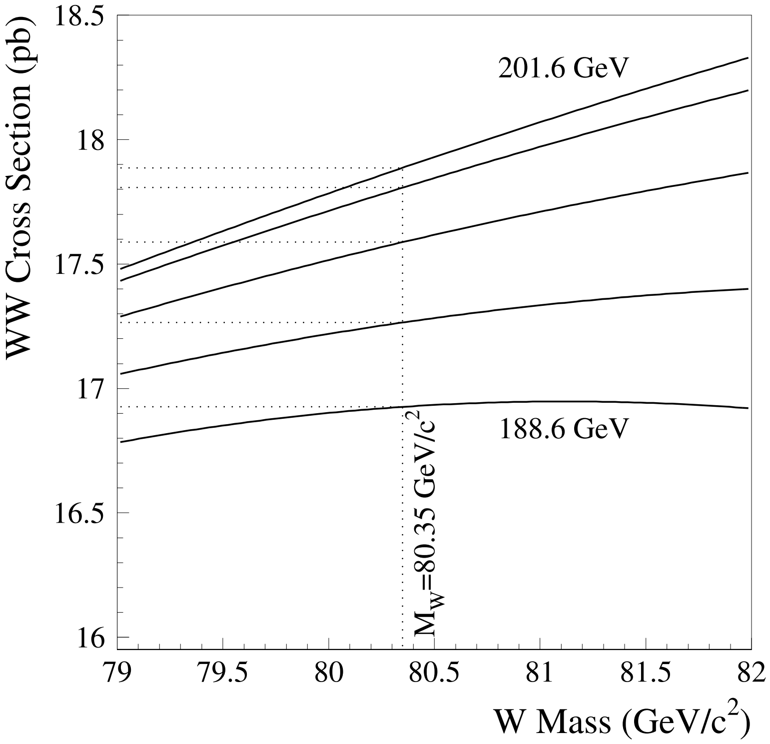

Figure 6.1: The parametrisation of the WW cross section as a function of the W mass, for centre of mass energies between 188.6 GeV (bottom curve) and 201.6 GeV (top curve).

6.2.3 Binning of Probability Density Function

The probability density function is binned separately for signal and background. This binning must be carefully chosen in order to minimise possible bias from the finite number of Monte Carlo events used to construct the p.d.f. while at the same time maximising the sensitivity to the W mass. As Figure 5.21 shows, the mass window criteria used in the jet pairing algorithm make the mass distribution fall into three different regions; the peak region and two tails. Previous studies [62] have shown that instead of using a fixed binning a better solution is to use a variable bin size for each of the three regions, demanding a minimum number of events in each bin. The minimum number of events in each bin, N_{ij}^{min}, determines the size of the bins. An initial binning is chosen which requires the same number of events in each bin, separately for each of the three regions. The number of bins is then adjusted iteratively until the number of events in each bin is greater than the minimum, N_{ij}^{min}.

The minimum number of events required has to be chosen carefully. If it is too large then sensitivity is lost in the measurement, while if it is too small the measurement becomes biased towards the reference mass used in the Monte Carlo. Studies have shown that the optimal number of bins to use is $N_{ij}^{min} = 200$ [63]. Figure 6.2 shows the binning used for signal and background. The regions most sensitive to the W mass are those where the bin size is smallest. Also shown in Figure 6.2 are scatter plots of the masses used to build the probability density function; the correlation between the two masses for the signal can be seen.

6.2.4 Maximisation of Likelihood

To find the best estimate of the W mass the probability density function obtained in the previous section is used to construct a likelihood function that depends upon the reconstructed invariant masses for each data event and the Monte Carlo W mass:

$$\mathcal{L}\left(M_{\mathrm{W}}\right) = \prod_{i=1}^{N_{evt}} pdf_{data}\left(M_1^i, M_2^i | M_{\mathrm{W}}^0\right) . \tag{6.5}$$

N_{evt} is the number of data events. This likelihood is then maximised to find the fitted value of the W mass. In practice the quantity $-2\ln\mathcal{L}$ is minimised using the `MINUIT` package [77].

The statistical uncertainty on the fitted W mass is by convention taken as the 68% confidence level region, as this corresponds to one standard deviation of a Gaussian distribution. In the limit of large sample sizes the logarithm of the likelihood is a parabola, with the minimum of $-2\ln\mathcal{L}$ at the fitted W mass. The statistical uncertainty may then be calculated analytically by inverting the second

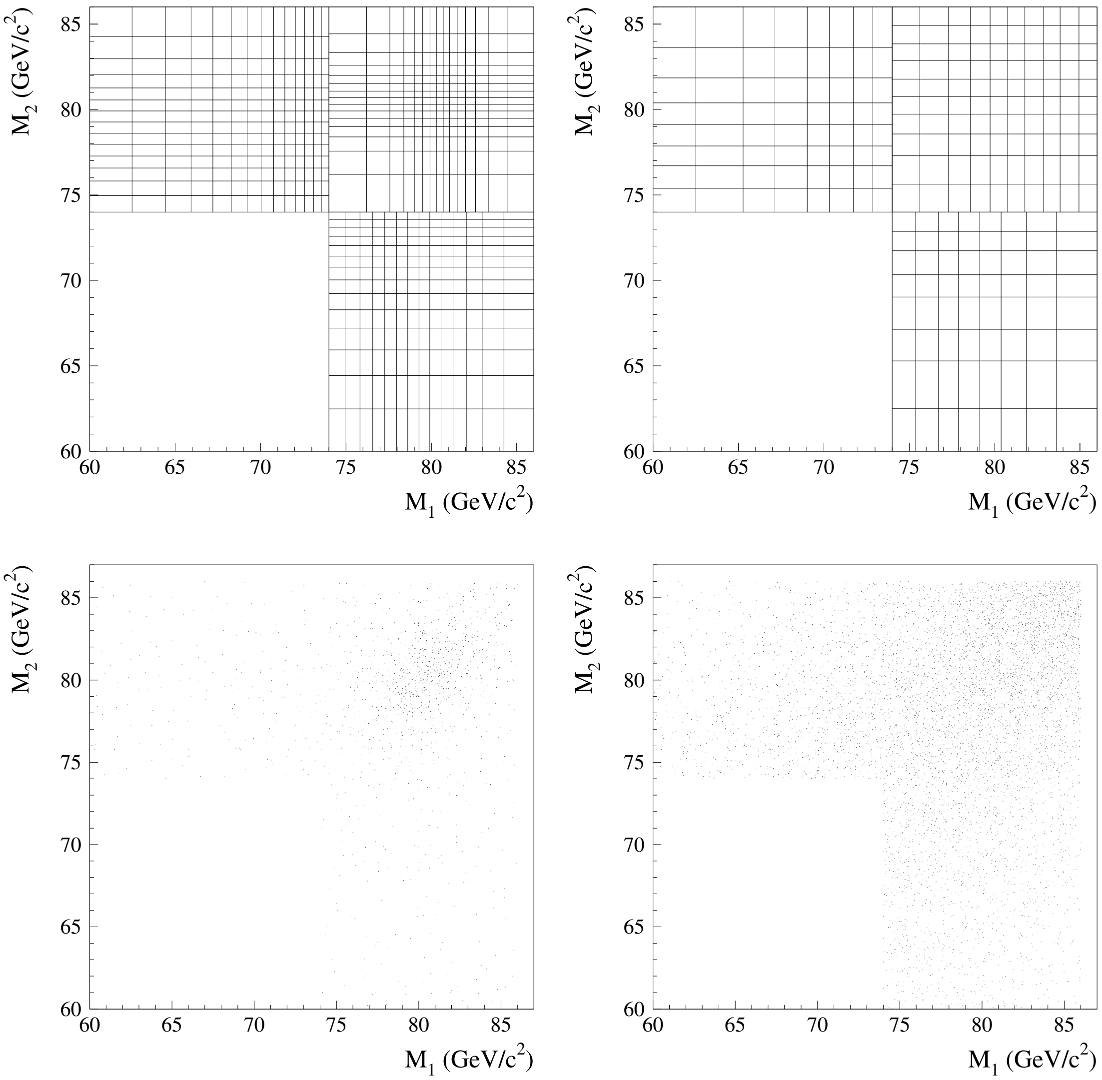

Figure 6.2: The top plots show the binning used for signal (left) and background (right). All bins contain more than the minimum of 200 entries. The bottom plots show the scatter plots of the Monte Carlo used to construct the probability density function for signal(left) and background(right).

derivative of $\ln \mathcal{L}$. In practice the 68% confidence level region is determined numerically, its boundaries occurring when the likelihood is one unit greater than at its minimum. The likelihood for the data fit at $\sqrt{s} = 188.6$ GeV is shown in Figure 6.3. This calculation of the fit uncertainty assumes that the errors are Gaussian and that the response of the analysis to the true W mass is linear. These checks are described in the following sections.

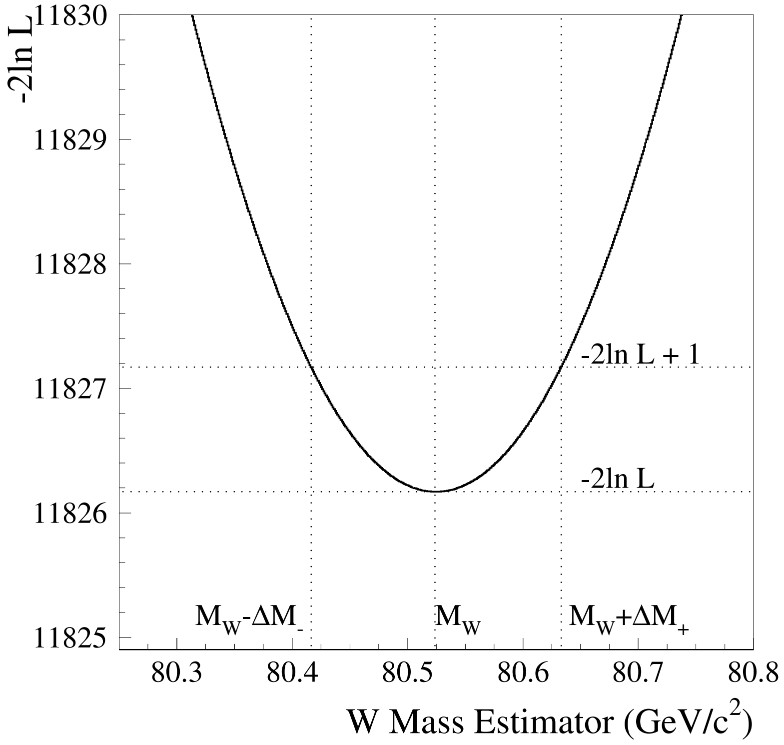

Figure 6.3: The quantity $-2 \ln \mathcal{L}$ (see text) as a function of the W mass. The fitted mass is given by the minimum of this quantity. The parabolic behaviour of the likelihood is clearly shown.

6.3 Monte Carlo Studies

6.3.1 Expected Statistical Uncertainty

In order to test that the fit uncertainty is a correct estimate of the statistical uncertainty on the W mass it is necessary to carry out many simulated experiments using Monte Carlo data. Many samples of Monte Carlo are used of the same size as the fitted data sample. The W mass is extracted from each of these samples in the same way as for the data. The distribution of these fitted masses should have a mean consistent with the W mass that the samples were generated with. The r.m.s. of the fitted mass distribution is called the "expected error" and is an estimate of the statistical uncertainty on the fitted mass. This value should also be consistent with the average value of the error distribution of the fits. The statistical uncertainty on the fitted data should also be compatible with the expected error. The distributions of masses and errors are shown in Figure 6.4. It can be seen that the fitted mass is consistent with the W mass used as input to the Monte Carlo, 80.35 GeV/c^2, and with a Gaussian distribution. The r.m.s. of this distribution is taken as the expected statistical uncertainty on the fitted W mass. It can also be seen that the positive statistical, negative statistical and parabolic uncertainties are all consistent with each other and with the expected uncertainty obtained from the r.m.s. of the mass distribution. The statistical uncertainty on the expected error is given by $100.7/\sqrt{2 \times 200} = 5.0$ MeV/c^2 while that on the average uncertainty is $2.1/\sqrt{200} = 0.1$ MeV/c^2, a factor of fifty smaller. Thus the average uncertainty is usually used to compare the statistical power of different analyses.

6.3.2 Linearity Check

As explained in Section 6.2 one great advantage of the method of reweighting is that the method does not need calibrating. This can be tested by fitting a large sample of Monte Carlo events as if they were data. The fitted mass should be the same as the mass used as input to the Monte Carlo, within the statistical uncertainty on the measurement, showing that the analysis is unbiased. The analysis should also have a linear response, that is the fitted mass should reproduce the true mass when it has a different value from the W mass used as input to the Monte Carlo reference. This can be tested using several samples of Monte Carlo, each generated at different input W masses. Samples of Monte Carlo were generated with 11 different W masses between 79.35 GeV/c^2 and 81.35 GeV/c^2, a straight line fit to the fit results shows that the analysis is indeed linear, as shown in Figure 6.5, with no bias.

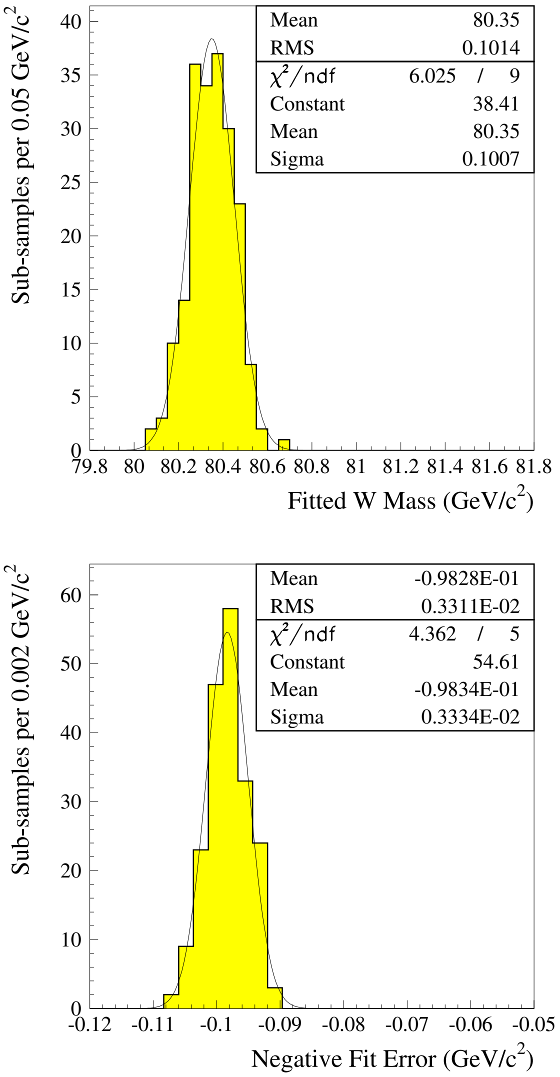

Figure 6.4: Fitted W mass and fit errors from 200 subsamples of Monte Carlo (see text). The fitted mass is shown in the top left plot. The other plots show the distributions of the positive and negative statistical uncertainty, and the parabolic uncertainty.

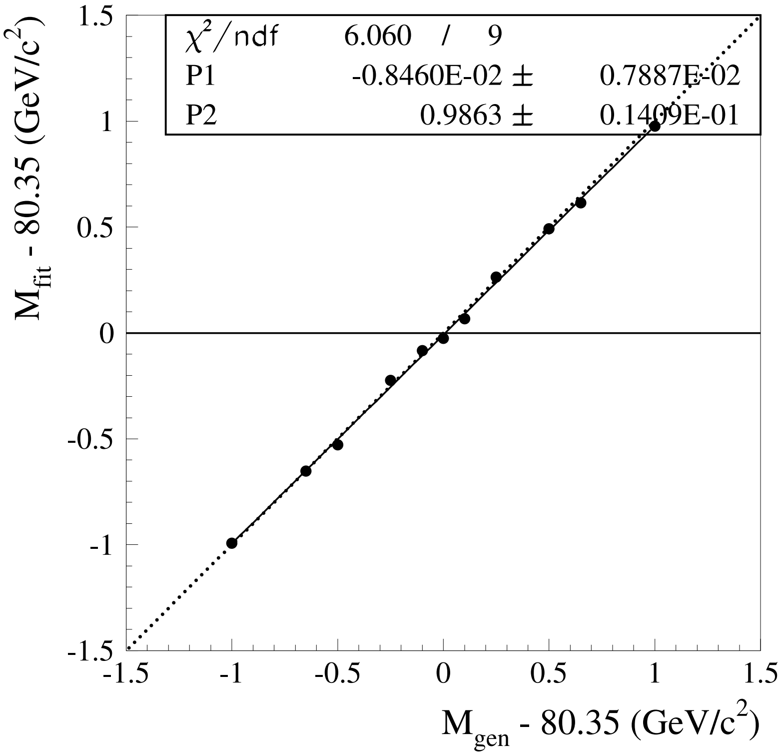

Figure 6.5: The fitted W mass, M_{fit}, versus the generated W mass M_{gen} (relative to the reference mass of 80.35 GeV$/c^2$) for eleven different Monte Carlo samples (points). The result of a straight line fit to the points is shown as a solid line and the values of the slope, P2, and offset, P1, are given in the plot together with the χ^2 of the fit. The dotted line has slope 1 and offset 0.

6.4 Data Fit Results

The results of the fit to the 1998 and 1999 data are shown in Table 6.1, together with the expected errors. The expected errors have been calculated according to both the observed luminosity and the observed number of data events. The observed uncertainty is compatible with the expected uncertainty for the same number of selected events. The fitted masses have had 27 MeV/c^2 added to them to account for the difference in the running width and fixed width schemes as explained in Section 2.3.3. The observed uncertainty on the fitted mass is quoted as the mean of the positive and negative fit uncertainties.

$\sqrt{s}$ GeV	Fitted Mass GeV/c^2	Statistical Uncertainty GeV/c^2	Expected Uncertainty for measured luminosity GeV/c^2	Expected Uncertainty for observed number of events GeV/c^2
188.6	80.551	0.108	0.101 ± 0.005	0.104 ± 0.005
191.6	80.270	0.268	0.237 ± 0.012	0.230 ± 0.011
195.5	80.447	0.142	0.132 ± 0.007	0.144 ± 0.007
199.5	80.311	0.157	0.148 ± 0.007	0.148 ± 0.007
201.6	80.471	0.246	0.210 ± 0.010	0.239 ± 0.012

Table 6.1: Results of the fit for the W mass from data, showing the observed and expected statistical uncertainties for the measurements.

6.5 Stability Checks

6.5.1 Neural Network Cut

The fitted mass as a function of neural network output cut is shown in Figure 6.6. The fitted mass is stable over a wide range of values for the cut.

6.5.2 Kinematic Fit

The complete reconstruction step was repeated using `KINFIT` instead of `ABCFIT` to do the kinematic fitting. A difference in the fitted mass of 10 MeV/c^2 was observed.

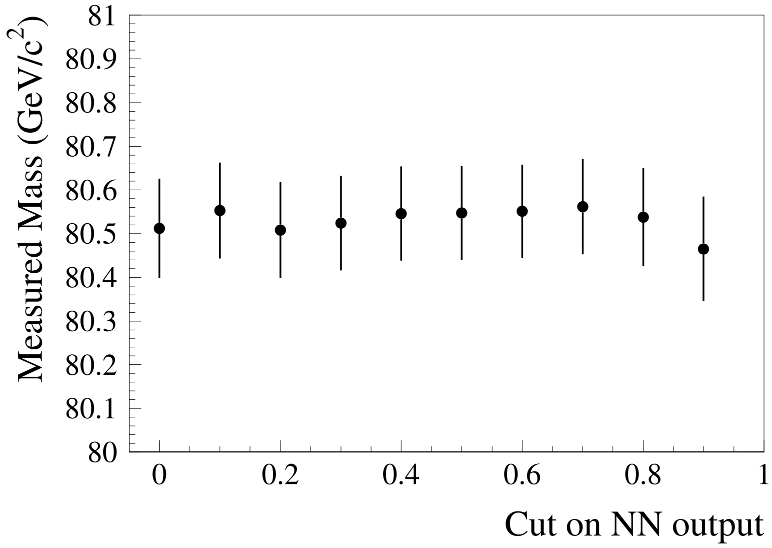

Figure 6.6: The measured W mass as a function of the cut on the neural network output.

6.5.3 Mass Window

The fitted masses for different values of the mass window criteria are shown in Table 6.2. The table shows that the fitted W mass is stable for a wide range of mass windows, as is the average statistical uncertainty determined from Monte Carlo. This is explained by the fact that although an increase in the mass window selects more events these events lie in the tails of the reconstructed mass distribution and so have little sensitivity to the W mass.

Tail Region (GeV/c^2)	Peak Region (GeV/c^2)	N_{data}	Fitted Mass (GeV/c^2)	Expected Uncertainty (MeV/c^2)	Average Uncertainty (MeV/c^2)
60-86	74-86	1093	80.551 ± 0.108	101 ± 5	98.2 ± 0.2
60-86	65-86	1132	80.559 ± 0.110	95 ± 5	98.6 ± 0.2
60-86	70-86	1120	80.549 ± 0.108	94 ± 5	98.1 ± 0.2
50-86	74-86	1141	80.546 ± 0.109	98 ± 5	98.0 ± 0.2
64-86	74-86	1063	80.545 ± 0.109	101 ± 5	98.2 ± 0.2
68-86	74-86	1002	80.553 ± 0.109	95 ± 5	98.2 ± 0.2
70-86	74-86	960	80.556 ± 0.108	104 ± 5	98.2 ± 0.2
72-86	74-86	911	80.561 ± 0.110	97 ± 5	98.4 ± 0.2
60-90	74-90	1287	80.591 ± 0.107	100 ± 5	97.4 ± 0.2

Table 6.2: The effect of varying the mass window on the fitted mass. Also shown are the number of data events, N_{data}, and the expected and average statistical uncertainties determined from 200 Monte Carlo samples of the same luminosity as the data.

Chapter 7

Systematic Uncertainties on the W Mass Measurement

The systematic uncertainties on the W mass are now very important, since the stage has been reached where the combined W mass from the four LEP experiments has a systematic uncertainty larger than the statistical uncertainty [84], and the statistical uncertainty will be reduced further with data taken in the year 2000. Much work is ongoing to gain a better understanding of these uncertainties, especially that due to fragmentation. This chapter describes the estimation of the uncertainties important to the analysis in this thesis, with emphasis on methods that have been improved since previous ALEPH W mass measurements, such as those used in the estimation of effects due to the ALEPH detector. The author's contribution to the results in this chapter is in the calculation of the systematic uncertainty due to finite Monte Carlo statistics, that due the uncertainty on the LEP energy measurement and the detector related effects.

7.1 ISR

The modelling of initial state radiation in the main Monte Carlo used in the analysis, `KORALW`, is performed to second order in the leading log approximation, $\mathcal{O}\left(\alpha^2 L^2\right)$, where L is the logarithm ln $\left(s/m_{\mathrm{e}}^2\right)$ as described in Section 2.3.4. To estimate the effect of higher order terms, $\mathcal{O}\left(\alpha^3 L^3\right)$, a sample of `KORALW` W pair events are weighted by the ratio of the first and second order matrix elements squared. These events are then treated as data and the W mass obtained compared with that obtained from the same unweighted events. The difference in masses is taken as an upper limit on the effect of the missing higher order terms; the difference is of the order of 5 MeV/c^2 [85].

7.2 Background

The expected amount of background remaining in the data sample after all analysis cuts (neural net selection and jet pairing) is about 15%. The relatively small data sample therefore makes it difficult to compare the properties of the data and Monte Carlo background events. A technique developed for previous analyses [86] is used that compares Z^0 data and Monte Carlo. This procedure uses a similar preselection to this W mass analysis to select events in the 1994 Z^0 data and Monte Carlo. The shape of several variables and the overall number of events are then compared. The effect of any discrepancies between data and Monte Carlo on the fitted W mass is evaluated by varying the background p.d.f. used in the reweighting step appropriately. A 5% variation in the number of background events is applied. The estimated uncertainty on the measured W mass is of the order of 5 MeV/c^2 [87].

7.3 Monte Carlo Statistics

As explained in Section 6.2.3 the finite number of Monte Carlo events used to build the reference p.d.f. contributes a systematic uncertainty to the measured W mass. The method of calculating the uncertainty for this measurement was developed for previous measurements [62] and follows an analytical approach, described in detail in Appendix C. The method is based on the fact that each bin in the reference probability distribution function has a different sensitivity to the W mass as the reference distribution is reweighted. The statistical contribution from each bin is calculated, and leads to an estimate of 5 MeV/c^2 for the uncertainty.

7.4 Detector Effects

The technique of reweighting relies on a good Monte Carlo simulation of both the underlying physics processes and the response of the ALEPH detector to these events. The simulation of the detector therefore has to be investigated in detail for possible discrepancies between the Monte Carlo simulation and the real data, and to ensure that these discrepancies are understood.

The technique used to estimate the uncertainties due to detector related effects is the same for all sources of uncertainty under investigation. A large sample of Monte Carlo events is used in place of data in order to increase the precision of the estimate, and to reduce the effects of statistical fluctuations due to the small size of the data sample. The W mass of this Monte Carlo sample is measured using the normal analysis. The detector related effect under investigation is then applied to the sample and the measurement of the W mass repeated. The difference in the masses is taken as the systematic uncertainty.

7.4.1 Jet Energy Corrections

As explained in Section 5.1.2 corrections are applied to the energy of jets in any Monte Carlo used in the analysis. These corrections are derived from Z^0 calibration data taken at the start and end of each year's data taking and Monte Carlo simulation. The systematic uncertainty on the W mass due to these corrections is estimated by varying randomly the bin to bin correction factors by their statistical uncertainty, which is about 0.3%, and taking the largest shift in the measured W mass as the systematic uncertainty. This is found to be about 5 MeV/c^2.

7.4.2 Calorimeter Simulation

The jet corrections described in the previous section are obtained after the energy flow algorithm has been run and are applied to the jet as a whole. The individual calorimeter energy depositions are treated in a similar way by considering differences between Z^0 data and Monte Carlo. The corrections obtained are applied to Monte Carlo and the energy flow and jets recomputed along with new jet energy corrections before finally estimating the systematic uncertainty on the W mass.

The simulation of the calorimeters in the Monte Carlo assumes that their energy calibrations are constant with time, however this is not the case and the calorimeters are constantly monitored to study the variations. The size of the fluctuations during 1998 were of the order of 0.4% for ECAL and 1.5% for HCAL [88]. Since the jet energy corrections are determined using data taken at the start and end of the data taking period then they also do not take the variations into account. A random smearing of the energy depositions in the calorimeters by these amounts is therefore applied to a Monte Carlo sample and the energy flow repeated.

The systematic uncertainty due to applying both the rescaling and smearing of the calorimeter energy deposits simultaneously is estimated to be 10 MeV/c^2.

7.4.3 Jet Energy Resolution

The jet energy resolution, $\sigma_{E_{jet}}$, is also studied using Z^0 data and Monte Carlo, in the same way as the jet energy itself. The comparison of 1998 Z^0 data and Monte Carlo jet energy resolutions is shown in Figure 7.1 together with the comparison of the jet energies. It can be seen that the statistical uncertainty of the comparison of the resolution is greater than that for the jet energy and is at a level of about 2%, but reasonable agreement is seen over the whole angular range except for the low angle regions at $|\cos\theta| > 0.95$. Here the discrepancy is as large as 10%. Therefore, the jet energies of a Monte Carlo sample are randomly smeared by the appropriate amounts, depending on the jet polar angle, and the systematic uncertainty on the W mass estimated. This is approximately 7 MeV/c^2.

7.4.4 Jet Angular Bias

Any angular bias due to misalignment of the detector would be very hard to detect. Hadronic Z^0 decays produce two jets that are back to back and we have no knowledge of their true production angle. The charged particle tracking detectors and the ECAL are, however, aligned independently. It is therefore possible to study if there is any possible source of discrepancy between data and Monte Carlo in the angular measurement by looking at the different components of jets.

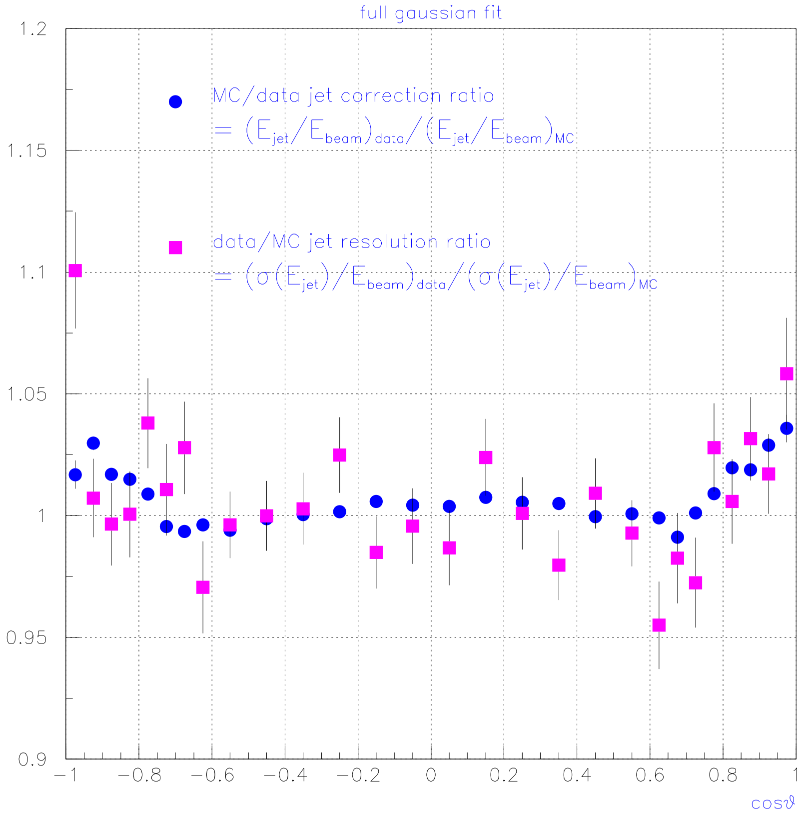

Figure 7.1: The ratios $\frac{(E_{jet}/E_{beam})_{data}}{(E_{jet}/E_{beam})_{MC}}$ and $\frac{\left(\sigma_{E_{jet}}/E_{beam}\right)_{data}}{\left(\sigma_{E_{jet}}/E_{beam}\right)_{MC}}$ as a function of polar angle. The ratios are determined from 1998 Z^0 peak data and Monte Carlo. The largest discrepancies between data and simulation are seen in the low angle regions. Taken from [88].

The two largest components are charged particles, measured by the tracking detectors, and photons measured by ECAL. The polar angle difference between the photonic and charged particle components of jets, $\theta_{hadrons} - \theta_{photons}$, is examined using Z^0 peak data and Monte Carlo simulation. Figure 7.2 shows this difference as a function of polar angle. It can be seen that the difference is less than 2 mrad, which is the statistical sensitivity of the measurement. Studies using higher statistics from the 1994 Z^0 data taking period show that the difference between data and Monte Carlo is small except in the region of the overlap between the endcap and barrel calorimeters. The result of a fit to the 1994 data is shown by the line in Figure 7.2. The systematic uncertainty on the W mass due to a 2 mrad angular bias is estimated to be less than 5 MeV/c^2.

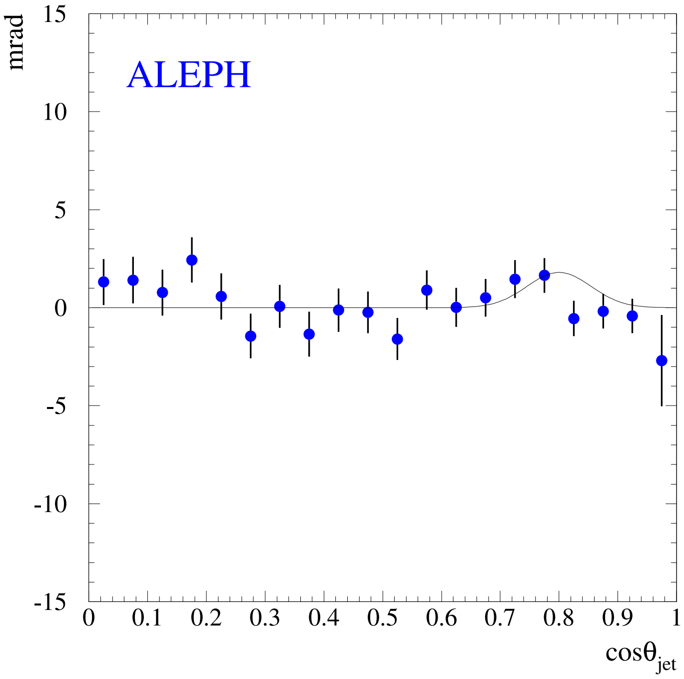

Figure 7.2: The difference of data and Monte Carlo for the quantity $\theta_{hadrons} - \theta_{photons}$ as a function of jet polar angle, determined from 1998 Z^0 data and Monte Carlo. The line is a functional fit to higher statistics data from 1994, showing the discrepancy observed in the overlap region of the barrel and endcap calorimeters. Taken from [74].

7.4.5 Jet Angular Resolution

The fact that Z^0 decay jets should be back to back can be exploited to study the angular resolution of the jets. It is found that the resolution is slightly better in the Monte Carlo simulation than the data [88]. An additional random smearing is thus introduced to the jet angles in the Monte Carlo to account for this discrepancy. The systematic uncertainty on the W mass due to this smearing is small, less than 5 MeV/c^2.

7.4.6 Charged Particle Tracking

The tracking detectors that measure charged particles are aligned with each other using the Z^0 calibration data. Small systematic differences between positive and negative charged tracks are observed in the data. These differences are proportional to momentum, and so are more important for the W mass measurement using semileptonic W decays which relies on the accurate measurement of a single high energy lepton. Corrections determined from $Z^0 \rightarrow \mu^+\mu^-$ events are applied to data events to account for the distortions. In order to estimate the systematic uncertainty on the W mass due to these corrections the corrections are applied to a sample of Monte Carlo events and the measured W mass compared with that obtained with no correction. The effect is about 3 MeV/c^2.

7.5 LEP Energy

As explained in Section 5.2 the LEP beam energy enters directly in the kinematic fit, and also after fitting in the rescaling of the dijet masses by the beam energy. Any uncertainty in the measurement of the LEP beam energy therefore contributes an uncertainty to the measured W mass. Through the rescaling formula it may be expected that the fractional uncertainty in the beam energy translates directly to a fractional uncertainty on the mass:

$$\frac{\sigma^{LEP}_{M_{\mathrm{W}}}}{M_{\mathrm{W}}} = \frac{\sigma_{E_{beam}}}{E_{beam}}, \tag{7.1}$$

This is tested by taking a sample of Monte Carlo, changing the LEP energy in the kinematic fit and rescaling steps and fitting the W mass. Figure 7.3 shows that the relationship between the mass obtained and the LEP energy assumed is indeed linear with a gradient as expected. The total uncertainty on the LEP beam energy was 20 MeV in 1998 [44] and 21 MeV in 1999 [45], translating into uncertainties on the W mass of 17 MeV/c^2 in both years.

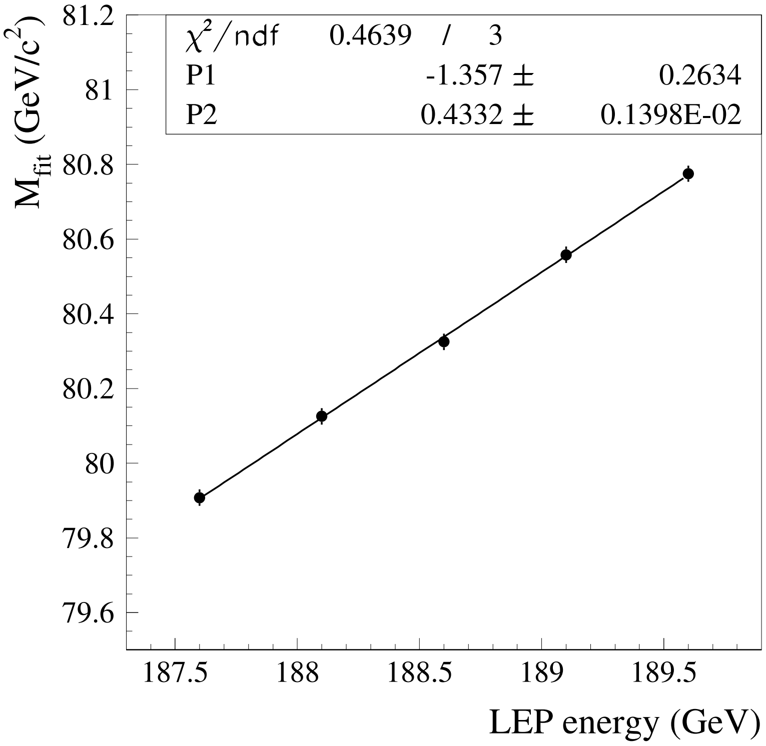

Figure 7.3: The fitted W mass as a function of the LEP centre of mass energy (points). The result of a straight line fit to the points with slope P2 and offset P1 is shown on the plot as the solid line.

7.6 Fragmentation

In the fully hadronic WW decay channel the fragmentation of the decay partons into jets needs to be well simulated, because reconstructed jets are used to form the invariant mass distribution from which the W mass is extracted. The Monte Carlo used throughout the analysis uses the `JETSET` fragmentation model [22]. The systematic uncertainty on the fitted W mass due to this model is very difficult to estimate since the effect of the fragmentation model is convoluted with the detector resolution and features of the analysis such as jet clustering and pairing.

The method used to estimate the uncertainty for this analysis involves comparing the `JETSET` model with that of another Monte Carlo package, `HERWIG` [24, 23]. The `HERWIG` fragmentation parameters are optimised using Z^0 data [89]. Studies of fragmentation related properties, mainly those related to the jets such as jet mass, derived from WW data and Monte Carlo show that this `HERWIG` tuning describes the data as well as the `JETSET` tuning [89]. A large sample of WW events, some 600,000, is generated using `KORALW` and then fragmented using both `JETSET` and `HERWIG`. This sample is then split into several smaller samples and the W mass evaluated for each sub-sample and each fragmentation model using the normal analysis. The mean difference between the measured W masses, `JETSET` $-$`HERWIG`, is taken as the systematic uncertainty due to the fragmentation model. This is calculated to be -30 ± 10 MeV$/c^2$ [90].

Studies are continuing to understand further this systematic uncertainty as it is currently the largest uncertainty on the LEP combined W mass. This is because it is taken as fully correlated between all decay channels, experiments, and years. The efforts are focussed on studying different distributions related to fragmentation, such as jet mass. The Monte Carlo distributions can be reweighted to exactly reproduce the data distributions. The weights can be propagated through to the invariant mass distribution and the W mass shift evaluated. The largest shift observed is of the order of 20 MeV$/c^2$ for both the `HERWIG` and `JETSET` Monte Carlos. However, the source of the overall difference between `JETSET` and `HERWIG` is not understood using this technique as the mass shifts observed for each variable are similar for each model [91].

7.7 Final State Interactions

Two possible sources of systematic uncertainty that only affect the fully hadronic decay channel have been suggested. These are both final state interactions that are not simulated by the standard `KORALW` Monte Carlo used for the analysis. They arise because the decay of a W typically takes place over a shorter space-time distance than the hadronisation scale, leading to a possible overlap of the two decays of the W bosons produced in the event.

The first effect is colour reconnection between the final state partons [25]. Theorists have suggested that the effect of colour reconnection is expected to be small during the perturbative phase of hadronisation, but could possibly be large during the non-perturbative phase. The only models existing for the non-perturbative phase are purely phenomenological, but currently provide the only means to estimate the systematic uncertainty on the W mass.

The second final state effect is that of Bose-Einstein correlations between identical hadrons produced by different W bosons [32], typically pions. The enhancement of the production of pions close in momentum space has already been observed in Z^0 decays at LEP1 [92] and semi-leptonic WW decays at LEP2 [93]. The closeness of the W's during their decay leads to the expectation that the production of identical pions from different W's could also be enhanced, possibly leading to a systematic bias in the measured W mass. Again, the only models for Bose-Einstein correlations are phenomenological. All values quoted in the following section may be found in Reference [94].

7.7.1 Colour Reconnection Effects

The estimation of the systematic uncertainty on the W mass due to colour reconnection is performed using many different phenomenological models in the different Monte Carlo fragmentation packages `JETSET`, `ARIADNE` and `HERWIG`.

`JETSET` includes the Sjöstrand and Khoze models SK1, SK2 and SK2′ [25]. A sample of events is generated with KORALW and then passed through the standard `JETSET` fragmentation package and all three modified versions, before being passed through the ALEPH detector simulation.

In the SK2 model colour strings are seen as vortex lines with thin cores. Reconnection takes place if the cores of two strings cross each other. SK2′ varies in that reconnection only takes place if the overall string length is shortened by the reconnection. The shift in the W mass of these models is evaluated to be $+6 \pm 8$ MeV$/c^2$ for SK2 and $+4 \pm 8$ MeV$/c^2$ for SK2′.

In the SK1 model strings are seen as cylindrical bags with a Gaussian decrease in the colour field density in the transverse direction, which is approximately of the hadronic size. The probability for a particular event to be reconnected depends on the overlap, I, of the colour fields. The probability, $\mathcal{P}_{reco}$, is taken as $\mathcal{P}_{reco} = 1 - \exp{(-k_I I)}$, where k_I is a free parameter of the model. A sample of connected and unreconnected events can be made by only taking a reconnected event if the value of $\mathcal{P}_{reco}$ is larger than a random number generated between zero and unity, otherwise the unreconnected event is kept. If the fraction of events is required to be the same as for the SK2 model, $\sim$ 29% at 188.6 GeV, then $k_I = 0.65$. The shift observed in the W mass is then measured to be $+30 \pm 10$ MeV/c^2.

The events generated with `KORALW` were passed through the `ARIADNE` package using no colour reconnection and using the models AR2 and AR3 [28]. `ARIADNE` uses the Dipole Cascade Model [29, 30] in which the string length is determined in terms of a parameter, Λ, defined as $\Lambda = \sum \ln \left(m_i^2 / m_p^2 \right)$ where m_i is the invariant mass of the string segment i and m_p sets a typical hadronic mass scale. Reconnections between strings are allowed if the total Λ is reduced, multiple reconnections are allowed and also reconnections within the same W. The models differ in that AR2 restricts reconnections to gluons with energies below the W width, Γ_W, while AR3 does not. However, gluons above this energy are perturbative and have been shown to be radiated incoherently by two initial colour dipoles [29, 30]. AR3 is therefore theoretically disfavoured. It is also ruled out on the grounds that distributions such as the charged particle multiplicity do not agree between data and Monte Carlo. Only AR2 is considered therefore, and a mass shift of $+21 \pm 10$ MeV/c^2 is observed, corresponding to 51% of events being reconnected.

The `HERWIG` model was used with a reconnection probability of 1/9 corresponding to $1/N_C^2$, where N_C is the number of colours. A shift of $+20 \pm 10$ MeV/c^2 is observed.

The largest shift, and therefore that quoted for the systematic uncertainty on the W mass, is for the SK1 model, 30 MeV/c^2. It should be noted however that the reconnection probability is only chosen so that it agrees with the other `JETSET` models. Studies are ongoing to try and rule out some of these phenomenological models, or at least some part of them, using all the WW data collected. It is hoped that this will lead to an upper limit for the systematic uncertainty due to colour reconnection.

7.7.2 Bose-Einstein Correlations

The model considered for Bose-Einstein correlations is the `LUBOEI` model [32], implemented in `JETSET`. The model shifts the final state momenta of identical bosons in order to reproduce the two pion correlation function. However, once this is done the other final state particles also need shifting in momentum in order to restore energy and momentum conservation in the event. The model needs tuning in order to represent the data correctly and this is done using LEP1 Z^0 data.

A sample of events was generated with `KORALW` and hadronised in three different ways: standard `JETSET`, `JETSET` with the `LUBOEI` model for particles from the same W and `JETSET` with `LUBOEI` for all particles. The samples were then passed through the ALEPH detector simulation in the usual way. The uncertainty due to Bose-Einstein correlations is quoted as the mass shift between the first and third samples, measured to be $+29 \pm 21$ MeV/c^2. If the second sample is used instead of the third then a shift of only -3 ± 21 MeV/c^2 is observed, consistent with zero. The quoted uncertainty of 30 MeV/c^2 is conservative since recent measurements seem to disfavour Bose-Einstein correlations between pions from different W's [93].

7.8 Summary and Combination

Table 7.1 summarises the systematic uncertainties on the W mass measurement. The table is split into two parts, those uncertainties that are correlated between the measurements made from the different WW decay channels and those that are uncorrelated. It can be seen that the dominant uncertainties are those due to final state interactions, fragmentation, and the LEP beam energy. The latter two are the more important, however, due to the fact that they are taken as correlated. All these uncertainties are still being studied in the hope of gaining a better understanding of them and their correlations. For this reason the preliminary results from the 1999 data (given in Section 6.4) are quoted using the uncertainties calculated for the $\sqrt{s} = 188.6$ GeV data.

Source	ΔM_W (MeV/c^2)
Correlated Uncertainties	
Jet energy corrections	5
Jet energy resolution	7
Jet angular bias/resolution	5
Calorimeter simulation	10
Charged tracking	3
Fragmentation	30
ISR	5
LEP energy	17
Uncorrelated Uncertainties	
Reference MC statistics	5
Background contamination	5
Colour reconnection	30
Bose-Einstein statistics	30
Total Systematic Uncertainty	57

Table 7.1: The systematic uncertainties on the W mass measurement from the fully hadronic channel, calculated using the 1998 data and Monte Carlo.

Chapter 8

Combination of W Mass Results and Interpretation

The fitted W masses obtained using the method described in this thesis from the 1998 and 1999 data including the statistical and systematic uncertainties are shown in Table 8.1, where the systematic uncertainty has been broken down to show the contributions due to final state interactions and the measurement of the LEP beam energy separately. The 1998 result is the final ALEPH result and has been published in [74] while those for the 1999 data are preliminary results prepared for the 2000 spring conferences [95].

$\sqrt{s}$ (GeV)	M_W (GeV/c^2)		σ_{stat}		σ_{syst}		σ_{FSI}		$\sigma_{\rm LEP}$
188.6	80.551	±	0.108	±	0.035	±	0.042	±	0.017
191.6	80.270	±	0.268	±	0.035	±	0.042	±	0.017
195.5	80.447	±	0.142	±	0.035	±	0.042	±	0.017
199.5	80.311	±	0.157	±	0.035	±	0.042	±	0.017
201.6	80.471	±	0.246	±	0.035	±	0.042	±	0.017

Table 8.1: The W mass from the fully hadronic decay channel for the 1998 ($\sqrt{s} =$ 188.6 GeV) and 1999 ($\sqrt{s} =$ 191.6–201.6 GeV) ALEPH data.

These may be combined to give a value of the W mass for the 1998 and 1999 data of

$$M_{\rm W} = 80.453 \pm 0.070({\rm stat}) \ \pm 0.035({\rm syst}) \ \pm 0.042({\rm FSI}) \ \pm 0.017({\rm LEP}) \ {\rm GeV}/c^2 \,. \tag{8.1}$$

8.1 ALEPH Measurements

The results obtained in this thesis may be combined with those from the semi-leptonic and fully-leptonic decay channels and previous measurements using the method of direct reconstruction made at LEP centre of mass energies of 172 GeV [83] and 183 GeV [80]. The combination is done taking into account the correlated and uncorrelated systematic uncertainties as shown in Table 7.1, firstly considering the mass values from the fully-hadronic channel (M_{W}^{4q}) and other channels (M_{W}^{non-4q}) as different physical parameters in order to investigate if there is a significant difference due to final state interactions. The resulting average values are [95]:

$$\begin{aligned} M_{\mathrm{W}}^{4q} &= 80.467 \pm 0.064(\mathrm{stat}) \ \pm 0.035(\mathrm{syst}) \ \pm 0.042(\mathrm{FSI}) \ \pm 0.017(\mathrm{LEP})\ \mathrm{GeV}/c^2\,, \\ M_{\mathrm{W}}^{non-4q} &= 80.435 \pm 0.063(\mathrm{stat}) \ \pm 0.045(\mathrm{syst}) \ \pm 0.017(\mathrm{LEP})\ \mathrm{GeV}/c^2\,, \end{aligned}$$

with a χ^2/ndf of 7.81/6. The W mass measurements from the fully-hadronic channel are shown in Figure 8.1. Previous measurements at centre of mass energies of 172 GeV [83] and 183 GeV [80] are shown together with the measurement at 189 GeV from the 1998 data and at 192-202 GeV from the 1999 data given in Table 8.1. The 1999 values have been averaged to give a single data point in Figure 8.1 labelled as 19X GeV. The average value of the measurements from the four different centre of mass energies is also shown. The uncertainties shown in Figure 8.1 are formed by combining all the statistical and systematic uncertainties in quadrature.

A second fit is then performed to extract the difference between the two mass values when the systematic uncertainties due to final state interactions are not included. This gives a result of [95]:

$$M_{\mathrm{W}}^{4q} - M_{\mathrm{W}}^{non-4q} = +0.032 \pm 0.091\ \mathrm{GeV}/c^2\,, \qquad (8.2)$$

to be compared with the 0.042 GeV/c^2 uncertainty due to FSI. Thus the difference is not significant.

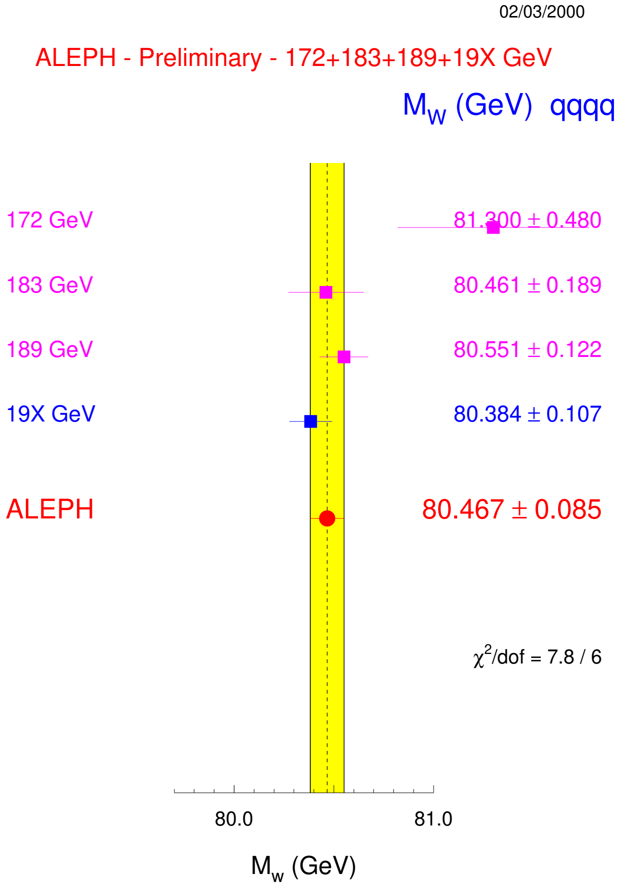

Figure 8.1: The measurements of the W mass using the method of direct reconstruction for the fully hadronic decay channel.

A final combination may be made to a single W mass parameter and including the result obtained from the WW cross section at 161 GeV [96] to give a value of [95]:

$$M_{\mathrm{W}} = 80.440 \pm 0.044(\mathrm{stat}) \;\pm 0.040(\mathrm{syst}) \;\pm 0.020(\mathrm{FSI}) \;\pm 0.017(\mathrm{LEP})\ \mathrm{GeV}/c^2\,, \tag{8.3}$$

with a χ^2/ndf of 8.67/8, as shown in Figure 8.2. The measurement from the fully-hadronic channel has a smaller weight than that from other channels because of the large uncertainty due to final state interactions, and the weight of the cross section measurement is very small.

8.2 LEP Measurements

The ALEPH W mass measurement may be combined with those made by the other LEP experiments, DELPHI [97, 98, 99, 100, 101], L3 [102, 103, 104, 105, 106], and OPAL [107, 108, 109, 110, 111] again taking into account the correlations in the systematic uncertainties, to give a combined LEP W mass of [112]

$$M_{\mathrm{W}} = 80.427 \pm 0.046\ \mathrm{GeV}/c^2\,, \tag{8.4}$$

as shown in Figure 8.3.

The difference between the masses from the fully-hadronic channel and all other channels may be determined, neglecting uncertainties due to final state interactions, and is found to be [112]

$$\Delta M_{\mathrm{W}} = 0.005 \pm 0.051\ \mathrm{GeV}/c^2\,, \tag{8.5}$$

which is compatible with zero.

8.3 Tevatron Measurements

The Tevatron collider at Fermilab near Chicago is a proton anti-proton collider with a centre of mass energy of 1.8 TeV. W bosons are produced by $\mathrm{q\bar{q}}$ annihilation. The large QCD background means that only those events in which the W decays to either an electron or a muon are considered. The lepton momentum

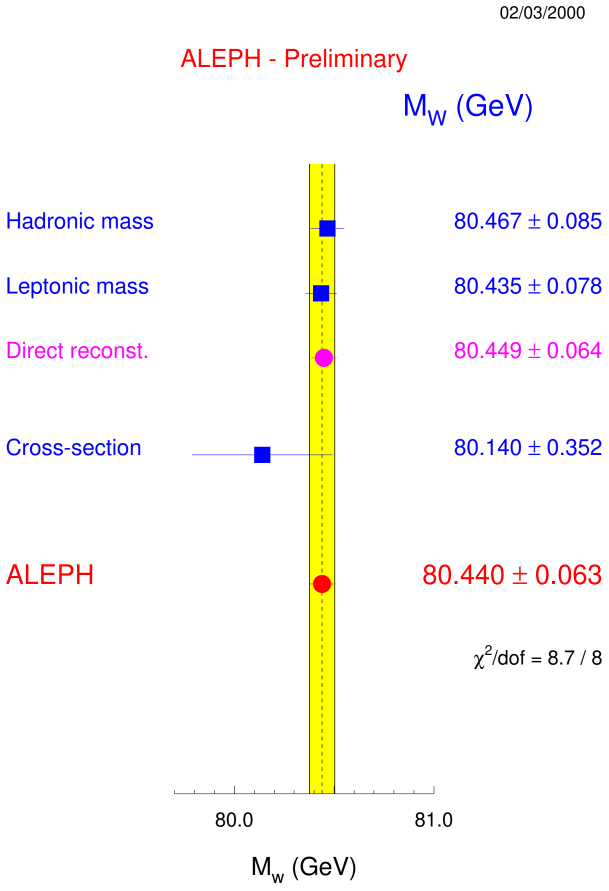

Figure 8.2: The ALEPH average W mass. The hadronic mass is referred to as M_W^{4q} and the leptonic mass as M_W^{non-4q}. The direct reconstruction value is the weighted average of these two measurements. The point labelled as cross-section is extracted from the threshold WW cross section [96]. The average of this measurement with the direct reconstruction measurements gives the ALEPH average W mass. The individual uncertainties are the total combined statistical and systematic uncertainties.

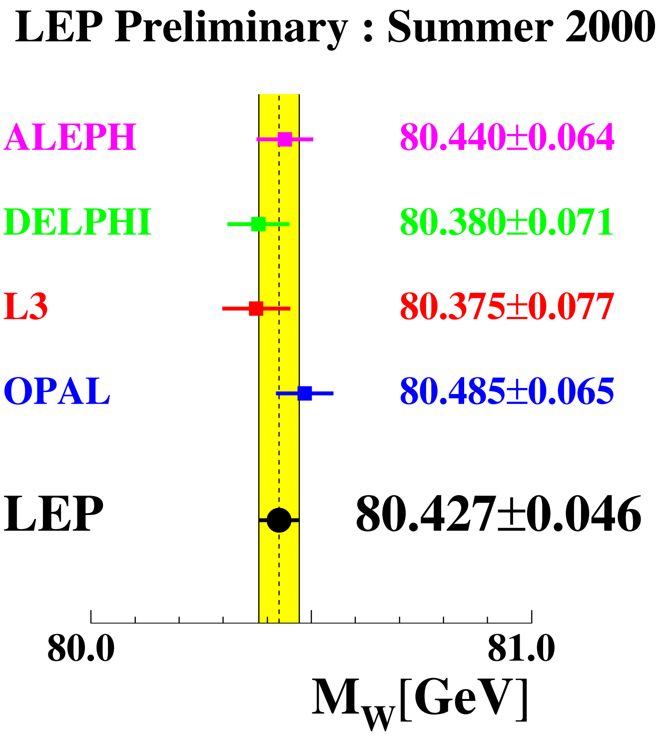

Figure 8.3: The LEP average W mass at the time of the 2000 summer conferences.

distribution is measured together with the transverse momentum of the neutrino, inferred by the large missing momentum of the event. The W mass is determined through the direct reconstruction of the transverse mass distribution of the event. The systematic uncertainties on the measurement are dominated by the calorimeter energy scale and the modelling of the proton decay remnants. The measurements from the two experiments CDF [113, 114] and D0 [115] are combined with that from the UA2 experiment [116] at CERN's SPS to give a hadron collider W mass average of

$$M_{\mathrm{W}} = 80.452 \pm 0.062 \text{ GeV}/c^2 . \tag{8.6}$$

The Tevatron collider and experiments are currently undergoing an upgrade which will allow for higher luminosities and thus a reduction in the uncertainties on this measurement.

8.4 World Average W Mass

The LEP average W mass may be combined with the hadron collider W mass to give a world average W mass of [1]

$$M_{\mathrm{W}} = 80.436 \pm 0.037 \text{ GeV}/c^2 , \tag{8.7}$$

as shown in Figure 8.4. Also shown on this figure is the indirect measurement obtained from the neutrino-nucleon scattering experiments CCFR [117] and NuTeV [118]. These experiments measure the quantity $\sin^2\theta_W = 1 - M_{\mathrm{W}}^2/M_{\mathrm{Z}}^2$ from the ratio of neutral current to charged current neutrino-nucleon cross sections.

8.5 Standard Model Constraints

The indirect determination of the W mass is the result of a global electroweak fit using Equation 1.1. This fit uses as input measurements made at many experiments such as the Z mass from LEP and SLD, the value of $\sin^2\theta_W$ from NuTeV and CCFR neutrino-nucleon scattering and measurements of the top quark mass from CDF [119] and D0 [120] to give a fitted W mass of [1]

$$M_{\mathrm{W}}^{indirect} = 80.386 \pm 0.025 \text{ GeV}/c^2 , \tag{8.8}$$

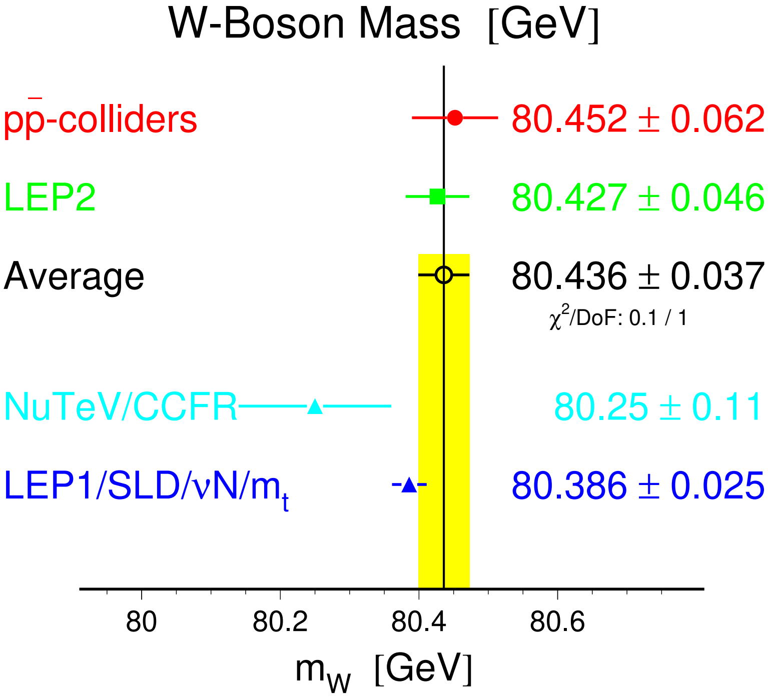

Figure 8.4: The world average W mass at the time of the 2000 summer conferences. The value labelled $p\bar{p}$-collider is the average hadron collider W mass measurement from Equation 8.6 and that labelled LEP2 is the LEP average measurement from Equation 8.4. Also shown are the measurements obtained from neutrino-nucleon scattering experiments NuTeV and CCFR and the indirect measurement (labelled LEP1/SLD/νN/m_t) obtained from a global fit to electroweak data as described in the text.

as shown in Figure 8.4. The direct and indirect measurements are also shown in Figure 8.5, confirming the Standard Model prediction is correct at the one-loop level. Also shown on this figure are the Standard Model predictions of the Higgs mass as a function of the mass of the W boson and the mass of the top quark. It is clear that a light value of the Higgs boson mass is favoured. The direct W boson measurement can be included with all the other Standard Model parameters in a fit for the Higgs boson mass. The difference of the χ^2 of this fit to zero, $\Delta\chi^2$, is shown in Figure 8.6. The minimum value of this χ^2 gives a Higgs mass of [121]

$$M_{\mathrm{H}} = 60^{+52}_{-29}\,\mathrm{GeV}/c^2\,. \tag{8.9}$$

The one-sided 95% upper confidence limit on the Higgs mass is 165 GeV/c^2. These results can be compared with the result of direct searches for the Higgs boson which set a lower limit of 113.3 GeV/c^2 on its mass [122].

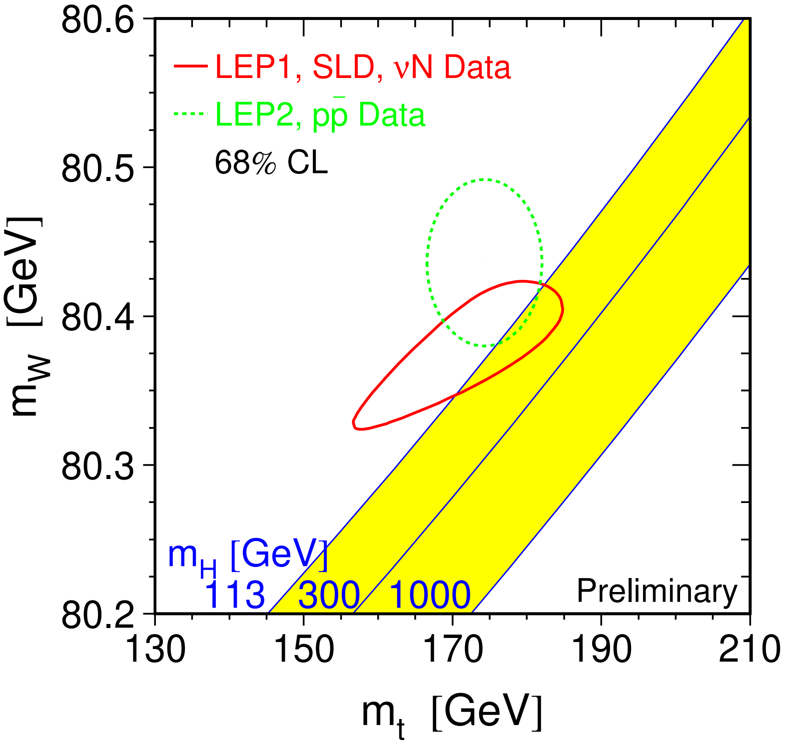

Figure 8.5: Comparison of direct (dashed line) and indirect (solid line) W mass measurements. Also shown are the predictions for a range of Higgs boson masses as a function of the W mass and top quark mass.

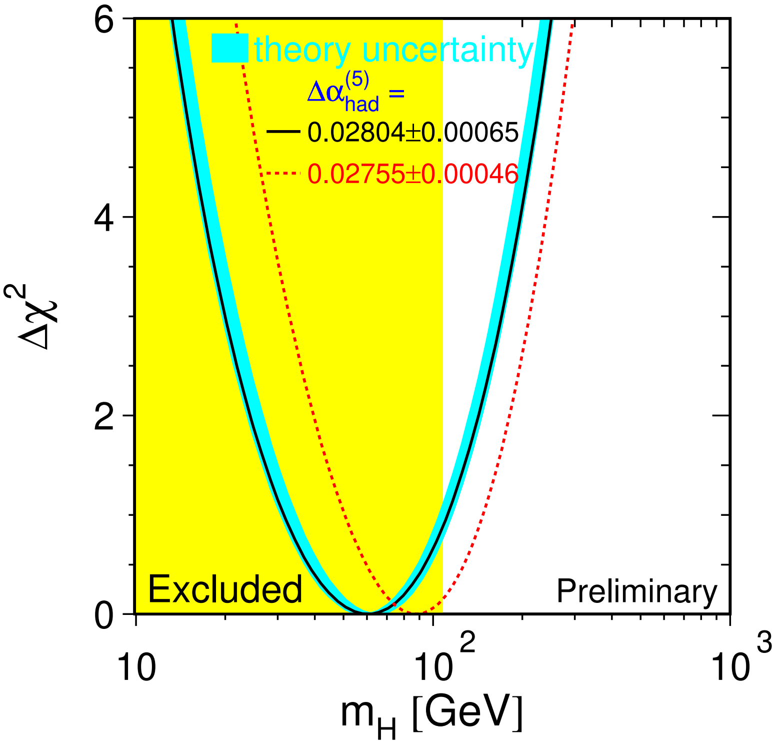

Figure 8.6: The change in χ^2 as a function of the Higgs mass (see text).

Chapter 9

Summary and Conclusions

The direct measurement of the mass of the W boson is of fundamental physical importance, providing an experimental test of the Standard Model of particle physics and providing constraints on the mass of the only particle of the Standard Model yet to be observed, the Higgs boson. This thesis describes a measurement of the mass of the W boson in the fully hadronic decay channel with data collected by the ALEPH detector during 1998 and 1999.

The similarities between W pair signal events and the mainly $q\overline{q}$ background mean that the most efficient way of selecting signal events is with a multi-variable neural network, giving selection efficiencies of around 90% and purities of around 80% for centre of mass energies between 188.6 GeV and 201.6 GeV.

Once the events are selected the W bosons are reconstructed from their decay products. The first step in this process is jet clustering using the `DURHAM PE` algorithm. A kinematic fit is used to improve the dijet invariant mass resolution by applying the constraints of energy and momentum conservation. Allowing for collinear initial state radiation in the kinematic fit is found not to improve the overall mass resolution. The selection and treatment of initial state photons in the detector does bring an improvement and reduces the expected statistical uncertainty on the W mass measurement. The mass resolution is further improved by rescaling by the LEP beam energy. The jets are paired by considering the `CC03` matrix element for each possible combination of dijet pairs, and then using information from the dijet opening angles and a window applied to the dijet invariant masses. The end result of the reconstruction process is a two dimensional mass distribution that is constructed for both data and Monte Carlo simulated data.

The W mass is measured by comparing the two dimensional invariant mass distribution for data with many distributions from a large Monte Carlo sample of events. These distributions are obtained by reweighting according to the ratio of `CC03` matrix elements, and used to build a probability density function. The W mass is taken to be the value which maximises a log-likelihood function built using this probability density function. The value obtained in this way is shown to be unbiased and its statistical uncertainty in agreement with Monte Carlo expectations. The stability of the measured mass is checked for variations in the neural network selection cut, the mass window and the kinematic fit.

The systematic uncertainties are discussed paying particular attention to detector related effects, fragmentation and final state interactions. The W mass from fully hadronic events selected from data taken in 1998 and 1999 is found to be

$$M_{\mathrm{W}} = 80.453 \pm 0.070(\mathrm{stat}) \ \pm 0.035(\mathrm{syst}) \ \pm 0.042(\mathrm{FSI}) \ \pm 0.017(\mathrm{LEP})\ \mathrm{GeV}/c^2\,. \tag{9.1}$$

This measurement is combined with ALEPH, LEP and other W mass measurements to give a prelimnary world average W mass of

$$M_{\mathrm{W}}^{direct} = 80.436 \pm 0.037\ \mathrm{GeV}/c^2\,, \tag{9.2}$$

which is in good agreement with the indirect measurement of the mass obtained from Standard Model fits to electroweak data from various experiments of

$$M_{\mathrm{W}}^{indirect} = 80.386 \pm 0.025\ \mathrm{GeV}/c^2\,. \tag{9.3}$$

The measured W mass when used with measurements of other Standard Model parameters favours a light mass of the Higgs boson.

The data collected during the year 2000 will reduce further the statistical uncertainty on the LEP W mass measurement. The understanding of the systematic uncertainties then becomes crucial, in particular those due the modelling of the fragmentation and the final state interactions. If this understanding is forthcoming then it may be hoped that the precision on the direct measurement of the W mass will be as high as that on the indirect measurement.

Appendix A

Neural Network Variables

The neural network used for selecting fully hadronic WW signal events uses global event shape variables as some of its input variables. These are variables which condense the information about the many different particles in an event into a single variable which is often dimensionless. Two such variables are *thrust* and *sphericity*, which are now described.

A.1 Thrust

The thrust, T, is defined as the sum of the lengths of the longitudinal momenta of the final state particles relative to the axis $\mathbf{n}$ which maximises this sum:

$$T = \frac{\sum_{i=1}^{N} |\mathbf{n}.\mathbf{p}_i|}{\sum_{i=1}^{N} |\mathbf{p}_i|}, \tag{A.1}$$

where N is the number of particles in the final state and $\mathbf{p}_i$ is the momenta of the i particle. T lies between $1/2$ and 1, with $T \sim 1$ for a dijet event and $T \sim 1/2$ for an isotropic event. Thus fully hadronic WW events are expected to generally have lower values of thrust than $\mathrm{q\overline{q}}$ events.

A.2 Sphericity

The sphericity tensor $S^{\alpha\beta}$ is defined as

$$S^{\alpha\beta} = \frac{\sum_{i=1}^{N} p_i^{\alpha} p_i^{\beta}}{\sum_{i=1}^{N} |\mathbf{p}_i|^2}, \tag{A.2}$$

where $\alpha, \beta = 1, 2, 3$ correspond to the x, y, z components of the momentum respectively. The sphericity S is then defined as

$$S = \frac{3}{2}\left(\lambda_2 + \lambda_3\right) \, , \tag{A.3}$$

where $\lambda_{\alpha,\beta}$ are the eigenvalues obtained from diagonalising the sphericity tensor. S lies between 0 and 1 with $S \sim 0$ corresponding to a dijet event and $S \sim 1$ corresponding to an isotropic event. Thus fully hadronic WW events are expected to have generally higher values of sphericity than $\mathrm{q\overline{q}}$ events.

Appendix B

Rescaling

The improvement in the dijet mass resolution obtained by rescaling is most easily illustrated by considering the case of on shell W bosons produced close to the threshold for WW pair production. If the two dijet invariant masses obtained after a 4C kinematic fit are M_{12} and M_{34} then the rescaled masses are defined in terms of the LEP beam energy, E_b as:

$$\begin{aligned} M_{12}^{resc} &= E_b \tfrac{M_{12}}{E_{12}} \\ M_{34}^{resc} &= E_b \tfrac{M_{34}}{E_{34}} \, , \end{aligned} \tag{B.1}$$

where the dijet energies E_{12} and E_{34} are the sum of the individual jet energies:

$$\begin{aligned} E_{12} &= E_1 + E_2 \\ E_{34} &= E_3 + E_4 \, . \end{aligned} \tag{B.2}$$

Firstly assume that there are no experimental errors in the invariant mass reconstruction so that $M_{12} = M_{12}^{true}$, $E_{12} = E_{12}^{true}$ and $\vec{p}_{12} = \vec{p}_{12}^{true}$.

Considering the two-body kinematics of the dijet system then it must be true that

$$E_{12} + E_{34} = 2E_b \, , \tag{B.3}$$

and since $\vec{p}_{12} = -\vec{p}_{34}$, then it follows that $|\vec{p}_{12}|^2 = |\vec{p}_{34}|^2$, thus taking the difference of the square of the invariant masses

$$\begin{aligned} M_{12}^2 - M_{34}^2 &= \left(E_{12}^2 - |\vec{p}_{12}|^2\right) - \left(E_{34}^2 - |\vec{p}_{34}|^2\right) \\ &= E_{12}^2 - E_{34}^2 \\ &= \left(E_{12} + E_{34}\right)\left(E_{12} - E_{34}\right) \, . \end{aligned} \tag{B.4}$$

Substituting for E_{34} from B.3 into B.4,

$$E_{12} = E_b + \frac{M_{12}^2 - M_{34}^2}{4E_b}\,, \tag{B.5}$$

and substituting for E_b from this result into B.1 gives an expression for the rescaled mass:

$$M_{12}^{resc} = \frac{M_{12}}{E_{12}}\left(E_{12} - \frac{M_{12}^2 - M_{34}^2}{4E_b}\right) = M_{12}\left(1 - \frac{M_{12}^2 - M_{34}^2}{4E_bE_{12}}\right)\,, \tag{B.6}$$

showing that the rescaled mass is a function of both dijet masses M_{12} and M_{34}.

Now introduce experimental error by considering the case where a particle with a small amount of energy δ is assigned to jet 1 instead of jet 4:

$$E_1 = E_1^{true} + \delta \qquad E_4 = E_4^{true} - \delta \tag{B.7}$$

$$\vec{p}_1 = \vec{p}_1^{\,true} + \vec{\delta} \qquad \vec{p}_4 = \vec{p}_4^{\,true} - \vec{\delta} \tag{B.8}$$

Assuming again that the energies and momenta of the particles are measured perfectly then we have that

$$\begin{aligned} M_{12}^2 &= E_{12}^2 - \vec{p}_{12}^{\,2} \\ &= \left(E_{12}^{true} + \delta\right)^2 - \left(\vec{p}_{12}^{\,true} + \vec{\delta}\right)^2 \\ &= \left(E_{12}^{true}\right)^2 + \delta^2 - \left|\vec{p}_{12}^{\,true}\right|^2 - \left|\vec{\delta}\right|^2 + 2E_{12}^{true}\delta - 2\vec{p}_{12}^{\,true}.\vec{\delta} \\ &\approx \left(M_{12}^{true}\right)^2 + 2\delta E_{12}^{true}\,, \end{aligned} \tag{B.9}$$

since $\vec{p}_{12}^{\,true} \ll E_{12}^{true}$ close to threshold. The jet energy is

$$\begin{aligned} E_{12}^2 &= \left(E_{12}^{true} + \delta\right)^2 \\ &\approx \left(E_{12}^{true}\right)^2 + 2\delta E_{12}^{true}\,, \end{aligned} \tag{B.10}$$

assuming $\delta^2 \sim 0$. The ratio of dijet mass and energy is then

$$\frac{M_{12}^2}{E_{12}^2} \approx \frac{\left(M_{12}^{true}\right)^2\left(1 + 2\delta\frac{E_{12}}{M_{12}^2}\right)}{\left(E_{12}^{true}\right)^2\left(1 + 2\delta\frac{E_{12}}{E_{12}^2}\right)}\,, \tag{B.11}$$

with the approximation $E_{12} \approx E_{12}^{true}$ to zero order in δ. Rewriting B.11 in terms of a single argument in δ,

$$\left(\frac{M_{12}}{E_{12}}\right)^2 \approx \left(\frac{M_{12}^{true}}{E_{12}^{true}}\right)^2\left(1 + 2\delta E_{12}\frac{E_{12}^2 - M_{12}^2}{E_{12}^2M_{12}^2}\right)\,, \tag{B.12}$$

the ratio is given approximately by

$$\left(\frac{M_{12}}{E_{12}}\right) \approx \left(\frac{M_{12}^{true}}{E_{12}^{true}}\right)\left(1+\frac{\delta}{E_{12}}.\frac{p_{12}^2}{M_{12}^2}\right) . \tag{B.13}$$

This can be written in terms of the boost of the W in the lab frame, $\beta_{\mathrm{W}} = p/E$ and $\gamma = \left(1-\beta_{\mathrm{W}}^2\right)^{-\frac{1}{2}} = E/M$, to give

$$\left(\frac{M_{12}}{E_{12}}\right) \approx \left(\frac{M_{12}^{true}}{E_{12}^{true}}\right)\left(1+\frac{\delta}{E_{12}}.\left(\gamma\beta_{\mathrm{W}}\right)^2\right) . \tag{B.14}$$

Thus the relative error on M_{12}/E_{12} is suppressed by the factor $(\gamma\beta_{\mathrm{W}})^2$ by rescaling.

If B.14 is substituted into B.1 then the rescaled mass becomes:

$$\begin{aligned} M_{12}^{resc} &\approx M_{12}^{true}\left(1-\frac{\left(M_{12}^{true}\right)^2-\left(M_{34}^{true}\right)^2}{4E_b E_{12}^{true}}\right)\left(1+\frac{\delta}{E_{12}}.\left(\gamma\beta_{\mathrm{W}}\right)^2\right) \\ &\approx \left(M_{12}^{resc}\right)^{true}\left(1+\frac{\delta}{E_{12}}.\left(\gamma\beta_{\mathrm{W}}\right)^2\right) . \end{aligned} \tag{B.15}$$

Now consider the effect of the error on the 4C masses before rescaling by rewriting B.9 as

$$M_{12} \approx M_{12}^{true}\left(1+\frac{\delta}{M_{12}}\gamma\right) . \tag{B.16}$$

The reduction in errors when using the rescaled masses is thus

$$\left(\frac{\delta}{M_{12}}\gamma\right) / \left(\frac{\delta}{E_{12}}.\left(\gamma\beta_{\mathrm{W}}\right)^2\right) = \frac{1}{\gamma\beta_{\mathrm{W}}^2} . \tag{B.17}$$

To summarise, the rescaled masses M_{12}^{resc} and M_{34}^{resc} are not in themselves better estimators of M_{12}^{true} and M_{34}^{true}. For the case of on shell W's close to threshold rescaling significantly improves the dijet resolution because the effects of misassignment of particles are reduced. For the case of Breit-Wigner decay of W's at higher energies rescaling adds more information through the use of the W velocities.

Appendix C

Uncertainty due to Finite Monte Carlo Statistics

The systematic uncertainty of the W mass due to the finite number of Monte Carlo events used to build the reference mass distribution can be computed using the fact that each bin in this distribution has a different sensitivity to the W mass.

The contribution to the uncertainty on M_{W} from the invariant mass bin i is

$$\Delta M_{\mathrm{W}}^{i} = \frac{\Delta\sigma_i}{\partial\sigma_i/\partial M_{\mathrm{W}}}\,, \tag{C.1}$$

where σ_i is the differential cross section over the ith bin in the invariant mass m:

$$\sigma_i = \int_i \frac{d\sigma}{dm}dm\,. \tag{C.2}$$

This can be estimated as

$$\sigma_i = \frac{N_i}{\mathcal{L}\mathcal{E}}\,, \tag{C.3}$$

with an error of

$$\Delta\sigma_i = \frac{\sqrt{N_i}}{\mathcal{L}\mathcal{E}}\,, \tag{C.4}$$

where N_i is the number of events in bin i, $\mathcal{L}$ is the integrated luminosity and $\mathcal{E}$ is the selection efficiency.

The probability density function for an event to have an invariant mass m is defined as

$$\rho\left(m\right) = \frac{d\sigma/dm}{\sigma_T}; \qquad \sigma_T = \int \frac{d\sigma}{dm}dm\,, \tag{C.5}$$

$$\tag{C.6}$$

and can be approximated as

$$\rho_i\left(m\right) = \frac{N_i}{N_T}.\frac{1}{\Delta m_i}, \tag{C.7}$$

where N_T is the total number of events and Δm_i is the width of the invariant mass bin i.

Taking the derivative of this with respect to M_{W} and making use of Equation C.3,

$$\frac{\partial \rho_i}{\partial M_{\mathrm{W}}} = \frac{1}{N_T}.\frac{\partial}{\partial M_{\mathrm{W}}}\left(\frac{N_i}{\Delta m_i}\right) = \frac{1}{\sigma_T \Delta m_i}.\frac{\partial \sigma_i}{\partial M_{\mathrm{W}}}, \tag{C.8}$$

where σ_T is the total cross section. Making use of this together with Equation C.4 the contribution to the uncertainty on M_{W} from each invariant mass bin from Equation C.1 can be written as

$$\Delta M_{\mathrm{W}}^i = \frac{\sqrt{N_i}}{\mathcal{L}\mathcal{E}}.\frac{1}{\sigma_T \Delta m_i \frac{\partial \rho_i}{\partial M_{\mathrm{W}}}} = \frac{1}{\Delta m_i.\frac{\partial \rho_i}{\partial M_{\mathrm{W}}}.\frac{N_T}{\sqrt{N_i}}}. \tag{C.9}$$

Thus assuming that the contribution from each bin is independent the final uncertainty on the W mass due to the finite number of Monte Carlo events used is given by

$$\left(\Delta M_{\mathrm{W}}^T\right)^2 = \frac{1}{\sum_i \left(\Delta m_i.\frac{\partial \rho_i}{\partial M_{\mathrm{W}}}.\frac{N_T}{\sqrt{N_i}}\right)^2}. \tag{C.10}$$

Bibliography

[1] A. Gurtu, "Precision Tests of the Electroweak Gauge Theory." Talk at ICHEP 2000, XXXth International Conference on High Energy Physics, July 27 – August 2, 2000, Osaka, Japan.

[2] Z. Kunszt and W. J. Stirling, "Determination of the mass of the w boson,". In Physics at LEP2, G. Altarelli, T. Sjöstrand and F. Zwirner (editors), CERN 96-01 (1996) vol. 1, 141.

[3] S. L. Glashow, "Partial symmetries of weak interactions," *Nucl. Phys.* **22** (1961) 579–588.

[4] S. Weinberg, "A model of leptons," *Phys. Rev. Lett.* **19** (1967) 1264–1266.

[5] A. Salam, "Weak and electromagnetic interactions,". Originally printed in Svartholm: Elementary Particle Theory, Proceedings Of The Nobel Symposium Held 1968 At Lerum, Sweden, Stockholm 1968, 367-377.

[6] S. L. Glashow, J. Iliopoulos, and L. Maiani, "Weak interactions with lepton - hadron symmetry," *Phys. Rev.* **D2** (1970) 1285.

[7] P. W. Higgs, "Broken symmetries and the masses of gauge bosons," *Phys. Rev. Lett.* **13** (1964) 508.

[8] I. J. R. Aitchison and A. J. Hey, *Gauge Theories in Particle Physics*. Adam Hilger, 2 ed., 1989.

[9] D. Griffiths, *Introduction to Elementary Particles*. Wiley, New York, USA, 1987.

[10] F. Halzen and A. D. Martin, *Quarks and Leptons: an Introductory Course in Modern Particle Physics*. Wiley, New York, USA, 1984.

[11] W. Beenakker and A. Denner, “Standard model predictions for W pair production in electron - positron collisions,” *Int. J. Mod. Phys.* **A9** (1994) 4837–4920.

[12] A. Denner, “Techniques for calculation of electroweak radiative corrections at the one loop level and results for W physics at LEP200,” *Fortschr. Phys.* **41** (1993) 307–420.

[13] D. E. Groom *et al.*, “Review of particle physics,” *Eur. Phys. J.* **C15** (2000) 1.

[14] D. Y. Bardin, A. Leike, T. Riemann, and M. Sachwitz, “Energy dependent width effects in e^+e^- annihilation near the Z pole,” *Phys. Lett.* **B206** (1988) 539–542.

[15] W. Beenakker and F. A. Berends, “WW cross-sections and distributions,”. In Physics at LEP2, G. Altarelli, T. Sjöstrand and F. Zwirner (editors), CERN 96-01 (1996) vol. 1, 79.

[16] V. S. Fadin, V. A. Khoze, A. D. Martin, and A. Chapovsky, “Coulomb effects in W+ W- production,” *Phys. Rev.* **D52** (1995) 1377–1385, `hep-ph/9501214`.

[17] V. A. Khoze and W. J. Stirling, “On the Coulomb effects on the W line shape of LEP-2,” *Phys. Lett.* **B356** (1995) 373–380, `hep-ph/9506203`.

[18] E. A. Kuraev and V. S. Fadin, “On radiative corrections to e+ e- single photon annihilation at high-energy,” *Sov. J. Nucl. Phys.* **41** (1985) 466–472.

[19] D. Bardin, A. Olshevsky, M. Bilenkii, and T. Riemann, “Off-shell W pair production in e+ e- annihilation: Initial state radiation,” *Phys. Lett.* **B308** (1993) 403–410.

[20] D. Bardin and T. Riemann, “Off shell W pair production in e+ e- annihilation: The CC11 process,”. DESY 95-167.

[21] B. Andersson, G. Gustafson, G. Ingelman, and T. Sjöstrand, "Parton Fragmentation and String Dynamics," *Phys. Rept.* **97** (1983) 31.

[22] T. Sjöstrand, "High-energy physics event generation with PYTHIA 5.7 and JETSET 7.4," *Comput. Phys. Commun.* **82** (1994) 74–90.

[23] G. Marchesini *et al.*, "HERWIG version 5.9: A Monte Carlo event generator," `hep-ph/9607393`.

[24] G. Marchesini *et al.*, "HERWIG: A Monte Carlo event generator for simulating hadron emission reactions with interfering gluons. Version 5.1 - April 1991," *Comput. Phys. Commun.* **67** (1992) 465–508.

[25] T. Sjöstrand and V. A. Khoze, "On Color rearrangement in hadronic W+ W- events," *Z. Phys.* **C62** (1994) 281–310, `hep-ph/9310242`.

[26] T. Sjöstrand and V. A. Khoze, "Does the W mass reconstruction survive QCD effects?," *Phys. Rev. Lett.* **72** (1994) 28–31, `hep-ph/9310276`.

[27] L. Lönnblad, "ARIADNE version 4: A Program for simulation of QCD cascades implementing the color dipole model," *Comput. Phys. Commun.* **71** (1992) 15.

[28] L. Lönnblad, "Reconnecting colored dipoles," *Z. Phys.* **C70** (1996) 107–114.

[29] G. Gustafson, "Dual description of a confined color field," *Phys. Lett.* **B175** (1986) 453.

[30] G. Gustafson and U. Pettersson, "Dipole formulation of QCD cascades," *Nucl. Phys.* **B306** (1988) 746.

[31] G. Goldhaber, S. Goldhaber, W. Lee, and A. Pais, "Influence of Bose-Einstein statistics on the antiproton proton annihilation process," *Phys. Rev.* **120** (1960) 300–312.

[32] L. Lönnblad and T. Sjöstrand, "Bose-Einstein effects and W mass determinations," *Phys. Lett.* **B351** (1995) 293–301.

[33] L. Lönnblad and T. Sjöstrand, "Modelling Bose-Einstein correlations at LEP 2," *Eur. Phys. J.* **C2** (1998) 165, `hep-ph/9711460`.

[34] **ALEPH** Collaboration, D. Decamp *et al.*, "ALEPH: A Detector for electron-positron annihilations at LEP," *Nucl. Instrum. Meth.* **A294** (1990) 121–178.

[35] **DELPHI** Collaboration, P. Aarnio *et al.*, "The DELPHI detector at LEP," *Nucl. Instrum. Meth.* **A303** (1991) 233–276.

[36] **L3** Collaboration, "The Construction of the L3 Experiment," *Nucl. Instrum. Meth.* **A289** (1990) 35.

[37] **OPAL** Collaboration, K. Ahmet *et al.*, "The OPAL detector at LEP," *Nucl. Instrum. Meth.* **A305** (1991) 275–319.

[38] S. Myers and E. Picasso, "The Design, Construction and Commissioning of the CERN Large Electron Positron Collider," *Contemp. Phys.* **31** (1990) 387.

[39] "`http://sl.web.cern.ch/SL/opnews/Lep/lep98.html`."

[40] "`http://sl.web.cern.ch/SL/opnews/Lep/lep99.html`."

[41] R. Assmann *et al.*, "Calibration of Centre-of-Mass Energies at LEP1 for Precise Measurements of Z Properties," *Eur. Phys. J.* **C6** (1999) 187.

[42] L. Arnaudon *et al.*, "Accurate Determination of the LEP Beam Energy by Resonant Depolarization," *Z. Phys.* **C66** (1995) 45–62.

[43] A. A. Sokolov and I. Ternov, "On Polarization and Spin Effects in the Theory of Synchrotron Radiation," *Sov. Phys. Dokl.* **8** (1964) 1203.

[44] The LEP Energy Working Group, "Evaluation of the LEP Centre-of-Mass Energy for Data Taken in 1998,". LEP Energy Working Group 99/01.

[45] The LEP Energy Working Group, "Evaluation of the LEP Centre-of-Mass Energy for Data Taken in 1999,". LEP Energy Working Group 00/01.

[46] **ALEPH** Collaboration, "The ALEPH Handbook 1995 Vol. 1," European Organization for Nuclear Research, CERN, Geneva, 1995.

[47] **ALEPH** Collaboration, "The ALEPH Handbook 1995 Vol. 2," European Organization for Nuclear Research, CERN, Geneva, 1995.

[48] **ALEPH** Collaboration, D. Buskulic *et al.*, "Performance of the ALEPH detector at LEP," *Nucl. Instrum. Meth.* **A360** (1995) 481–506.

[49] D. Creanza *et al.*, "The new ALEPH Silicon Vertex Detector," *Nucl. Instrum. Meth.* **A409** (1998) 157.

[50] G. J. Barber *et al.*, "Performance of the Three-Dimensional Readout of the ALEPH Inner Tracking Chamber," *Nucl. Instrum. Meth.* **A279** (1989) 212.

[51] W. B. Atwood *et al.*, "Performance of the ALEPH Time Projection Chamber," *Nucl. Instrum. Meth.* **A306** (1991) 446–458.

[52] J. Knobloch, "JULIA Users and Programmers Guide," Tech. Rep. ALEPH 90-11, ALEPH internal report, 1990.

[53] E. B. H. Albrecht and J. Boucrot, "ALEPH Physics Analysis Package - ALPHA User's guide - versions > 124," Tech. Rep. ALEPH 99-087, ALEPH internal report, 1999.

[54] B. Bloch-Devaux *et al.*, "KINGAL Users Guide," Tech. Rep. ALEPH 87-53, ALEPH internal report, 1987.

[55] F. Ranjard, "GALEPH - Monte Carlo Program for ALEPH," Tech. Rep. ALEPH 88-119, ALEPH internal report, 1988.

[56] R. Brun, F. Bruyant, M. Maire, A. C. McPherson, and P. Zanarini, "GEANT3,". CERN-DD/EE/84-1.

[57] M. Skrzypek, S. Jadach, W. Placzek, and Z. Wąs, "Monte Carlo Program KORALW-1.02 for W Pair Production at LEP-2 / NLC energies with Yennie-Frautschi-Suura Exponentiation," *Comput. Phys. Commun.* **94** (1996) 216.

[58] T. Ishikawa, Y. Kurihara, M. Skrzypek, and Z. Was, “Four-quark final state in w-pair production: Case of signal and background,” *Eur. Phys. J.* **C4** (1998) 75, `hep-ph/9702249`.

[59] **MINAMI-TATEYA Group** Collaboration, T. Ishikawa *et al.*, “GRACE manual: Automatic Generation of Tree Amplitudes in Standard Models: Version 1.0,”. KEK-92-19.

[60] E. Barberio and Z. Wąs, “PHOTOS: A Universal Monte Carlo for QED Radiative Corrections. Version 2.0,” *Comput. Phys. Commun.* **79** (1994) 291–308.

[61] S. Jadach, B. F. L. Ward, and Z. Wąs, “The Monte Carlo program KORALZ, version 4.0, for the lepton or quark pair production at LEP / SLC energies,” *Comput. Phys. Commun.* **79** (1994) 503–522.

[62] I. Riu, *Measurement of the W mass from the* $\mathrm{WW} \rightarrow \mathrm{q\overline{q}q\overline{q}}$ *channel with the ALEPH detector*. PhD thesis, Universitat Autonoma de Barcelona, 1998.

[63] M. Chalmers, *Measurements of the mass of the W boson in the* $\mathrm{WW} \rightarrow \mathrm{q\overline{q}q\overline{q}}$ *channel with the ALEPH detector*. PhD thesis, University of Glasgow, 1999.

[64] **ALEPH** Collaboration, R. Barate *et al.*, “Measurement of W pair production in e+ e- collisions at 189-GeV,” *Phys. Lett.* **B484** (2000) 205, `hep-ex/0005043`.

[65] D. Bardin *et al.*, “GENTLE/4fan v. 2.0: A program for the semi-analytic calculation of predictions for the process e+ e- –> 4f,” *Comput. Phys. Commun.* **104** (1997) 161, `hep-ph/9612409`.

[66] W. Beenakker, F. A. Berends, and A. P. Chapovsky, “Radiative corrections to pair production of unstable particles: Results for e+ e- –> 4fermions,” *Nucl. Phys.* **B548** (1999) 3, `hep-ph/9811481`.

[67] S. Jadach, W. Placzek, M. Skrzypek, B. F. L. Ward, and Z. Wąs, “Exact O(alpha) gauge invariant YFS exponentiated Monte Carlo for (un)stable W+ W- production at and beyond LEP2 energies,” *Phys. Lett.* **B417** (1998) 326, `hep-ph/9705429`.

[68] A. Denner, S. Dittmaier, M. Roth, and D. Wackeroth, "O(alpha) corrections to e+ e- –> W W –> 4fermions(+gamma): First numerical results from RACOONWW," *Phys. Lett.* **B475** (2000) 127, `hep-ph/9912261`.

[69] **JADE** Collaboration, W. Bartel *et al.*, "Experimental Studies on Multi-Jet Production in e+e- Annihilation at PETRA energies," *Z. Phys.* **C33** (1986) 23.

[70] S. Catani, Y. L. Dokshitzer, M. Olsson, G. Turnock, and B. R. Webber, "New clustering algorithm for multi - jet cross-sections in e+ e- annihilation," *Phys. Lett.* **B269** (1991) 432–438.

[71] S. Bethke, Z. Kunszt, D. E. Soper, and W. J. Stirling, "New jet cluster algorithms: Next-to-leading order QCD and hadronization corrections," *Nucl. Phys.* **B370** (1992) 310–334.

[72] T. Sjöstrand, "The LUND Monte Carlo for e+e- Jet Physics," *Comput. Phys. Commun.* **28** (1983) 229.

[73] J. M. Scarr and I. ten Have, "PTCLUS: Jet Finding Algorithm for High Energy Hadronic Final States,". ALEPH 89-150, PHYSIC 89-60.

[74] **ALEPH** Collaboration, R. Barate *et al.*, "Measurement of the W mass and width in e+ e- collisions at 189-GeV," *Eur. Phys. J.* **C17** (2000) 241–261.

[75] "ABCFIT Manual." `http://alephwww.cern.ch/ hansenjo/ALEPH-ONLY/abcfit/abcfit.html`.

[76] "KINFIT Manual." `http://alephwww.cern.ch/ valassi/kinfit/`.

[77] F. James and M. Roos, "'MINUIT' a System for Function Minimization and Analysis of the Parameter Errors and Correlations," *Comput. Phys. Commun.* **10** (1975) 343.

[78] J. B. Hansen, *Triple Gauge-boson Couplings in W pair Production via e+e- Annihilation*. PhD thesis, Copenhagen University / Niels Bohr Institute, 1996.

[79] K. Kölbig, “D503: Minimum of a Function of One Variable.” `http://wwwinfo.cern.ch/asdoc/shortwrupsdir/d503/top.html`.

[80] **ALEPH** Collaboration, R. Barate *et al.*, “Measurement of the W mass in e+ e- collisions at 183-GeV,” *Phys. Lett.* **B453** (1999) 121.

[81] F. Teubert. Talk at ALEPH WW meeting.

[82] S. Goodsir, *A W Mass measurement with the ALEPH detector*. PhD thesis, Imperial College, 1999.

[83] **ALEPH** Collaboration, R. Barate *et al.*, “Measurement of the W mass by direct reconstruction in e+ e- collisions at 172-GeV,” *Phys. Lett.* **B422** (1998) 384.

[84] S. Schmidt-Kärst, “W Mass Measurement using Fully Hadronic Events at LEP2.” Talk at ICHEP 2000, XXXth International Conference on High Energy Physics, July 27 – August 2, 2000, Osaka, Japan.

[85] Lluisa Mir, Private Communication.

[86] I. Riu, “W Mass Background Systematic Study using Z peak data,”. ALEPH 97-060, PHYSIC 97-053.

[87] Lluisa Mir, Private Communication.

[88] “Aleph detector systematics information.” `http://alephwww.cern.ch/LEP2ANALYSIS/WTF/Conveners/ligabue/jets.html`.

[89] Gerald Rudolph, Talks in ALEPH WW meeting and LEP W Workshop, CERN 19th April 2000.

[90] Lluisa Mir, Private Communication.

[91] Eric Lançon, Talks in ALEPH WW meetings.

[92] **ALEPH** Collaboration, D. Decamp *et al.*, “A Study of Bose-Einstein correlations in e+ e- annihilation at 91-GeV,” *Z. Phys.* **C54** (1992) 75–86.

[93] **ALEPH** Collaboration, R. Barate *et al.*, "Bose-Einstein correlations in W-pair decays," *Phys. Lett.* **B478** (2000) 50–64.

[94] Hugo Ruiz, `http://alephwww.cern.ch/ ruizh/FSI.html`.

[95] **ALEPH** Collaboration, "Measurement of the W Mass and Width in e+ e- collisions at *sqrts*= 192-202 GeV,". ALEPH 2000-018, CONF 2000-015, Contributed paper for ICHEP 2000.

[96] **ALEPH** Collaboration, R. Barate *et al.*, "Measurement of the W mass in e+ e- collisions at production threshold," *Phys. Lett.* **B401** (1997) 347–362.

[97] **DELPHI** Collaboration, P. Abreu *et al.*, "Measurement and interpretation of the W pair cross-section in e+ e- interactions at 161-GeV," *Phys. Lett.* **B397** (1997) 158–170.

[98] **DELPHI** Collaboration, P. Abreu *et al.*, "Measurement of the W pair cross-section and of the W mass in e+ e- interactions at 172-GeV," *Eur. Phys. J.* **C2** (1998) 581.

[99] **DELPHI** Collaboration, P. Abreu *et al.*, "Measurement of the mass of the W boson using direct reconstruction at s**(1/2) = 183-GeV," *Phys. Lett.* **B462** (1999) 410–424.

[100] **DELPHI** Collaboration, "Measurement of the mass and width of the W Boson in e^+ e^- collisions at $\sqrt{s} = 189$ GeV,". DELPHI 2000-144 CONF 443, Contributed paper for ICHEP 2000.

[101] **DELPHI** Collaboration, "Measurement of the mass and width of the W Boson in e^+ e^- collisions at $\sqrt{s} = 192$–202 GeV,". DELPHI 2000-149 CONF 446, Contributed paper for ICHEP 2000.

[102] **L3** Collaboration, M. Acciarri *et al.*, "Pair-production of W bosons in e+ e- interactions at s**(1/2) = 161-GeV," *Phys. Lett.* **B398** (1997) 223–238.

[103] **L3** Collaboration, M. Acciarri *et al.*, "Measurements of mass, width and gauge couplings of the W boson at LEP," *Phys. Lett.* **B413** (1997) 176.

[104] **L3** Collaboration, M. Acciarri *et al.*, "Measurement of mass and width of the W boson at LEP," *Phys. Lett.* **B454** (1999) 386, `hep-ex/9909010`.

[105] **L3** Collaboration, "Preliminary Results on the Measurement of the Mass and Width of the W Boson at LEP,". L3 Note 2377, March 1999.

[106] **L3** Collaboration, "Preliminary Results on the Measurement of the Mass and Width of the W Boson at LEP,". L3 Note 2575, July 2000.

[107] **OPAL** Collaboration, K. Ackerstaff *et al.*, "Measurement of the mass of the W boson in e+ e- collisions at s**(1/2) = 161-GeV," *Phys. Lett.* **B389** (1996) 416–428.

[108] **OPAL** Collaboration, K. Ackerstaff *et al.*, "Measurement of the W boson mass and W+ W- production and decay properties in e+ e- collisions at s**(1/2) = 172- GeV," *Eur. Phys. J.* **C1** (1998) 395, `hep-ex/9709006`.

[109] **OPAL** Collaboration, G. Abbiendi *et al.*, "Measurement of the W mass and width in e+ e- collisions at 183-GeV," *Phys. Lett.* **B453** (1999) 138, `hep-ex/9901025`.

[110] **OPAL** Collaboration, G. Abbiendi *et al.*, "Measurement of the mass and width of the W boson in e+ e- collisions at 189-GeV," `hep-ex/0009018`.

[111] **OPAL** Collaboration, "Measurement of the Mass of the W Boson in e^{+} e^{-} annihilations at 192-202 GeV,". OPAL Physics Note PN422 (updated July 2000).

[112] The LEP Collaborations ALEPH, DELPHI, L3, OPAL and the LEP W Working Group, "Combined Preliminary Results on the Mass and Width of the W Boson Measured by the LEP Experiments,". LEPEWWG/MASS/2000-01, ALEPH 2000-086 PHYSIC 2000-032, DELPHI 2000-165 PHYS 879, L3 Note 2617, OPAL TN-667.

[113] **CDF** Collaboration, T. Affolder *et al.*, "Measurement of the W boson mass with the collider detector at Fermilab," `hep-ex/0007044`.

[114] **CDF** Collaboration, F. Abe *et al.*, "Measurement of the W boson mass," *Phys. Rev.* **D52** (1995) 4784–4827.

[115] **D0** Collaboration, B. Abbott *et al.*, "A new measurement of the W boson mass at D0," `hep-ex/9907028`.

[116] **UA2** Collaboration, J. Alitti *et al.*, "An Improved determination of the ratio of W and Z masses at the CERN anti-p p collider," *Phys. Lett.* **B276** (1992) 354–364.

[117] **CCFR** Collaboration, K. S. McFarland *et al.*, "A precision measurement of electroweak parameters in neutrino nucleon scattering," *Eur. Phys. J.* **C1** (1998) 509, `hep-ex/9701010`.

[118] **NuTeV** Collaboration, K. S. McFarland *et al.*, "Measurement of sin**2(Theta(W)) from neutrino nucleon scattering at NuTeV," `hep-ex/9806013`.

[119] **CDF** Collaboration, F. Abe *et al.*, "Measurement of the top quark mass with the Collider Detector at Fermilab," *Phys. Rev. Lett.* **82** (1999) 271–276, `hep-ex/9810029`.

[120] **D0** Collaboration, B. Abbott *et al.*, "Direct measurement of the top quark mass at D0," *Phys. Rev.* **D58** (1998) 052001, `hep-ex/9801025`.

[121] B. Pietrzyk, "The Global Fit to Electroweak Data." Talk at ICHEP 2000, XXXth International Conference on High Energy Physics, July 27 – August 2, 2000, Osaka, Japan.

[122] ALEPH, DELPHI, L3 and OPAL Collaborations, The LEP working group for Higgs boson searches, "Searches for Higgs bosons: Preliminary combined results using LEP data collected at energies up to 209 GeV." Submitted to ICHEP 2000, XXXth International Conference on High Energy Physics, July 27 – August 2, 2000, Osaka, Japan.